UCL Université catholique de Louvain

École polytechnique de Louvain (EPL)

epl

Nanostructured bioactive surfaces to control cell behaviour

Dissertation presented by
Annelies BAUWENS

for obtaining the Master's degree in
Chemical and Materials Engineering

Supervisor(s)
Sophie DEMOUSTIER , Karine GLINEL

Reader(s)
Claire CHATTAWAY, Alain JONAS

Academic year 2015-2016

Acknowledgement

First, I would like to thank my supervisors, Prof. Karine Glinel and Prof. Sophie Demoustier who were available when needed for guidance all along this project. I would also like to thank them for all the advice they gave me during the meetings we had all over the year.

Secondly, I would like to thank very much the PhD student Claire Chattaway for her support, her availability and the hours she spent to help and guide me.

Finally, I would like to thank Colette Douchamps, Cécile D'Haese and Varvara Gribova for the SEM, AFM and spin-coating trainings respectively. I also thank Catherine Philippart for all the advice and guidance she gave in the laboratory as well as for her accessibility for any question at any time.

Lastly I thank all the people from the BSMA laboratory for their kindness.

Abstract

With the emergence of nanotechnologies, smart surfaces and biointerfaces are being developed increasingly fast. These could potentially allow a better control over cell processes with an improved manipulation of cell fate. Moreover, smart surfaces are promising for the development of innovative drug delivery systems.

Several researches have already proven that nanopillars can provide a direct access to the cell, with the delivery of DNA and other compounds of interest inside the cell medium. On the other hand, it has been proven that a controlled release of drugs can be achieved by using redox-responsive surfaces. A particularly interesting type of redox-responsiveness is based on the reversible formation of a disulfide bond. Indeed, disulfide bondings are characterised by an excellent stability in extracellular medium whereas they are rapidly degraded if exposed to the intracellular medium. This is because it is a reductive environment maintained by the glutathione/glutathione disulfide couple.

The project of which this thesis is a part, intends to investigate the combination of nanopillars with a redox-responsive coating for drug delivery applications. Therefore gold nanopillars need to be functionalised by grafting a thiol containing copolymer. But only a fraction of the thiol functions are grafted to the gold surface, the remaining part is used to attach thiolated compounds. When the nanopillars penetrate inside the cell, the copolymer is submitted to its reductive environment triggering the release of the attached thiolated compounds inside the cell.

In this study, we developed and optimised a strategy to selectively functionalise the top of the gold nanopillars by copolymer grafting. This could open the way to the fabrication of chemically and topographically patterned surfaces. Our strategy is based on the deposition of a sacrificial, protecting layer onto the gold nanostructured surfaces. This layer is subsequently partially etched in order to only expose the top of the gold nanopillars. Thereafter the copolymer is grafted on the exposed gold surface (tops of the nanopillars only) and the remaining sacrificial layer is dissolved. Characterisation results of the obtained selectively functionalised gold surfaces proved the efficiency of our strategy. Copolymer grafting was effectively observed and only low gold surface coverage was established.

Furthermore, we also investigated complete functionalisation (i.e. funtionalisation of the whole available gold surface) of nanostructured gold surfaces by copolymer grafting. Results indicate that grafting on nanostructured surfaces is less efficient than on flat controls. The reason behind this is not clearly understood. Nevertheless the surface topography and the geometry of the nanopillar seem to play an important role.

Finally, we evaluated the redox-responsiveness of a completely functionalised nanostructured gold surface by copolymer grafting. We compared the obtained results with flat controls. Results show that the redox-responsive property is still present although less pronounced than on flat controls.

CONTENTS

Acknowlegdement **i**

Abstract **iii**

List of abbreviations **vii**

1 Introduction **1**
1.1 General Context 1
1.2 Master thesis context 3

2 Literature review **5**
2.1 Nanotopography and cell behaviour 5
2.1.1 Morphology 6
2.1.2 Adhesion 6
2.1.3 Proliferation 7
2.1.4 Differentiation 7
2.1.5 Drug delivery applications 7
2.2 Elaboration of nanopillars by template-based methods 8
2.2.1 Template fabrication 8
2.2.2 Deposition techniques 10
2.3 Sacrificial layers 11
2.3.1 Deposition techniques 11
2.3.2 Etching techniques 13
2.3.3 Water-soluble polymers 14
2.4 Gold surface modification and thiol chemistry 15
2.4.1 Self-assembled monolayers (SAM) 15
2.4.2 Polythiols 16

3 Objectives and strategy **21**
3.1 Towards the design of redox-responsive nanostructured gold surfaces[1] . . 21
3.2 Functionalisation of the nanopillars 23
3.3 Objectives of this master thesis 25

4 Materials and methods **27**
4.1 Solvents and products 27
4.2 Elaboration of gold nanopillars 28
4.2.1 Elaboration of flat gold surfaces 28

4.2.2 Fabrication of track-etched membrane[1] . . . 28
4.2.3 Gold electrodeposition . . . 29
4.2.4 Template removal . . . 29
4.3 Spin-coating . . . 29
4.3.1 Preparation of PAA solution . . . 30
4.3.2 PAA spin-coating . . . 30
4.4 Plasma treatment . . . 31
4.5 Gold surface modification . . . 31
4.5.1 Copolymer grafting . . . 31
4.5.2 PAA film dissolution . . . 33
4.5.3 SAM grafting . . . 33
4.5.4 Grafting and release of PEG-SH from the copolymer layer . . . 33
4.6 Characterisation techniques . . . 35
4.6.1 Electrochemical techniques . . . 35
4.6.2 X-Ray Photoelectron Spectroscopy (XPS) . . . 42
4.6.3 Ellipsometry . . . 43
4.6.4 Scanning electron microscopy (SEM) . . . 44
4.6.5 Atomic force microscopy (AFM) . . . 44

5 Results and discussion **45**
5.1 Gold nanopillars fabrication and exposure of their tops for selective functionalisation . . . 46
5.1.1 Gold nanopillar fabrication . . . 46
5.1.2 PAA spin-coating . . . 46
5.1.3 Plasma treatment . . . 53
5.2 Bare gold surfaces . . . 59
5.3 Gold surface modification . . . 62
5.3.1 Copolymer grafting . . . 62
5.3.2 SAM grafting . . . 68
5.3.3 Copolymer redox-responsiveness assessment . . . 71

6 Conclusion and future perspectives **75**

Bibliography **77**

Appendices **83**

A Literature review **85**
A.1 Spin-coating on gold nanopillars . . . 85
A.2 Gold nanopillar properties . . . 87

B Results **89**
B.1 Spin-coating calibration . . . 89
B.2 Spin-coating at a speed higher than 1750 rpm on nanostructured gold surfaces . . . 89
B.3 PAA film defects created by plasma treatment . . . 90
B.4 Thiol grafting on electrodeposited and evaporated flat gold surfaces . . . 91
B.5 Dodecanethiol grafting on a nanostructured gold surface . . . 91
B.6 Optimisation of PAA film dissolution . . . 92

LIST OF ABBREVIATIONS

AAO Anodic Aluminium Oxide.

AFM Atomic Force Microscopy.

BF Blocking Factor.

BSMA Bio- and Soft Matter.

CAT Chloramine T.

CV Cyclic Voltammetry.

CVD Chemical vapor deposition.

DMA Dimethylacrylamide.

DNA Deoxyribonucleic Acid.

DTT Dithiothreitol.

EIS Electrochemical Impedance Spectroscopy.

ETA Ethanolamine.

GSH Glutathione tripeptide.

h-MSCs human mesenchymal stem cells.

HEPES 2-[4-(2-hydroxyethyl)piperazin-1-yl]ethanesulfonic acid.

IMCN Institute of Condensed Matter and Nanosciences.

$\mathbf{M}_w$ Mass average molar mass.

MES 2-(N-morpholino)ethanesulfonic acid.

NADPH Nicotinamide Adenine Dinucleotide Phosphate.

NMP Nitroxide-Mediated Polymerisation.

PAA Poly(acrylic acid).

PC Polycarbonate.

PEG-SH Sulfhydryl Poly(ethylene glycol).

PMMA Poly(methylmethacrylate).

QDs Quantum Dots.

$\mathbf{R}_s$ Solution Resistance.

$\mathbf{R}_{ct}$ Resistance to charge transfer.

RAFT Reversible Addition-Fragmentation chain Transfer.

SAM Self-assembled monolayer.

SEM Scanning Electron Microscopy.

TlaAm N-thiolactone Acrylamide.

XPS X-ray Photoelectron Spectroscopy.

CHAPTER 1

INTRODUCTION

1.1 General Context

Control of cell processes and manipulation of cell fate on biomaterials is of great interest in novel research domains like tissue engineering, regenerative medicine, drug screening and general cell study at the molecular level.

Tissue engineering and regenerative medicine are novel innovative research fields facing the ever-increasing burden of trauma, congenital abnormalities and degenerative diseases. They promise new biological therapeutics based on the acceleration and stimulation of inherent healing potential of cells and tissues. Alternatively they also seek to create replacement biological tissues and organs to replace damaged, deteriorated or lost body parts.[2] Nevertheless one of the main challenges is to perfectly control cell differentiation so as to elaborate complex tissue. Indeed, cell differentiation can be induced through various stimuli affecting cell behaviour. It has been proven that the surface characteristics on which cells adhere and are cultured strongly influence their behaviour including among others differentiation, adhesion, proliferation and morphology.[3] Therefore the properties of biointerfaces are studied in detail to control cell behaviour, notably their differentiation.

Topographical and chemical cues have been extensively investigated to control cell behaviour. Surfaces are notably chemically modified by bio(macro)molecules to create interactions with cells and to stimulate them. Those chemical compounds can be divided into three categories according to their function : functional molecules (e.g. deoxyribonucleic acid (DNA), drug), specific recognition molecules (e.g. antibody, RGD peptides) and responsive molecules (e.g. polymers whose bio-adhesiveness depends on external parameters like pH or temperature).[3]

Over the last decades it has been proven that topographical cues can influence cell processes.[3–8] In fact in the early 1960s Curtis[9] studied the effect of microtopography on cell migration. The substrate was made of grooves and ridges and he found that cell migration was more extensive on the ridges than in the grooves. These early experiments revealed that substrate topography can influence cell behaviour.

Since then cell stimulation via biointerfaces has significantly evolved thanks to the development of nanotechnologies that offer the possibility to fabricate nanopatterned surfaces to investigate the influence of surface nanostructure on cell processes. The in-

teractions at this scale could potentially influence cell mechanisms. As surface feature size is several orders of magnitude below that of cells, the response is however more complex. But investigating the influence of the features at the nanoscale is particularly interesting because they have a size similar to individual cell receptors. Thus receptors could be specifically targeted to control cell response.

Nanotechnologies comprise numerous tools to fabricate nanostructured surfaces with a feature size ranging between a few nanometers to several μm. Among the possibilities of nanostructures one can find nanowires, nanorods, nanotubes, nanopillars, nanofibers. All these nanostructures could potentially affect cells. Indeed, nanostructures like nanowires for example exert mechanical constraints at the nanoscale on adhered cells affecting among others their morphology.[4] Moreover, the mechanical constraints will depend on the size and the density distribution of the nanostructure, which are adjustable parameters. The surface topography can thus be tuned to obtain the desired constraints and influence on cell behaviour.[4] Nanowires can also affect and ease the mechanism of endocytosis within a specific range of size and density. This gives a direct access to the cytoplasm of the cell.[6] This configuration can be very interesting to study the local delivery of drugs on cellular behaviour.

Many cell processes are dynamic. First, cells adhere to a surface through specific receptors called integrins. Integrins are transmembrane proteins acting as an interface between the extra- and intracellular environment. On the extracellular side, they can interact with the extracellular matrix and for example recognise RGD sequences (Arginine, Glycine, Asparagine). Whereas on the intracellular side, they interact with various molecules stimulating the formation of focal adhesions[a].[10]

Following adhesion cells can grow, differentiate and migrate. The way the cell will behave highly depends on environmental factors like chemical stimuli and physical features of the surface (topography). Cells search for the most suitable environment to develop. As cell culture is a dynamic process, cell environment changes inducing alteration of cell behaviour. In vivo cells are thus constantly subjected to changes in their environment. By adapting themselves towards these changes, cells are able to differentiate.[1] Therefore surfaces with changing properties can be particularly useful to stimulate cell processes.

As already mentioned, surfaces can be chemically modified and one of the possibilities is to use stimuli-responsive macromolecules. These compounds also called smart polymers undergo a huge change of their properties (e.g. conformation) under the application of an external stimulus like a variation of pH, ionic strength or temperature. For example redox-responsive polymers show variation of their properties via a redox environment (i.e. oxidising or reducing conditions). Stimuli-responsive macromolecules can be used to show or hide or deliver a chemical compound affecting cell behaviour. Therefore they are of high interest in drug-delivery applications.

Smart surfaces that combine nanotopography and stimuli-responsive behaviour are of a great interest to influence cell processes.

[a]Focal adhesions are large macromolecular assemblies through which mechanical force and regulatory signals are transmitted between the extracellular matrix (ECM) and an interacting cell

1.2 Master thesis context

This master thesis is part of a main research project, which is the elaboration of nanostructured and stimuli-responsive surfaces for drug delivery applications. The release of the drug is based on the application of specific stimuli, which allows to regulate the drug release for optimal therapeutic efficiency. The objective of the research is to study the effect of therapeutic agents and nanotopography on cell processes especially differentiation and proliferation. A better understanding of these cell processes could allow a better control of them. As said previously controlling cell differentiation and proliferation is crucial in tissue engineering.

The fabrication of gold nanopillars is developed in IMCN/BSMA since several years using a template-based technique employing a track-etched polycarbonate (PC) film as template that is filled with gold by electrodeposition.
The gold nanopillars are functionalised by grafting a redox-responsive copolymer, which controls the drug delivery to cells through a stimulus. The chosen stimulus is redox-responsive via a disulfide link that can be reversibly formed and cleaved under redox stimulation. This choice is motivated by the fact that disulfide bonds are cleaved in cell medium because it is a reductive environment. Moreover redox-sensitive disulfide bonds are very stable in extracellular medium.
The chosen redox-responsive copolymer is a thiol containing copolymer, because the multiple thiols allow that a part of them are grafted to the gold surface whereas the remaining thiols can be further modified by grafting a thiolated compound, through a disulfide link. Nevertheless thiols are very sensitive to oxidation and therefore need to be protected. A strategy for thiol protection was developed by Ghent researchers.[11,12] The thiol functions are trapped in thiolactone rings and released by aminolysis. The copolymer that will be employed is thus a polythiolactone, which is a polythiol precursor. The grafting on gold surfaces and release of the thiol functions occurs at the same time in a one-pot reaction.

The subject of this master thesis is to develop and optimise a strategy to functionalise completely and selectively (i.e. only the top of) the gold nanopillars (figure 1.1). In case of selective functionalisation, the gold surface that is not intended to be functionalised needs to be protected by a sacrificial layer before copolymer grafting. The strategy to deposit, etch and remove this sacrificial layer was developed and optimised. Moreover flat gold surfaces and completely and selectively functionalised nanostructured surfaces were compared regarding surface coverage by the copolymer and grafting and releasing of thiolated compounds.

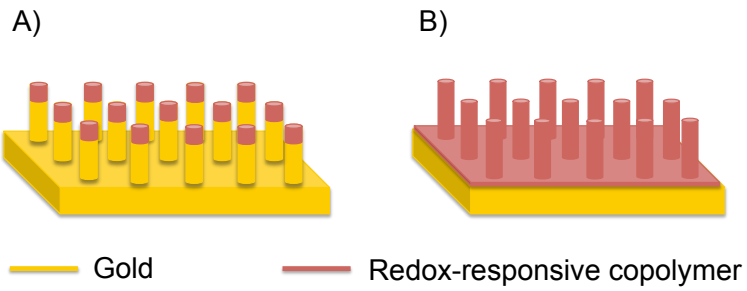

Figure 1.1 – A) Selective functionalisation of the tops of the nanopillars. B) Complete functionalisation of the nanostructured surface.

To begin a literature review on topics relevant to the subject of this master thesis is provided. Next, the materials and methods used during this work are detailed. This chapter also includes all characterisation techniques and their operating parameters. Then, the main obtained results are presented and discussed. Finally, this work is ended with a conclusion and some future perspectives.

CHAPTER 2

LITERATURE REVIEW

In this chapter, a literature review is provided on different subjects relevant to the strategy developed in this master thesis : the elaboration of partially functionalised gold nanopillars to control cell behaviour. First of all, the behaviour of cells on nanotopographical surfaces, especially nanopillars, is described. Next, an overview is given on the elaboration of nanopillars by template-based methods. Then, sacrificial layers with their corresponding deposition and etching techniques are discussed. Finally, gold surface functionalisation and cell behaviour are described.

2.1 Nanotopography and cell behaviour

Cells are naturally surrounded by a complex environment made of extracellular matrix (ECM) and neighbouring cells. This environment interacts with cells. Indeed, cells are sensitive to various kinds of environmental stimuli. These can act at a macro- or nanoscale and can be chemical (e.g. molecules) or physical (e.g. mechanical/electrical stimuli). This large amount of stimuli multiplies the possibilities regarding the design of biointerfaces. Currently focus is mainly given on two aspects : chemical and topographical stimuli.[3] In this section, the topographical aspect is investigated.
It all began in 1964 when a study suggested that cells react to the topography of their environment.[13] Since then, micro- and nanofabrication techniques have significantly evolved allowing developing nanostructured surfaces. Along with these developments, it has been demonstrated many times that cells can react to nanotopography.[8,14,15] This reaction depends upon many factors including cell type, feature size and geometry.[16] Three basic nanotopographic geometries are nanogratings, nanopillars and nanopits (figure 2.1). All of these structures affect cell behaviour in their own way.
In this section attention is given to nanopillars. Some confusion may exist between the term nanopillar and nanowire both used in the literature because of their similarity. To avoid any confusion in this work, nanopillars and nanowires are considered as solid and cylindrical nanostructures attached to a surface as shown in figure 2.1 B. The subtle difference between them is that nanowires have typically a higher aspect ratio although this is not consistently respected.[7]
The effect of nanopillars and nanowires on cell behaviour is described with respect to cell morphology, adhesion, proliferation and differentiation. Eventually the use of nanopillars in drug delivery applications is discussed.

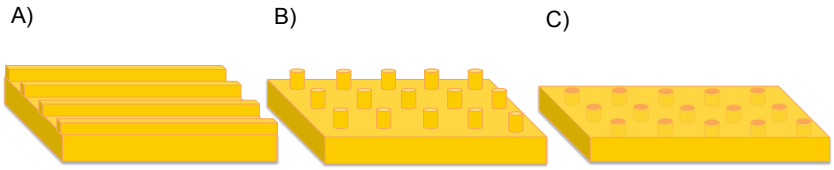

Figure 2.1 – Nanotopographic geometries. A) Nanogratings. B) Nanopillars. C) Nanopits.

2.1.1 Morphology

The first effect of nanotopography relates to cell morphology. In fact cells can adapt their morphology to the surrounding environment resulting in cell alignment along the nanostructures and modifications in cell area. Nevertheless this behaviour is not observed across all cell types.[16]
Regarding nanopillars, studies generally show that cells are rounder with a smaller projected cell area compared to flat surfaces[4,7] although exceptions exist.[17] Moreover increasing the height of the nanopillars or their density leads to a further decrease in cell area.[18,19] These observations can be noted a few minutes or hours after interfacing,[a] which is relatively early.[7] Explanations for the reduced cell area on nanopillars can be the high surface energy of the nanopillar material and the small surface area available for cell attachment.[8] Indeed, if nanopillars are high and/or densely arranged cells cannot reach the underlying surface and stay on top of the nanopillars (figure 2.2 B) with a small available contact surface. Whereas for less dense nanopillars the cells adapt their morphology, losing the round shape, and can even reach the underlying surface (figure 2.2 A) to maximise the contact with the surface.

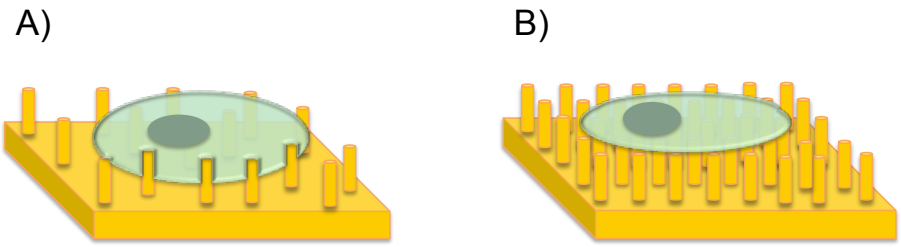

Figure 2.2 – General morphology of a cell adhered on nanopillars with a low (A) and high (B) density.

2.1.2 Adhesion

Cell adhesion is controlled by large protein scaffolds known as focal adhesion points. In some cases, nanotopographic structures can enhance mammalian cell adhesion because they are designed to mimic extracellular matrix proteins interacting with focal adhesion points.[20]
In case of nanopillars, their height and density are determining factors regarding cell adhesion. High-density of nanopillars ($\geq 30 \,.\, 10^6$ nanopillars/cm^2) generally inhibits cell adhesion[21] whereas medium (> 1 and $< 30 \,.\, 10^6$ nanopillars/cm^2) and low-density ($\leq 10^6$ nanopillars/cm^2) almost consistently support and even promote adhesion.[19] Attention has to be paid to the fact that these borderlines between nanopillar densities vary

[a] When the cells are removed from their continous culture and seeded onto nanopillars

following different geometries and materials used to fabricate the nanopillars.[7] However, a key difference between high- and low-density of nanopillars is the available surface area for cell attachment. For high densities, cells have to adhere to the top of nanopillars whereas with low densities they can reach the underlying flat surface. Consequently, the available surface for high densities is lower than for low densities resulting in reduced cell adhesion.[7] It has also been observed that cells on nanopillars exhibit only punctuated adhesion complexes.[15]
In the end the pillar height plays an important role. In fact, low nanopillars promote adhesion in contrary to higher nanopillars.[22] Indeed, if the nanopillars have a small height, the cell is more likely to reach the underlying surface and have access to a larger available surface for adhesion.

2.1.3 Proliferation

Regarding proliferation, trends are ambiguous for nanopillars as studies show wide discrepancies. Indeed, some nanopillar sizes and substrate materials promote proliferation whereas others reduce the proliferation rate.[16] Therefore, no general tendencies can currently be distinguished when it comes to cell proliferation on nanopillars.[7]

2.1.4 Differentiation

Studies have shown that nanopillars can influence stem cell fate. For example Liu and co-workers showed that mesenchymal stem cells preferentially differentiate into osteoblasts and chondrocytes when cultured on silicon nanowire substrates in the absence of growth factors.[23] They demonstrated that nanowires provide mechanical and topographical cues governing mesenchymal stem cell differentiation. However feature size has a great influence and studies have shown that only short nanowires induced and promoted osteogenic differentiation.[8]

Several studies also showed that nanopillars could affect cell elongation, a maturational feature of many types of neurons.[4] Migliorini and co-workers analysed the effect of nanopillars on the differentiation process of embryonic stem cells (ES)-derived neuronal precursors into neurons. They demonstrated that neuronal differentiation was enhanced when neuronal precursors were plated on nanopillars in comparison with flat polydimethylsiloxane (PDMS) substrates. Moreover they found that cell culture over nanopillars accelerated the differentiation of a fraction (40%) of the neuronal precursors with the maximal enhancement ($\pm$ threefold) after 6 h of culture.[24]

2.1.5 Drug delivery applications

Drug delivery applications can be related to the influence nanopillars have on cell behaviour especially morphology. Two nanostructures have been investigated to deliver drug to cells: nanoneedles and nanosyringes.

With the first ones nanopillars can penetrate into the cells and may have cytosolic access allowing delivery of bioactive compounds attached to the nanopillars. For example, Kim and co-workers demonstrated physical penetration of silicon nanowires in mammalian cells during cell incubation.[25] DNA-funtionalised nanowires were successfully used to deliver DNA coding green fluorescent protein into cells as the expression of this protein was observed one day later.

Alternately, nanosyringes consist in hollow nanopillars filled with a bioactive compound which can diffuse through the cell membrane. Park and co-workers used vertically

aligned carbon nanosyringes loaded through capillary action to efficiently deliver plasmid DNA to the cytoplasm of cancer cells and human mesenchymal stem cells (h-MSCs).[26] Other designs are based on nanostraws connected to a microfluidic channel to provide a permanent fluidic pipeline inside the cell.[6]

2.2 Elaboration of nanopillars by template-based methods

Nanopillars can be fabricated by various techniques. Among these, the template-based method is commonly used and will be described in this section. The main steps of this process are illustrated in figure 2.3. The first one is to elaborate a porous template. Secondly, pores are filled with the desired material by using deposition techniques. Finally, the membrane is dissolved or etched.[27] In this section, template fabrication and deposition techniques are discussed whereas etching is described in the next section.

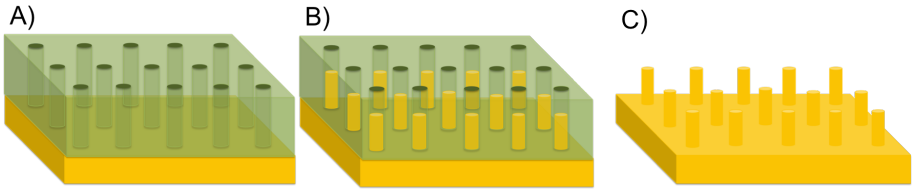

Figure 2.3 – Template-based method to elaborate nanowires. Porous template (A), pore filling (B) and selective dissolution or etching of the template.

2.2.1 Template fabrication

The first step to elaborate nanowires by a template-based method is to make the template. The fabrication of the porous template and its porperties (e.g. density and diameter of the pores) influences certain parameters of the finally obtained nanowires like for example the density, shape and maximum obtainable size; the height of the nanowires cannot exceed the thickness of the template i.e. the height of the pores. The used method should therefore be well-defined to obtain the desired porous template.[28]

Track-etched polymer membranes

Track-etched polymer membranes are made in a two-step process beginning by the irradiation of a polymer layer or film (typically PC or polyester[27]) with energetic heavy ions. The most often used are Ar^{9+} at 220 MeV. These will damage locally the polymer by generating linear tracks. The second step consists of a chemical etching in order to enlarge the tracks to pores. In case of a PC template, chemical etching can be performed in successive temperature regulated baths of hydrogen peroxide, caustic soda and acetic acid aqueous solutions.[28] The two-step process is showed in figure 2.4.

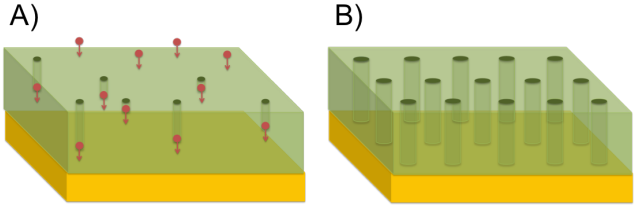

Figure 2.4 – Track-etched template fabrication. A) Ion irradiation B) Pores resulting from chemical etching of the tracks.

The resulting pore diameter ranges from 10 nm to 2000 nm[27] whereas the pore density varies between 10^5 and 10^{10} cm^{-2}, corresponding to a mean pore distance from several tens of μm to 10 nm.[28] The density of the pores is mainly influenced by the first step of the process i.e. the ion irradiation, more precisely the irradiation time. The longer the irradiation the higher the pore density. On the other hand the pore diameter is essentially influenced by the second step i.e. the chemical etching. The composition of the etching solution as well as the etching time and temperature will mainly determine the pore diameter. In particular etching time is varied so as to control pore diameter. Nevertheless as ion irradiation is a random process it can result in pore fusion during chemical etching, affecting the pore size and shape. This randomness is the main disadvantage of track-etching. A scanning electron microscopy (SEM) image of a track-etched template is shown in figure 2.5.

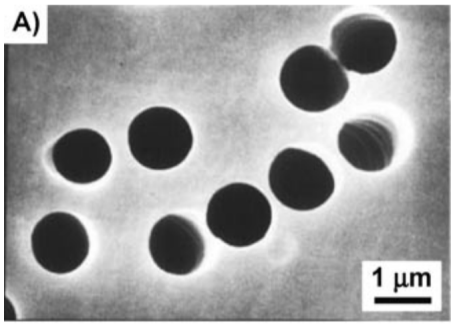

Figure 2.5 – SEM image of a PC membrane with ca. 1 μm pore diameter.[27]

Anodic aluminium oxide (AAO) templates

AAOs are a second type of templates that are also widely used. The fabrication of these templates consists in a two-step anodisation process established by Masuda and co-workers.[29] First, a thin sheet of high purity aluminium is annealed and then an electropolishing solution removes the top layer of aluminium oxide. This is followed by the first anodisation step in an acidic electrolyte solution. Subsequently, the sheet is subjected to a chromate solution removing the oxide layer. After that a second anodisation takes place in the acidic solution again. Finally, the aluminium is removed.[27] The obtained pores are of uniform diameter ranging from 5 to 267 nm[27] and are arranged in a hexagonal array (figure 2.6). Pore densities as high as 10^{11} cm^{-2} can be obtained. The advantage compared to track-etched templates is the absence of intersecting pores.

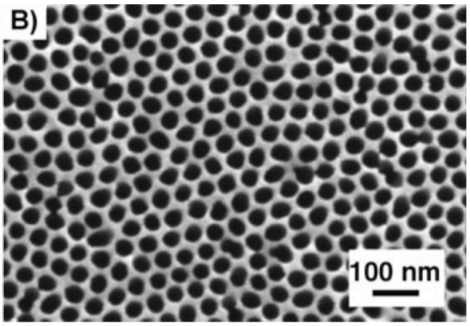

Figure 2.6 – SEM image of an AAO membrane with ca. 35 nm pore diameter.[27]

2.2.2 Deposition techniques

Once the template is made, it can be filled with the nanowire material by using deposition techniques. The most common is electrodeposition but other techniques are also employed.

Electrodeposition

Electrodeposition, also called electroplating, is a technique to deposit a metallic layer onto a surface. The surface to be plated acts as a negative working electrode (cathode) and is immersed in an electrolytic solution containing dissolved metal salts. This solution must allow the flow of electric current. The electric circuit is completed by a positive electrode (anode) that is generally made out of the metal to be deposited and is located at a short distance from the working electrode.[30] If the anode is not intended to dissolve into metal salts, an inert electrode called counter electrode can be used. In that case the metal to be deposited needs to be added to the electrolytic solution in the form of metal salt. Furthermore a reference electrode is added to complete the electrochemical cell. Once the electrochemical cell is completed with two or three electrodes, a voltage or current can be applied to reduce the metal salts so that the metal atoms plate out onto the working electrode. In this way the working electrode is covered by a metallic layer.[31]

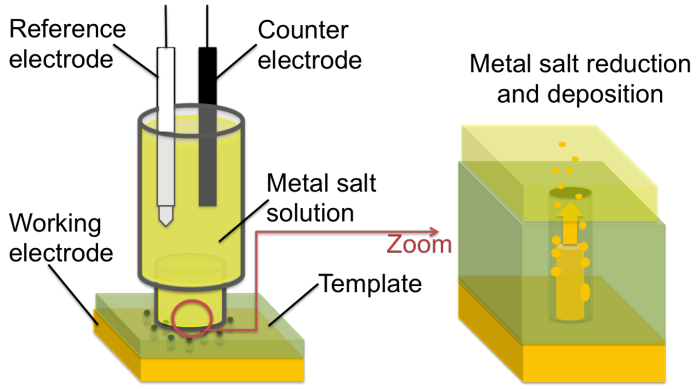

Figure 2.7 – Illustration of an electrochemical deposition with a zoom on a growing nanowire inside a pore using the template's support as working electrode.

In order to fill the template pores by electrodeposition a working electrode is indeed required, which can either be the template's support itself or a thin metal film coated onto one face of the template.[28] During the electrodeposition, nanowires will grow onto the surface of the working electrode inside the pores (figure 2.7). The final height of the nanowires depends on the amount of metal deposited.[32]

The electrodeposition process can be combined with track-etched membranes, as well as, with AAO templates. The main advantage of using this deposition technique is that it does not require high temperatures or low pressure. Moreover the instrumentation is not expensive. The possible drawback of the technique is the necessity to use a conductive and easy to reduce, i.e. more noble, material for the nanowires.[31]

Alternative deposition techniques

Some alternative deposition techniques can also be used like chemical polymerisation or electroless deposition. Chemical polymerisation allows making polymer nanowires

by placing the template into a solution of monomer and polymerisation reagent, i.e. initiator. For example, polyacrylonitrile tubules were made through an alumina template immersed in a solution of acrylonitrile and initiator.[32] Electroless deposition is similar to electrodeposition; a metal salt is reduced and thus plated from a solution onto a surface. The main difference is that in electrodeposition an external power supply is provided (e.g. current) to reduce the metal salt whereas in electroless deposition a reducing agent is used. Consequently the advantage of electroless deposition is that the surface to be plated does not need to be conductive.[32]

2.3 Sacrificial layers

The concept of sacrificial layers appeared in 1965 as well as the corresponding releasing or etching techniques.[33] It is defined as a layer of material deposited for physical separation.[33] The term sacrificial is due to the fact that the deposited layer will eventually be removed by a releasing technique. Micro- and nanofabrication processes frequently use sacrificial layers.

2.3.1 Deposition techniques

Different techniques can be used to deposit a sacrificial layer depending on the sacrificial material and the desired thickness of the deposited layer. One of the most common techniques is spin-coating because it is a simple, cheap and fast process that only requires dissolving the sacrificial material. This technique is described in detail in the following section; other techniques are also briefly mentioned.

Spin-coating

Spin-coating is a widely used technique to deposit thin polymer layers on a substrate as it is a relatively easy technique to use. Indeed, the equipment, called spin-coater, is a simple spinning table with variable speed and acceleration. The spin-coated material needs to be dissolved into a solution and must have a good adhesion with the substrate. If the adhesion is not satisfying, one can either change the material or modify the substrate surface. This can be done by a pretreatment changing for example a hydrophobic surface to a hydrophilic one (or vice-versa) and this according to the nature of the coating solution.[34] Another alternative is the use of binding agents.

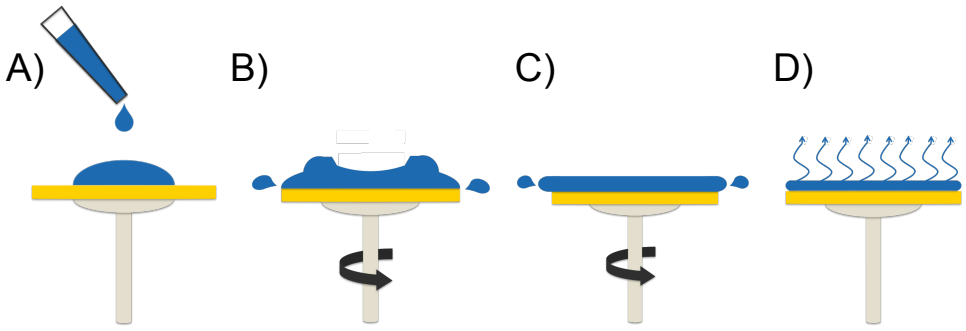

Figure 2.8 – Illustration of the spin-coating process. A) Deposition of the polymer solution on the substrate. B) Acceleration with material ejection. C) Rotation at constant speed with film homogenisation. D) Solvent evaporation.

Before spin-coating, the substrate needs to be fixed and maintained on the table by vacuum sucking.[35] Then, the spin-coating process itself can be divided in four steps

illustrated in figure 2.8. To begin the polymer is deposited on the center of the substrate with a pipette (figure 2.8 A). Next, the spin-coater starts spinning with the chosen acceleration to the desired speed. During this step, material starts to be ejected from the borders of the substrate whereas the central part flattens (figure 2.8 B). This continues until the film is thinned and homogenised (figure 2.8 C). Eventually, the solvent evaporates by baking and a solid, cured film is left (figure 2.8 D).[36]

Controlling the resulting thickness and the film homogeneity is often crucial. Regarding the film thickness, several parameters play a major role. The first one is the speed : the higher the speed, the thinner the film. Moreover the relation between final thickness, h, and the rotation speed, ω, is $h \propto \omega^{\frac{3}{2}}$ according to Scriven L. E..[36] The resulting speed-thickness curve shape is shown in figure 2.9.

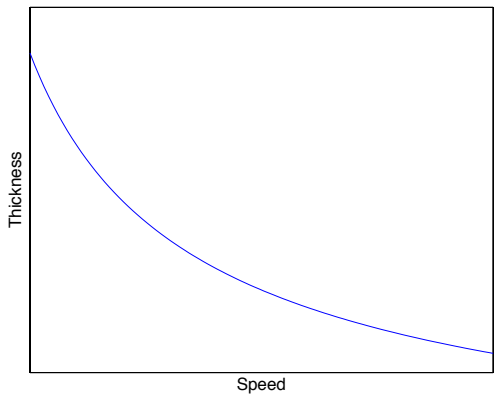

Figure 2.9 – Illustration of the thickness versus speed curve obtained by spin-coating.

Another parameter affecting the thickness is the volume of the solution placed onto the substrate; the higher the volume, the thicker the film. Besides those two, other parameters like acceleration, spin-coating time, concentration and viscosity of the spin-coating solution also affect the final thickness.[34,36] However it is generally admitted that the concentration of the spin-coating solution is the main parameter affecting the thickness. Theoretically predicting the obtained thickness with a specific solution is often too complex. One usually prefers to make calibration curves experimentally by measuring the thickness as a function of just one parameter at the same time. The most common adapted parameters are speed and solution concentration.

To finish, although spin-coating is a technique designed to deposit thin films on flat surfaces, it can also be used on nanostructured surfaces like gold nanopillars. Literature reporting spin-coating on gold nanostructures is briefly reviewed in appendix A section A.1.

Alternative deposition techniques

Although spin-coating is a very attractive technique it is usually limited to polymers and photoresists.[37] In order to deposit alternative materials, other techniques need to be used (e.g. chemical vapor deposition and physical vapor deposition).
Chemical vapor deposition (CVD) is based on a chemical reaction initiated in a vacuum chamber. More precisely, precursors are vaporised to gas and introduced in the vacuum chamber. Those precursors will then react and/or decompose on the substrate surface

resulting in the formation of a film.[35] This technique is appropriate for oxides and nitrides[37] but has a lot of variations resulting in a wide range of different CVD (e.g. low-pressure CVD (LPCVD) and plasma-enhanced CVD (PECVD)).
Physical vapor deposition (PVD) includes several techniques that all rely on the same principle : a physical process produces vapor of a material, which is deposited on the substrate. The difference with CVD is that no chemical reaction is involved. These techniques can be used to deposit metals and alloys. Finally, the type of PVD depends on the way the material is vaporised (e.g. arc vapor deposition or ion plating).[38]

2.3.2 Etching techniques

Following the development of deposition techniques for sacrificial layers, the corresponding etching techniques appeared. Their purpose is to eliminate partially or completely the sacrificial layer without damaging the remaining structure. The distinction can be made between dry etching and wet etching techniques.

Dry etching

Dry etching is generally an anisotropic material removal process using plasmas or etching gases.[33] It was first developed in 1968 by Irving who demonstrated oxygen plasma ashing of a polymer-based photoresist.[39,40] The principle relies on plasma production in a low-pressure gas by dissipation of electrical power to the medium. The major part of the power is transferred to electrons. Once they gain enough energy, collisions with atoms and molecules will start excitation, ionisation and dissociation processes. In this way atoms, radicals and ion species can be produced that can also form the basis of further reactions. Therefore plasma is usually a very complex mixture of chemical species.[41] These plasma species will eventually interact with the sample surface and can cause etching of the sample material by two mechanisms. The first one, physical sputtering, is due to simple ion bombardment. The second one, chemical etching is due to surface reactions leading to gasification of the molecules composing the sample surface.[42] Indeed, depending on the chemical affinity plasma species can be adsorbed. A reaction between adsorbed species and the sample surface is then possible. If the resulting product is volatile it can desorb into the plasma phase and thus etch the sample surface material (figure 2.10). If it is not volatile, it will form a thin film at the sample surface.[41]

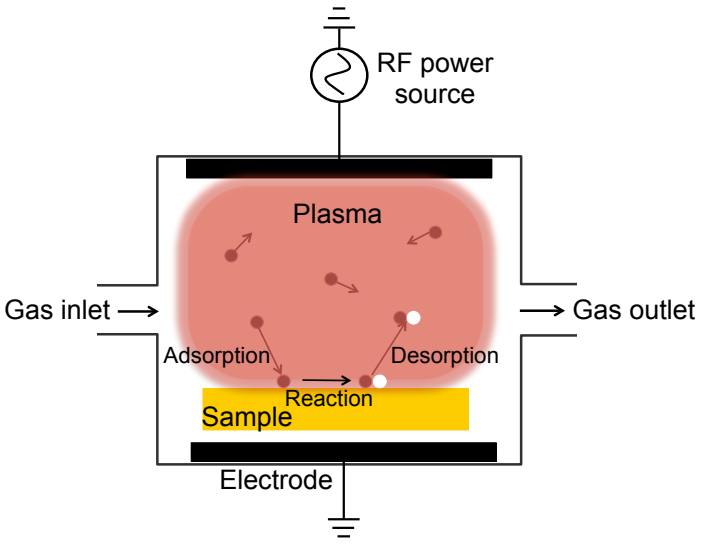

Figure 2.10 – Illustration of plasma etching.

Dry etching techniques based on plasma mainly vary by the excitation technique used to form the plasma (e.g. radio-frequency excitation of a power source at 13.56 MHz) and the chosen gas mixture (e.g. O_2, CF_4). The most important operating conditions to control are the composition and flux of the plasma species. However the operator can tune the following parameters : the power fed to the discharge; the nature, pressure and flow rate of the feed gas.[41]

Polymer films are one of the many material types that can undergo dry etching by plasma treatments[b]. Currently gasification of polymers is possible by atomic oxygen, fluorine, ozone and electronically excited oxygen molecules. Consequently, common gases utilised for polymer etching are CF_4 and O_2. In case the plasma contains oxygen, the polymer surface will likely react and form specific oxygen containing chemical groups :

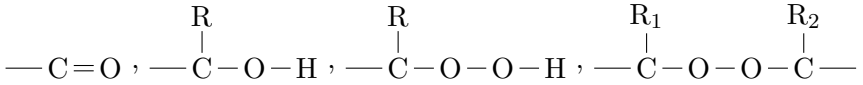

Eventually further interaction of the polymer with the oxygen containing plasma can result in further oxidation with formation of CO_2 and H_2O, which then transit to the gas phase. This process can be considered as chemical etching of polymer oxygen containing plasma.[42] Polymers have different etching rates depending especially on their composition and structure (e.g. cross-linking, branching, crystallinity). The least resistive ones are polymers containing heteroatoms and more particularly oxygen containing groups.[42] Etching rates are typically determined experimentally rather then theoretically as they depend on too many parameters.
Dry etching has the advantage that it does not require dangerous solvents. Furthermore it allows a good process control. Equipment is however expensive and gases can be toxic or corrosive.[33]

Wet etching

An alternative to dry etching avoiding its disadvantages is wet etching. This material removal process uses chemicals in their liquid state or etchants to consume material. First, the material to be removed is immersed in the liquid etchant. Then, a reaction takes place between the liquid etchant and the material it is applied to, resulting in the dissolution of the last one. Finally, the byproducts diffuse and need to be removed by rinsing or cleaning. Wet etching is an isotropic technique and is commonly used to dissolve sacrificial layers.[33]

2.3.3 Water-soluble polymers

Among the long list of possible sacrificial layer materials, some have a particularly attractive property : water solubility. Indeed, water-soluble polymers have two interesting assets. First of all, as they can be dissolved in water, they can be spin-coated easily with a solvent (water) removal at low temperature (95-150°C). As explained before spin-coating is a very attractive technique because it is an easy, fast and cheap deposition technique. Secondly, the sacrificial layer can simply be dissolved in water for removal (wet etching), avoiding the use of organic solvents or corrosive reagents. Water-soluble polymers are thus perfect sacrificial materials combining easy deposition and removal without the use of heavy treatments or dangerous solvents. Poly(acrylic acid) (PAA), dextran and poly(methacrylic acid) (PMA) are examples of water-soluble materials used as sacrificial layers.[43]

[b]When organic materials are removed by plasma treatment the word ashing is used rather than etching

2.4 Gold surface modification and thiol chemistry

Gold is an interesting material due to its chemical stability, surface chemistry and biocompatibility. It is also suitable for a convenient range of processing technologies allowing for example the fabrication of nanostructured surfaces (nanopillars). Furthermore gold surfaces can easily be modified by thiol-based self-assembled monolayers (SAM),[44] which can also be readily functionalised with a chosen functional group. More recently redox-responsive copolymer layers have been grafted on gold surfaces through polythiols chemistry. As the possibilities to modify gold surfaces are numerous and relatively stable through thiol-gold links, these modified surfaces are used in many applications particularly in biological systems including drug delivery, biosensing, etc.[44,45]

2.4.1 Self-assembled monolayers (SAM)

Gold surfaces are commonly modified by SAMs. SAMs are organic assemblies formed by the adsorption of molecular constituents onto the surface of solids. The adsorbates self-organise spontaneously into crystalline (or semicrystalline) structures. The mechanisms allowing this layered assembly involve intra and intermolecular interactions especially by means of the alkyl chains. These result in closer molecular packing and higher order.[46] The ligands molecules that form SAMs have a chemical functionality or headgroup with a specific affinity for the substrate. For gold substrates, the most studied headgroups are thiols, especially alkanethiols (figure 2.11) like dodecanethiol but disulfides can also be used. The adsorption of thiols and disulfides to gold surfaces follows[47] :

$$2\ \mathrm{R-SH} + 2\ \mathrm{Au}_{(s)} \longrightarrow 2\ \mathrm{RS-Au}_{(s)} + \mathrm{H_2}$$
$$\mathrm{RS-SR} + 2\ \mathrm{Au}_{(s)} \longrightarrow 2\ \mathrm{RS-Au}_{(s)}$$

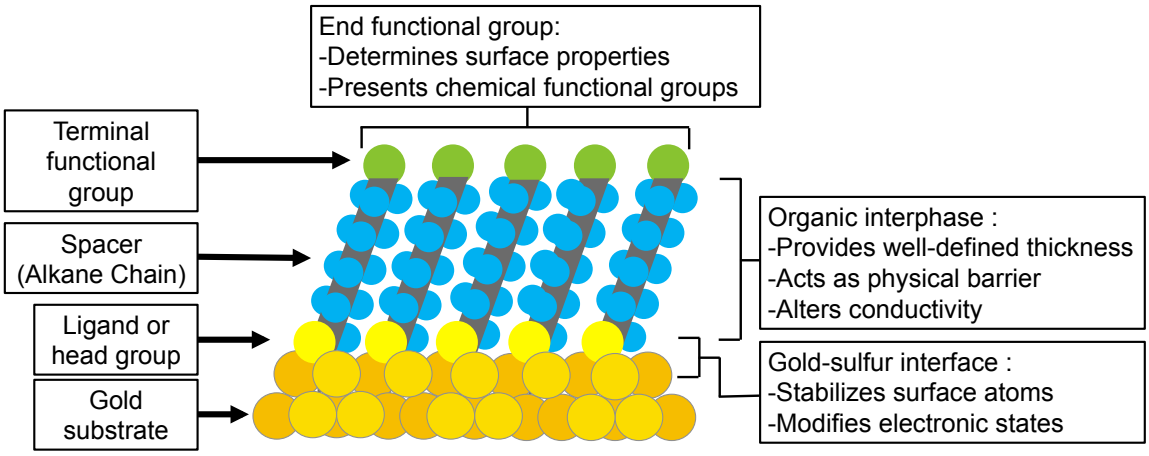

Figure 2.11 – Schematic representation of an ideal, single-crystalline SAM of alkanethiolates supported on a gold surface with a (111) texture. The anatomy and characteristics of the SAM are highlighted.[48]

The resulting strength of the S−Au bond is variable according to the literature. Studies suggest bond energy values start around 125 kJ/mol and go up to 209 kJ/mol.[48] Although the bond strength is relatively high, the adsorption is fully reversible. Indeed, adsorbed thiols or disulfides can desorb during oxidation or alternatively at high temperatures as they have limited thermal stability.[48]

As shown in figure 2.11, the terminal functional group of the SAMs determines the surface properties. Tailoring this terminal functional group allows to make surfaces with

a wide range of organic functionalities (e.g. electroactive, biologically active). Methods to modify SAMs after their formation are critical for the development of surfaces that present large, complex ligands and molecules for biology and biochemistry. Indeed, the synthesis of functionalised thiols is usually laborious and difficult, even for simple molecules. Thus making thiols linked to a peptide, protein, carbohydrate or other biomolecules is a major challenge. To conclude, in most biological or biochemical applications, SAMs are modified after their formation through various methods including among others amide-bond formation, non-specific polymer adsorption and covalent bond breaking.[44] A thiol SAM on a gold substrate can thus be modified to have a protein as part of the terminal group in order to favor cell adhesion.

2.4.2 Polythiols

Polythiols are macromolecules containing multiple thiols on their side chains. The strongest interest in the development of such polymers lies in the fact that they are potential substrates for the incorporation of various chemical functionalities via thiol-click reactions (figure 2.12). Indeed, radical or nucleophilic reactions can produce either a non-cleavable or a cleavable linkage. Moreover thiols can be oxidised to form disulfide links.[12] This oxidation process makes thiols unstable functional groups. To prevent thiol oxidation, thiol functions can be protected by including them for example in thiolactone cycles. Polythiolactones can thus be used as polythiol precursors (figure 2.13). Indeed, deprotection strategies can be employed to release the thiol functions from the thiolactone cycles when needed. However this makes the synthesis of polythiols more complicated.

In this section the challenge of polythiol and polythiol precursor synthesis with protection and deprotection strategies are discussed first. Then, grafting of polythiolactone (i.e. a polythiol precursor) on gold surfaces is briefly reviewed. Next, the redox-responsiveness of polythiols is detailed. Finally, biological applications are described.

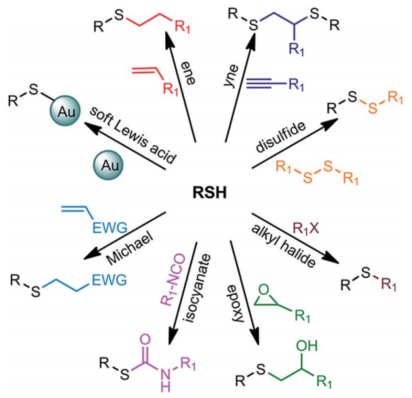

Figure 2.12 – Example of thiol-based reactions used in materials science.[49]

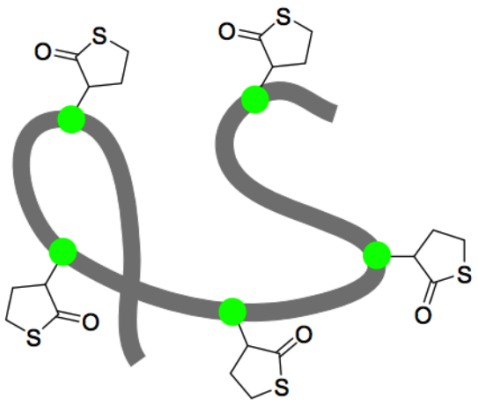

Figure 2.13 – Schematic diagram of a linear poly(thiolactone).[11]

Synthesis

Studies of successful synthesis of polythiol polymers having thiols on their side chains are scarce.[12] The high reactivity of thiols makes them appealing for macromolecular engineering but it also makes them prone to generate side reactions during polymerisation. Therefore synthesis of polythiols is a real challenge.[49]

Interferences of free thiols in both radical and anionic polymerisation processes exclude those routes. Consequently, a protection/deprotection strategy is necessary for polythiols syntheses that are thus usually prepared from protected monomers.[12]

First reports on linear polythiols synthesis date from 1960. They concerned polyurethanes and polyamides with free pendant thiol groups synthetised by polycondensation.[50,51] For polyamides the thiol groups were protected by an O-benzyl thiocarbonate and deprotected by a solution of trifluoroacetic acid saturated with hydrogen bromide. For polyurethanes the thiol moieties were protected with benzyl groups and deprotected with sodium in a mixture of liquid ammonia and propylamine.[49]

Since 1960 methods to synthetise polythiols have evolved. Du Prez and co-workers from Ghent University have studied polythiol synthesis and protection/deprotection techniques. Moreover the same group also reported the synthesis of linear polythiols copolymers. This team developed a clever approach to protect thiols by confining them in thiolactone cycles like N-thiolactone acrylamide for example. This monomer containing protected thiols can then be copolymerised with an acrylamide-based monomer like N-isopropyl or N,N-dimethylacrylamide to obtain linear copolymers carrying pendant thiolactone groups.[11] The copolymerisation can be performed by reversible-addition fragmentation transfer (RAFT) or nitroxide-mediated polymerisation (NMP).[12] These copolymers can then be modified by reacting with nucleophiles such as amines (aminolysis) to unprotect the thiols. Once the thiols are available to react, they can be further functionalised through various thiol-click modifications (figure 2.12).[12,49] The whole synthesis process is illustrated in figure 2.14.

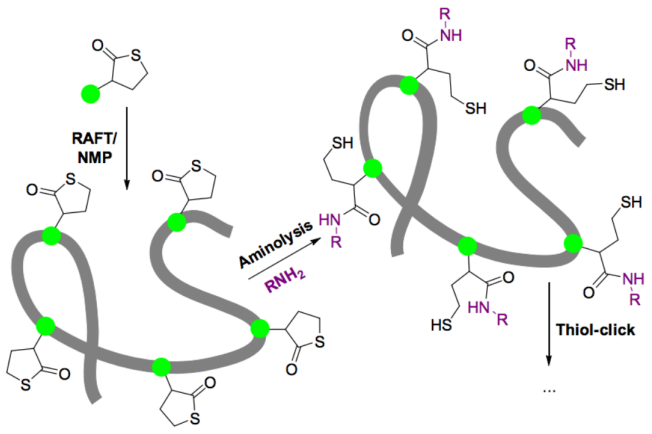

Figure 2.14 – Schematic description of double modification of pendant thiolactone moieties. After RAFT or NMP of a stable vinylic thiolactone monomer, aminolysis of the linear poly(thiolactone) yields a linear polythiol, i.e. a reactive polymer scaffold for thiol-click modification.[11]

Grafting on gold surfaces through aminolysis

Polythiol precursors, like polythiolactones, can be grafted onto gold surfaces. Indeed, polythiolactones were proven to be stable precursors to produce, in one step, stable polythiol layers grafted onto gold surfaces (figure 2.15).[45] This result can be of major interest for various applications because it allows tuning the properties of gold surfaces by combining the stable thiol-gold link and the variety of further thiol modifications.

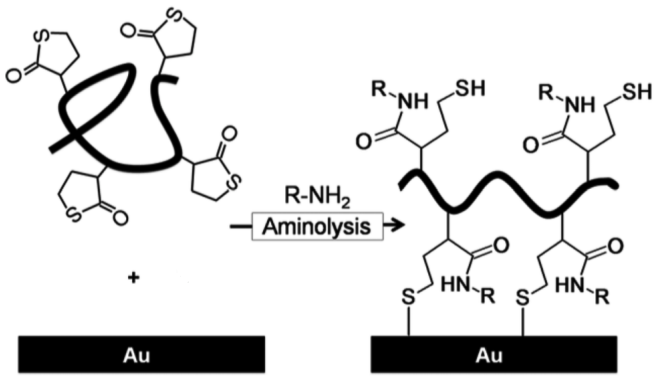

Figure 2.15 – Polythiolactone grafting on gold surface through aminolysis.[45]

Redox-responsiveness

As said previously polythiols can be further modified by various chemistries (figure 2.12). One in particular is disulfide bond formation. This reaction is completely reversible leading to a thiol/disulfide exchange reaction, which is a biological fundamental process.[12] The equation of such process is given below :

$$2\ \mathrm{R-SH} \rightleftharpoons \mathrm{RS-SR} + 2\ \mathrm{H^+} + 2\ \mathrm{e^-}$$

Only mild oxidation of thiols leads to disulfide bonding. Stronger oxidation conditions can give rise to further thiol oxidation with sulfonate formation.[1] Therefore if one wishes to modify polythiols by disulfide bonding, the oxidative agent should be chosen carefully.
On the other hand, cleavage of disulfide bonding can be performed in reductive conditions. To trigger the reduction, reductive agents like dithiols, mercaptoethanol or dithiothreitol (DTT) can be used in excess. A major drawback of using these reductive agents is possible thiol-disulfide interchange. Because the reductive agent is in excess, the equilibrium of disulfide bond formation is drawn to the right in comparison to the equation above.[1] In order to avoid thiol-disulfide interchange, the reductive agent should not be added in too excessive amounts.
To conclude, the reversible disulfide bond formation under redox conditions can bring an additional feature to polythiols namely redox-responsiveness.

Biological applications

Redox-responsive polythiols offer promising potentials in biological applications. This is because the cell medium is reductive and could thus trigger disulfide bond cleavage.
Glutathione (GSH) is a tripeptide (L-γ-glutamyl-L-cysteinyl-glycine) synthesised in the cytosol from the precursor amino acids : glutamate, cysteine and glycine. Animal cells contain millimolar concentrations of GSH (up to 10 mM) that is maintained in the reduced form by a cytosolic NADPH-dependent[c] reaction catalysed by glutathione reductase. Disulfide bonds (e.g. in proteins) rarely form in the cytosol, intracellular medium, because of the high concentrations of GSH. This makes the intracellular medium reductive and disulfide bonds are rapidly degraded.[52]

[c] nicotinamide adenine dinucleotide phosphate

A redox-responsive polythiol could thus be functionalised through disulfide bonding, which is stable in extracellular environment. But once exposed to the reductive medium of the intracellular environment, the disulfide bonds are promptly degraded. This property is of high interest in applications based on compound delivery, including drug delivery, affecting cell behaviour.

Recently it has been proven that polythiolactones grafted onto a gold surface (deprotecting by this way the thiol functions as illustrated in figure 2.15) allowed controlled grafting and release of a thiolated compound of interest.[45] However, no studies have been reported on the releasing of thiolated compounds in the cellular medium by either polythiols or grafted polythiolactones. Instead the use of nanoneedles to deliver compounds inside cells by cleavage of a disulfide link incorporated in an end-functionalised SAM has been investigated.[53] The study proved the successful delivery of fluorescent quantum dots (QDss) in cellular medium. The strategy was to first functionalise gold nanoneedles that could then penetrate inside the cell; details on this strategy are given in figure 2.16. When the nanoneedles penetrate inside the cell, disulfide bonds are cleaved thanks to the reducing environment allowing the release of fluorescent QDss in cytoplasm. This strategy could potentially be adapted to polythiols and precursors (e.g. polythiolactones) by replacing the SAMs by grafted polythiol precursors.

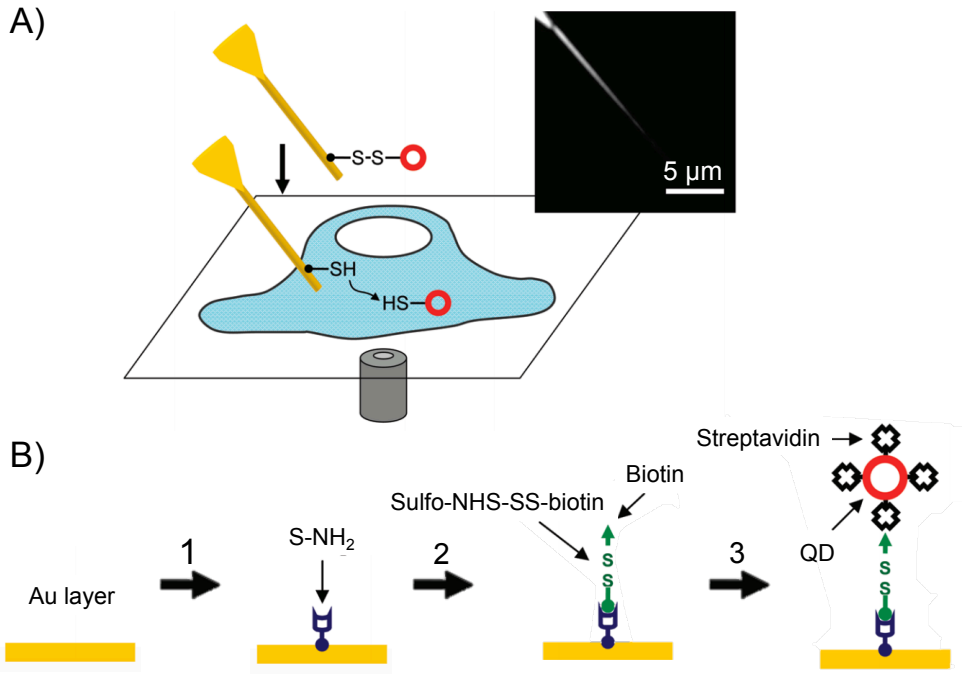

Figure 2.16 – Nanoscale mechanochemical delivery of QDs into living cells. A) Schematic diagram of the mechanochemical delivery of QDs into living cells. Inset, optical microscope image of a typical nanoneedle. B) Procedure for functionalisation of the nanoneedle and surface attachment of QDs. 1) A NH_2-terminated SAM was formed on the Au-coated nanoneedle by the chemisorption of thiols on gold. 2) The nanoneedle was biotinylated by reacting the NH_2 surface group with N-hydroxysulfosuccinimide (sulfo-NHS) esters of biotin (sulfoNHS-SS-biotin), forming a stable amide bond. 3) Streptavidin-coated QDs were attached onto the nanoneedle by the specific binding of streptavidin and biotin.[53]

CHAPTER 3

OBJECTIVES AND STRATEGY

3.1 Towards the design of redox-responsive nanostructured gold surfaces[1]

This master thesis is part of a research project whose main objective is the design of redox-responsive nanostructured gold surfaces for drug delivery applications. To pursue this objective, nanostructured surfaces need to be elaborated. The design of the nanostructure is very important since it is a factor that considerably influences cell behaviour. Once the nanostructure is elaborated, its surface is functionalised by grafting a copolymer layer bearing thiol groups (figure 3.1 step 1) which can be subsequently used to immobilise a substance of interest through a cleavable disulfide link (figure 3.1 step 2). Thereafter these functionalised nanostructured surfaces can be used for drug delivery applications to control cell processes (proliferation and differentiation) through interactions at the nanoscale with the cell (figure 3.1 steps 3 and 4).[1] This drug delivery approach is illustrated for a selective and full functionalisation of the nanopillars in figure 3.1 A and B respectively.

As can be seen in figure 3.1, thiolated compounds are fixed on the copolymer layer by a disulfide bond. This disulfide bond controls the attachment and the release of the drugs in the cytoplasm. Moreover to form this disulfide bond and graft the drug, a thiol functional group is needed. Therefore a copolymer coating incorporating thiol groups is used to functionalise the gold surface. Functionalisation is performed according to a specific strategy : a thiolactone-containing copolymer, thus a polythiol-precursor, was synthesised in collaboration with Ghent University.[45] As already explained in section 2.4.2, this research team developed a clever protection strategy for the thiols by using thiolactone rings. The thiols included in thiolactone rings can be deprotected by aminolysis. Moreover carrying aminolysis in presence of gold, allows the copolymer to react with the gold surface resulting in copolymer grafting while free thiols remain available for drug grafting (figure 3.2). The strategy of combining the deprotection of thiols and the grafting onto the gold surface is called one-pot reaction strategy.

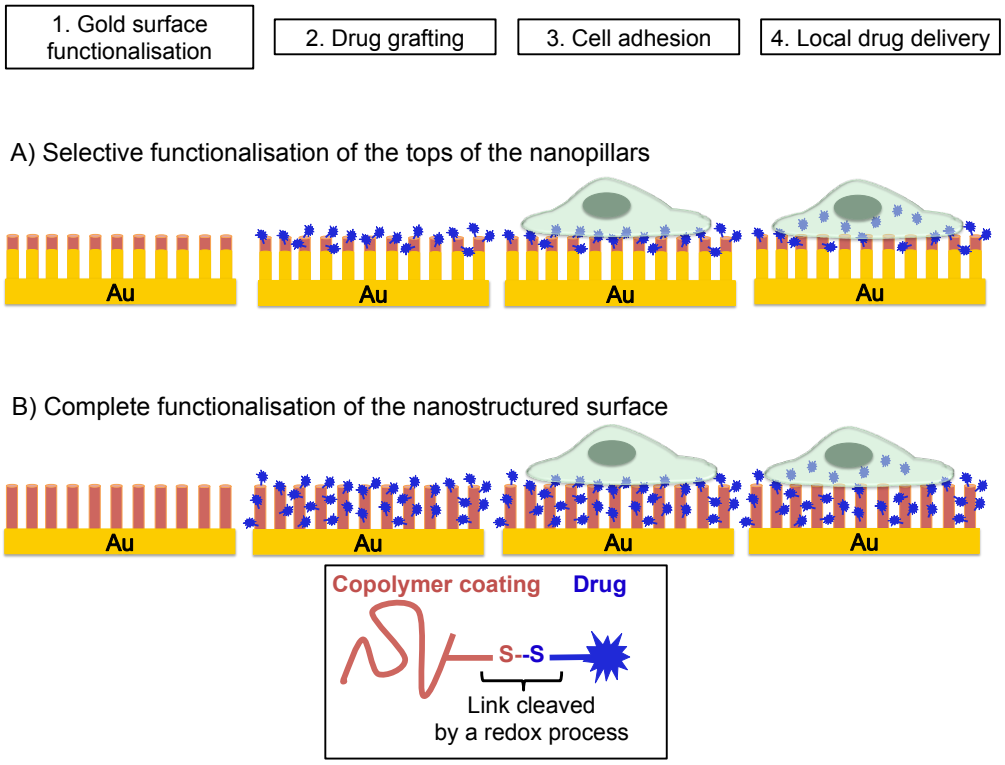

Figure 3.1 – Global strategy for drug delivery application during cell culture. 1. Gold surface functionalisation by copolymer grafting 2. Drug grafting though disulfide bond formation 3. Cell adhesion 4. Local drug delivery into the cell. Two cases are illustrated A and B, namely selective and complete functionalisation of the nanostructured surface respectively.

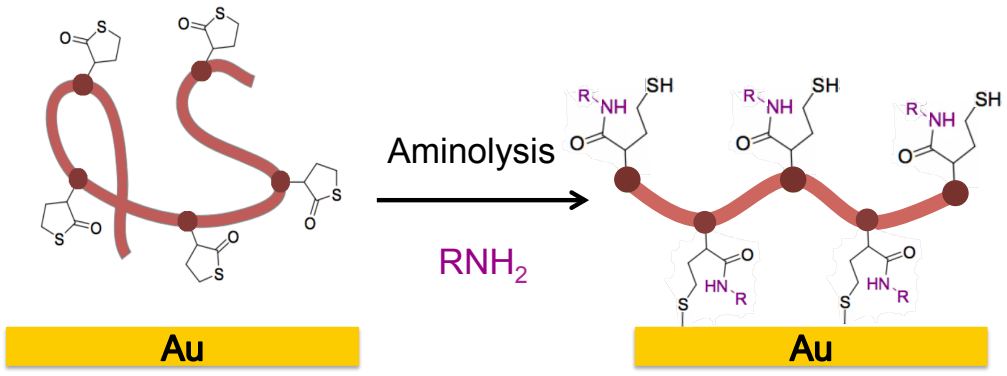

Figure 3.2 – One-pot reaction to immobilise a polythiol derivative on a gold surface.[1,11]

The thiol groups of the copolymer are thus partially used to anchor the chains on the gold surface whereas the remaining ones are available to attach a thiolated substance through a disulfide link in mild oxidising conditions. This reaction is reversible since the disulfide link can be cleaved in reducing conditions. This is illustrated in figure 3.3. However the release of the thiolated substance should happen during cell culture, more precisely when the nanopillars enter into contact with cells. Indeed, as intracellular medium is reductive it should trigger the drug release.

First experiments have been performed on flat gold surfaces used as model surfaces for the optimisation of gold surface functionalisation. The grafting and release of a thiolated compound are hence already optimised. To control if release could indeed occur under reductive conditions, the flat surfaces were put in contact with a reductive solution. The release is verified via electrochemical measurements. As the process is optimised for flat gold surfaces, they will be further used as control surfaces and be compared with results obtained on nanostructured surfaces.

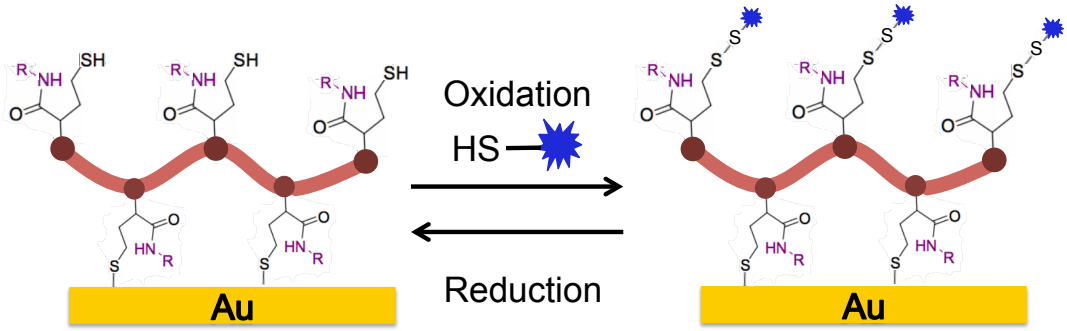

Figure 3.3 – Redox-responsiveness of the polymer coating allows to graft and release a thiolated compound through a disulfide bond.[1,45]

Flat surfaces have already been intensively investigated. Therefore focus is given to nanostructured surfaces. Some key topics to work on are :

- Optimising a selective functionalisation strategy for the nanopillars.
- Optimising the formation of thiolactone-based copolymer layers onto nanostructured gold surfaces.
- Optimising the conditions of grafting and release of a model thiolated compound with nanostructured surfaces
- Study cell adhesion and viability on functionalised flat surfaces and nanopillars
- Control the drug delivery during cell culture

During this master's thesis, we will focus essentially on the first 3 points.

3.2 Functionalisation of the nanopillars

Grafting of thiolactone-based copolymers onto flat gold surfaces using a one-pot reaction has already been optimised by Sabrina Belbekhouche.[45] The gold surface was efficiently covered by the copolymer and the loading and releasing of a thiolated compound under redox stimulation was successful. However only few research has been performed on nanostructured surfaces. Moreover the selective functionalisation of the top of the nanopilars was not yet explored. Indeed, selective functionalisation of the top of the nanopillars could allow specific interactions with cells, at the nanoscale. The resulting performances could be different from the ones obtained with fully functionalised nanopillars.

The strategy developed to selectively and fully functionalise a gold nanostructured surface is illustrated in figure 3.4. To begin, a nanostructured surface with a well-defined pillar geometry and density is elaborated. Then, if selective functionalisation is pursued, a sacrificial PAA film is spin-coated and subsequently plasma treated to reveal only the top of the nanopillars (figure 3.4, A step I). In this approach the tops of the nanopillars are exposed for functionalisation whereas the remaining gold surface is protected by the PAA film. Next, the thiolactone copolymer is grafted on the exposed gold surface (figure 3.4, A step II). After that the PAA film is dissolved (figure 3.4, A step III). If so wished the remaining unfunctionalised gold surface can also be functionalised by a SAM to get bifunctional surfaces (figure 3.4, A step IV). Lastly if the nanostructured gold surface is fully functionalised by the copolymer then the only step to be performed is the thiolactone copolymer grafting as illustrated in figure 3.4, B step I.

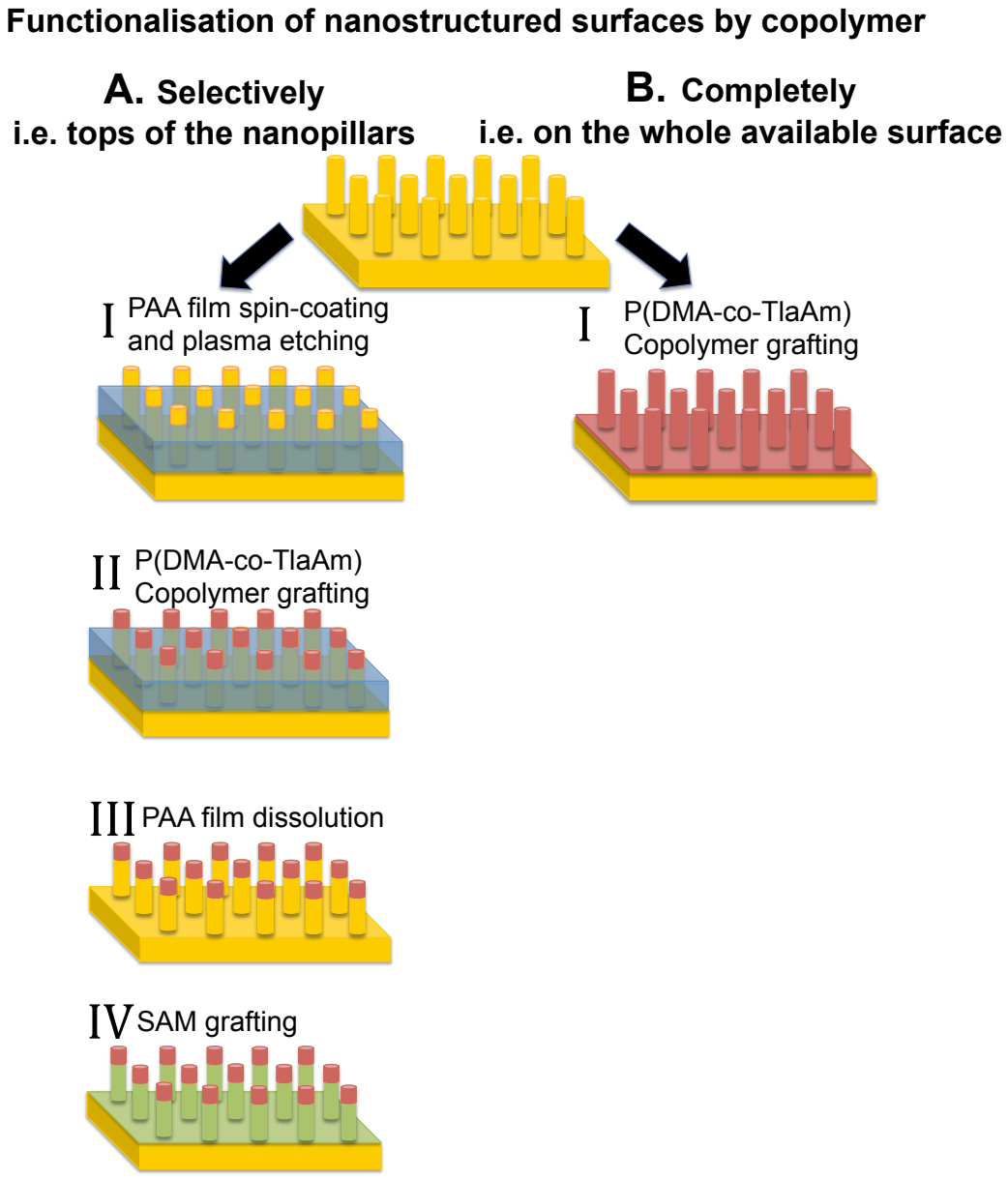

Figure 3.4 – Global strategy for nanostructured gold surface functionalisation.

3.3 Objectives of this master thesis

The first objective of this master thesis is to verify the feasibility of the proposed strategy to selectively functionalise the nanopillars. Thus each step of the strategy will be investigated regarding feasibility. We will also establish protocols for every process we employ and determine optimal process parameters. The resulting selectively functionalised nanostructured surfaces will then be characterised to verify the efficiency of the process. Therefore the presence of the copolymer will be investigated by chemical composition surface analyses.

The second objective of this master thesis is to develop experiments regarding complete functionalisation of nanostructured surfaces. Therefore the efficiency of the copolymer grafting will be analysed together with the grafting and release of thiolated compounds.

Finally, results obtained on selectively and fully functionalised nanostructured surfaces will be compared to each other and to the reference being a functionalised flat gold surface.

CHAPTER 4

MATERIALS AND METHODS

In this chapter, materials and methods used during this master thesis are detailed starting with the used materials (i.e. solvents and products). Then, the applied experimental protocols are described beginning with the elaboration of gold nanopillars, followed by PAA spin-coating and plasma treatment and ending with gold surface modification. Finally, characterisation techniques employed during this work are presented. For classical techniques like atomic force microscopy (AFM) and SEM, only the operating parameters are presented whereas the less common techniques are described in detail in order to facilitate the interpretation of their results.

4.1 Solvents and products

Solvents : Technical sulphuric acid (H_2SO_4) (95 %) was purchased from VWR chemicals. Hydrogen peroxide (H_2O_2) (30 w_t%) was purchased from Chem-Lab. Absolute ethanol (C_2H_5OH) ($\geq$ 99%), methanol (CH_3OH) ($\geq$ 99.8%) and dichloromethane (DCM) ($\geq$ 99.5%) were purchased from AnalaR NORMAPURE ®VWR chemicals. Chloroform ($CHCl_3$) ($\geq$ 99.8%) was purchased from HiPerSolv CHROMANORM ® for HPLC VWR chemicals. Water (H_2O) was purified by Milli-Q ®water purification system with a resistivity of 18.2 MΩ.cm at 25°C.

Products : Ethanolamine (ETA) ($\geq$ 98%), 2-(N-morpholino)ethanesulfonic acid (MES), potassium hexacyanoferrate (II) trihydrate ($K_4Fe(CN)_6.3H_2O$) ($\geq$ 98.5%), potassium hexacyanoferrate (III) ($K_3Fe(CN)_6$) ($\geq$ 99%), 4-(2-hydroxyethyl)-1-piperazineethanesulfonic acid (HEPES) ($\geq$ 99.5%), poly(acrylic acid) (PAA) solution ($M_w\sim$ 10000, 35 w_t% in H_2O), chloramine T (CAT) ($\geq$ 98%), dithiothreitol (DTT) ($\geq$ 98%), 1-Dodecanethiol ($C_{12}H_{26}S$) ($\geq$ 98%), gold (III) chloride trihydrate ($HAuCl_4.3H_2O$) ($\geq$ 99.9%), sodium hydroxide (NaOH) ($\geq$ 97%) were purchased from Sigma-Aldrich. Potassium chloride (KCl) ($\geq$ 99.9%) and potassium hydroxide (KOH) (ca. 85%) were purchased from Acros Organics. Sulfhydryl polyethylene glycol (PEG-SH) (95%) was purchased from Polymer source Inc.

Gold surfaces are modified by grafting a statistical copolymer synthesised in collaboration with the group of Filip Du Prez from Ghent University according to the protocol described in reference [45] . After synthesis, the copolymer was purified by dialysis against water to remove residual monomers. It theoretically contains 30 % of N-thiolactone acrylamide (TlaAm) and 70 % of dimethylacrylamide (DMA). Its chemical structure is shown in figure 4.1. The experimental value of thiolactone incorporated in the copolymer was

measured by X-ray Photoelectron Spectroscopy (XPS) by taking the ratio of the percentage of nitrogen to sulphur and that of oxygen to sulphur resulting in an experimental TlaAm content of 32 %.

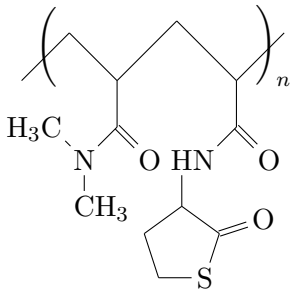

Figure 4.1 – Chemical structure of P(DMA-co-TlaAm).

Finally, the copolymer is named P(DMA-co-TlaAm)-30% in the sequel. After aminolysis in presence of ETA, the copolymer is named P(DMA-co-TlaAm)-30%-SH.[1]

4.2 Elaboration of gold nanopillars

Gold nanopillars were fabricated using a template-based method. For this case, the template is a track-etched PC membrane whose nanopores were filled with gold by electrodeposition (see section 2.2).

4.2.1 Elaboration of flat gold surfaces

Flat gold surfaces were made by evaporating a gold layer (100 nm) on a silicon wafer already coated with a chromium layer (1-2 nm). This chromium layer is supposed to enhance the adhesion of the gold onto the silicon substrate. Furthermore the gold surfaces were laser-cut in squares of dimension 1 $\times$ 1 cm^2 in a clean room environment.

4.2.2 Fabrication of track-etched membrane[1]

The first step to elaborate the template is to spin-coat a ca. 1 μm thick PC layer onto a flat gold surface. The spin-coating solution has a PC concentration of 90 mg/ml using chloroform as solvent. Regarding spin-coating parameters, the speed was set at 4500 rpm with an acceleration of 2250 rpm/s and the spin-coating process lasted for 60 s.
The next step is to anneal the PC film at 190°C during 4 h under vacuum to remove any trace of solvent. Only a part of the PC film (i.e. a circle of 6 mm diameter) is irradiated by heavy ion bombardment (Ar^{9+} at 220 MeV) at the Cyclotron Research Center in Louvain-la-Neuve. The resulting samples have a pore density between 10^8 and 10^9 pores/cm^2.

The second step is the chemical etching to enlarge the pores. Therefore the templates are first immersed in a 1 M NaOH methanol:water 50:50 solution during 10 min. Then, they are rinsed in a 50:50 methanol:water solution at 52°C for 3 min. To improve the wetting a surfactant (Dowfax) is added to the NaOH solution. Moreover, the solutions need to be changed monthly.
After this chemical etching the surfaces are dried under nitrogen. The main parameter determining the pore diameter is the time spent in the NaOH solution. In our case the mean obtained diameter varies between 90 and 120 nm. These values are obtained by SEM analysis of the template surface.

4.2.3 Gold electrodeposition

Once the template is fabricated, gold can be deposited in it. The chosen deposition technique is electrodeposition by cyclic voltammetry (CV). A ChInstruments Chi660 device served as equipment and the experimental set-up is shown in figure 4.2. The electrochemical solution is placed inside a Teflon cell vial together with the platinum counter electrode and the Ag/AgCl reference electrode. This electrochemical solution contains the following compounds : 6 mM $HAuCl_4$, 30 mM KCl and 30 mM K_2HPO_4. Finally, the gold surface, used as working electrode, is sandwiched between two rubbers to ensure that the system is sealed.
With respect to the operating parameters, the potential is swept between 0 and 0.77 V at a scan rate of 0.2 V/s. To finish, the number of potential scans is adapted to obtain the desired pillar height knowing that increasing the number of scans increases the final height.

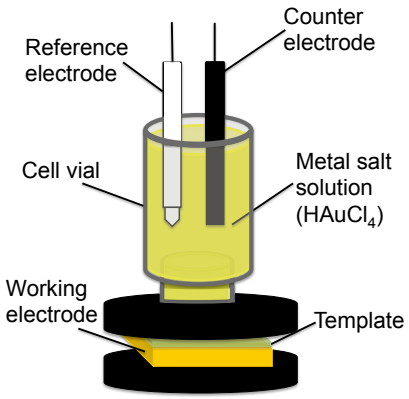

Figure 4.2 – Illustration of the experimental set-up of electrochemical deposition. The three electrodes are also linked to the Chi660 device.

4.2.4 Template removal

In order to efficiently and completely remove the PC template, the following procedure is used. The surfaces are dipped in dichloromethane for 10 min and rinsed with the same solvent afterwards. This step is repeated three times in a row. To finish and make sure all PC traces are eliminated, a 5 min oxygen plasma treatment at 100 W is applied by means of a K1050X RF Plasma Etcher/Asher/Cleaner from Emitech and using air (O_2/N_2) as gas.

4.3 Spin-coating

Spin-coating was performed to deposit a sacrificial layer of PAA, which purpose is to partially protect the gold surface to graft selectively the tops of the nanopillars with the copolymer layer. Spin-coating was performed on surfaces decorated with gold nanopillars and silicon wafers (reference surfaces) by using a PAA solution. The silicon wafers were used for thickness calibration because film thickness measurements are performed by ellipsometry, which is not compatible with gold surfaces. The procedure relating to the PAA solution preparation is detailed in this section as well as the PAA spin-coating itself.

4.3.1 Preparation of PAA solution

PAA is purchased as a water solution with a PAA concentration of 35 % wt. The spin-coating solutions have the following chosen concentrations : 2.5, 5, 6.5, 7.5 and 10 % (w/v). The PAA solution of 35 % wt needs thus to be diluted at the desired concentrations. As PAA is too viscous to be withdrawn by pipette, it is taken with a spatula. Because the volume cannot be evaluated without a pipette, the mass is measured and the volume is deducted by using the density of the 35 % wt solution : 1.14 $\frac{g}{ml}$. The final volume to reach is calculated by dividing the PAA mass by the desired concentration. To finish, the amount of water to add is simply the difference between the final and the initial volume. To summarise, the calculations and formulas are :

1. M_{paa}= 0.35 M_i
2. $V_i = \frac{M_i}{1.14 \frac{g}{ml}}$
3. $V_f = \frac{M_{paa}}{C_{desired}}$
4. $V_{eau} = V_f$ - V_i

- M_{paa} : PAA mass
- M_i: Mass of the 35 % wt PAA solution
- V_i : Initial volume
- V_f : Final volume
- $C_{desired}$: Desired concentration in w/v

The calculated amount of water is added so as to dilute the solution, which is then stirred with a magnetic barrel during 20 min. After that the pH of the solution is brought from 2 to 6-7 by using a basic KOH solution with a concentration of 8.93 mol/l (500 g/l)[a]. The pH is measured by a pH indicator paper. Finally, the solution is again stirred for 30 min and afterwards the pH is measured again to be sure that it is stabilised. Once the PAA solution has a stable pH, it is filtered through an Acrodisc ®syringe filter having a pore size of 0.2 μm. This filtration is performed under a laminar flux hood in order to avoid dust. The solution is then stored into a class 1/ISO 3 clean room and can be used for maximum 2-3 months.

4.3.2 PAA spin-coating

Before spin-coating, the surface to be spin-coated needs to be cleaned and prepared according to the following process.

Gold surface

1. Rinsing with MilliQ water then ethanol followed by drying under nitrogen stream. This step is repeated 3 times.
2. UV-ozone during 20 min
3. Rinsing with ethanol followed by drying under nitrogen stream.

Silicon surface

1. Cutting of a silicon wafer with a diamond tip into square(s) of 1× 1 cm^2
2. Rinsing with MilliQ water and methanol
3. Gentle rubbing with a Kimtech wiper to remove impurities
4. Rinsing with methanol followed by drying under nitrogen stream
5. UV-ozone during 15 min

[a]To be perfectly rigorous, the volume of KOH should be substracted from the volume of water to add.

Next, the surfaces are spin-coated in a class 1/ISO 3 clean room (Winfab, UCL) which is the micro- and nanofabrication platform of UCL. The used equipment is a model WS-650MZ-23NPP/LITE apparatus from Laurell.

The surface is placed onto the sample holder and maintained by vacuum sucking. Then, the PAA solution is deposited by pipette onto the surface and the coater starts to spin. The parameters that can be chosen by the operator are : the volume of solution deposited, the speed (rpm), the acceleration (rpm/s) and the time (s). These parameters were optimised by calibration to obtain the desired thickness and were fixed at 40 μl of PAA solution spin-coated at 1750 rpm with 875 rpm/s as acceleration during 60 s.

After spin-coating, the surface is baked at 150 °C on a hot plate to evaporate the solvent, in our case water.

4.4 Plasma treatment

After the spin-coating step, the surface undergoes a plasma treatment to partially etch the PAA film. In this way, tops of nanopillars are exposed as shown in figure 4.3. The equipment is a K1050X RF Plasma Etcher/Asher/Cleaner from Emitech using air (O_2/N_2) as gas. The parameters to be chosen are the time and the power in W. Measuring the thickness of PAA films deposited on silicon wafers before and after the plasma treatment allows quantification of polymer etching. We used a 2 min plasma treatment at 100 W in order to remove ca. 50 nm thickness of polymer.

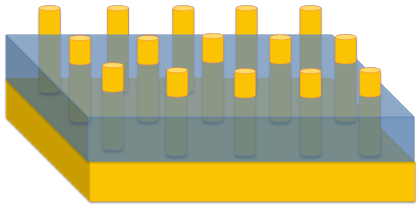

Figure 4.3 – Illustration of a nanostructured surface spin-coated with PAA film then exposed to plasma treatment to reveal the tops of the nanopillars.

4.5 Gold surface modification

Nanostructured gold surfaces are chemically modified by P(DMA-co-TlaAm)-30% copolymer and SAM[b] grafting. These graftings are detailed in this section as well as the PAA film dissolution and the assessment of the redox-responsiveness of P(DMA-co-TlaAm)-30% copolymer. All steps are given in the order in which they are performed although each step is not necessarily performed.

4.5.1 Copolymer grafting

P(DMA-co-TlaAm)-30% copolymer was grafted onto flat and nanostructured gold surfaces. The one-pot grafting reaction with opening of thiolactone cycles by aminolysis with ETA is shown in figure 4.4.

[b]In this work, dodecanethiol was chosen as model molecule for SAM grafting.

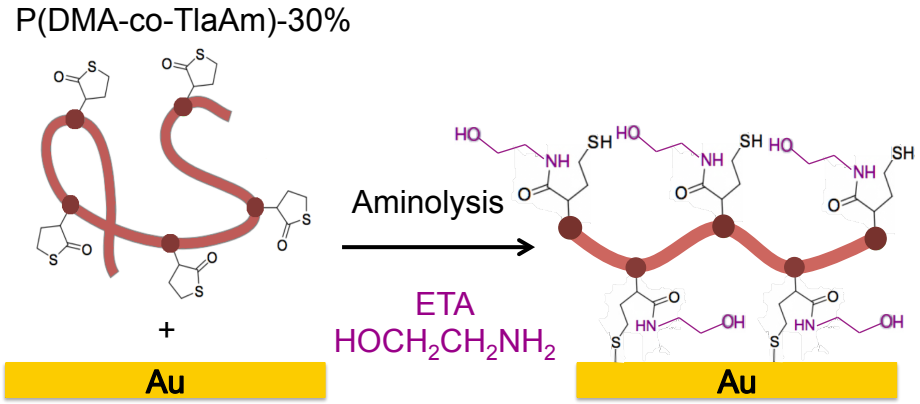

Figure 4.4 – One-pot reaction to immobilise P(DMA-co-TlaAm)-30% copolymer on a gold surface by aminolysis using ETA.

Moreover either the nanostructured surfaces were completely covered by the copolymer layer or only the tops of the nanopillars were grafted (figure 4.5). Of course, flat surfaces or nanostructured surfaces fully covered by the copolymer did not undergo either the spin-coating nor the plasma treatment. Furthermore those surfaces will not undergo the following steps after grafting of copolymer : PAA film dissolution and SAM grafting.

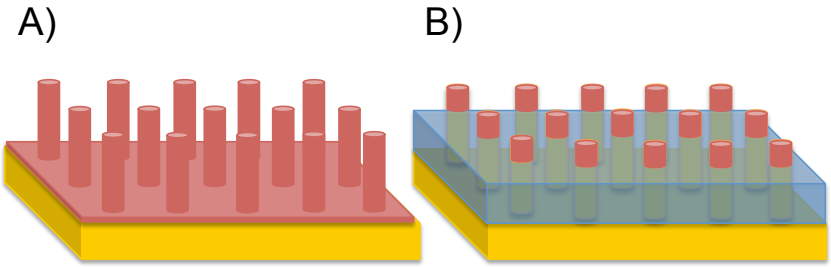

Figure 4.5 – Illustration of the copolymer grafting. A) Nanostructured surface with full coverage. B) Nanostructured surface with partial coverage (only the tops of the pillars).

The experimental procedure for copolymer grafting is based on the work done by Sabrina Belbekhouche.[45]
First, the gold surface to be modified is cleaned. The cleaning starts by rinsing with MilliQ water and ethanol, then the surface is dried under nitrogen stream. This step is repeated 3 times for each surface. After that a UV-ozone treatment is applied for 20 min. The surface is rinsed again to remove the remaining oxide and dried under nitrogen stream.

Next, the copolymer solution is prepared in a glass vial previously washed with piranha solution[c]. 5 mg of P(DMA-co-TlaAm)-30% copolymer is dissolved in 5 ml chloroform and stirred with a magnetic stirrer until complete dissolution. In the meantime a solution of ethanolamine made of 50 μl ethanolamine dissolved in 450 μl chloroform is prepared. After that 15 μl of ethanolamine solution, corresponding to 2 molar equivalents of TlaAm units, is added to the P(DMA-co-TlaAm)-30% copolymer solution. The

[c]The piranha treatment is a mixture 2:1 of sulfuric acid and hydrogen peroxide

resulting mixture is stirred for 30-40 s with a magnetic stirrer. Finally, the gold surface is immersed for 2 h. At the end of the reaction, the surface is gently removed from the reaction medium and rinsed with chloroform, ethanol, MilliQ water and ethanol. To finish the surface is dried under nitrogen stream.
CV is then performed to control if the grafting has succeeded.

4.5.2 PAA film dissolution

In case the purpose is to modify only the top of the nanopillars by P(DMA-co-TlaAm)-30% copolymer grafting, a sacrificial PAA layer is spin-coated and etched by plasma treatment (see section 4.3 and 4.4). This layer needs to be removed after copolymer grafting (figure 3.4, step III). Therefore the surface is immerged in 15 ml fresh MilliQ water at pH∼7. The pH of the water is adjusted by adding a small amount of diluted KOH solution and is measured by a pH meter. After 3 h of PAA dissolution in water, the surface is gently removed, rinsed with water and ethanol and finally dried under nitrogen stream. CV is then performed to see how the copolymer grafting on top of nanopillars influences the electrochemical results.

4.5.3 SAM grafting

A dodecanethiol layer, chosen as SAM model molecule, was grafted on some nanostructured surfaces for which the tops of the pillars were first modified with P(DMA-co-TlaAm)-30%-SH. The surfaces obtained after both grafting steps (thiolactone copolymer and dodecanethiol) show both nanotopographical and chemical patterns (figure 4.6). Dodecanethiol has been selected as a model molecule to provide a chemical contrast between the top of the nanopillars and the background of the nanostructured surface.
Experimentally, the nanostructured surface is immerged in a dodecanethiol solution after PAA film dissolution. This solution has a concentration of 20 mM and the used solvent is ethanol. The reaction time is one night thus ca. 16 h. Next, the surface is gently removed from the solution and rinsed with ethanol followed by drying under nitrogen stream. CV is then performed to control if the grafting has succeeded.

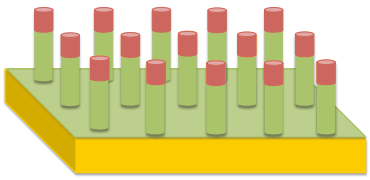

Figure 4.6 – Illustration of a gold nanostructured surface grafted with both P(DMA-co-TlaAm)-30% copolymer (red) and dodecanethiol (green).

4.5.4 Grafting and release of PEG-SH from the copolymer layer

The assessment of the redox-response of P(DMA-co-TlaAm)-30%-SH copolymer consists of grafting and subsequent release of PEG-SH molecules verified by electrochemical impedance spectroscopy (EIS). The protocol and operating conditions were optimised during the work of Sabrina Belbekhouche[45] and are further investigated by Claire Chattaway.[1] The procedure is detailed below.

The drug release strategy relies on the formation (drug attachment) and breaking (drug release) of a disulfide bonding between the thiol pendant groups of P(DMA-co-TlaAm)-30%-SH and a thiolated compound that simulates the drug. The disulfide bond

formation is done by selective thiol oxidation. The oxidising agent needs to be mild and selective for disulfide formation in order to avoid further oxidation. Next, the disulfide bond breaking needs to be investigated. In theory cell medium should allow the drug release. This is practically investigated by releasing a thiolated compound in a reductive medium simulating the cell medium.

The chosen oxidising agent for grafting of PEG-SH, a thiolated compound, is chloramine T (CAT).[45] The choice is based on the fact that CAT is highly selective for disulfide bond formation according to the literature.[54] The reducing agent for the release of PEG-SH is dithiothreitol (DTT),[45] which is a reducing agent. Thus DTT allows the reduction of the disulfide bonding between the copolymer P(DMA-co-TlaAm)-30% and PEG-SH by the disulfide formation of DTT. The chemical structures of CAT and DTT are shown in figures 4.7 and 4.8 respectively.

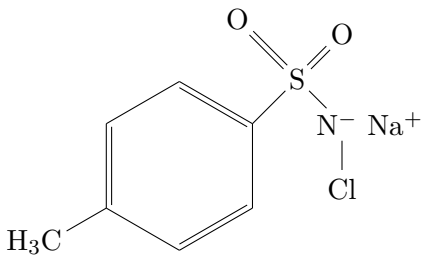

Figure 4.7 – Chloramine T.

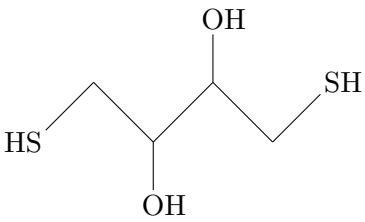

Figure 4.8 – Dithiothreitol.

The grafting and release of PEG-SH molecules is performed directly in an electrochemical cell. Thanks to that EIS measurements can be done on-line limiting the variability inherent to this technique. This is done according to the following experimental protocol.
To begin the following solutions are freshly prepared :

- MES solution : 10 mM MES solution using MilliQ water as solvent. The pH is adjusted to 6 using KOH solution and measured with a pH meter.
- Oxidation solution : 2 mM CAT solution using MES solution as solvent.
- Reduction solution : 2 mM DTT and 10 mM HEPES as buffer using MilliQ water as solvent. The pH is adjusted to 7.2 using KOH solution and measured with a pH meter.
- PEG-SH solution : ca. 3 mg/ml MES solution.

Subsequently the oxidation or PEG-SH grafting is performed by depositing 50 μl PEG-SH solution onto the gold surface and by adding oxidation solution so as to fill the electrochemical cell. The reaction is pursued for 2 min during which the electrochemical cell is stirred by a rotating plate. After that, the cell is emptied and rinsed three times with water. Then, EIS is performed.
Thereupon the reduction or PEG-SH release is done by filling the electrochemical cell with the reduction solution. This reduction reaction is performed for 10 min while stirring the cell on a rotating plate. After this, the electrochemical cell is emptied and rinsed three times with water. EIS is again performed.
To finish, the surface is removed from the electrochemical cell and rinsed with ethanol to be dried under nitrogen stream.

4.6 Characterisation techniques

The characterisation techniques used in this master thesis are described in this section. Common techniques are briefly described whereas the others are discussed in detail.

4.6.1 Electrochemical techniques

Electrochemical techniques were intensively used for three processes. First, to fabricate gold nanopillars by electrochemical deposition. Secondly, to characterise the gold surfaces after grafting of P(DMA-co-TlaAm)-30% copolymer and SAM (dodecanethiol). Thirdly to follow the grafting and release of PEG-SH. Specifically two electrochemical techniques were employed : Electrical Impedance Spectroscopy (EIS) and Cyclic Voltammetry (CV). The first one is very sensitive and the obtained results can vary from one measurement to another. It was used to follow the grafting and release of PEG-SH. The second one is less sensitive and was used to characterise the electrochemical deposition or the gold surfaces before and after chemical surface modifications. The principle of electrochemical techniques is explained in detail in this section and focus is given to CV and EIS.

Principle[55]

Electrochemical techniques link electricity and chemistry by measuring electrical quantities (current, potential or charge) and their relationship to chemical parameters. These techniques require at least two electrodes but in most techniques three are used : a working electrode, a reference electrode and a counter electrode. The working electrode corresponds, in this case, to the surface of interest. The reference electrode has a stable and well-known potential and is therefore used to control and measure the potential of the working electrode in the electrochemical cell. The counter electrode allows current to flow between the working and the counter electrode by functioning as a cathode when the working electrode is operating as an anode and vice versa. The two principal types of measurements are potentiometric-the potential is measured-and potentiostatic-the current is measured. In this work, a potentiostat will be used.

Controlled-potential techniques study the charge transfer processes at the electrode-solution interface and are based on dynamic (non-zero-current) situations. The electrode potential is used for electron transfer reactions and the resulting current is measured. This current reflects the rate at which electrons move across the interface electrode-solution.

The current can be faradaic if it results from the change in oxidation state of the electroactive species (reduction or oxidation of the analyte). The name comes from the fact that the current obeys Faraday's law i.e. the reaction of 1 mole of substance involves a change of n $\times$ 96.487 C. This means that the faradaic current is a direct measurement of the rate of the redox reaction. The pathway of the electrode reaction can be complicated and the final reaction rate depends on the slowest step. Simple reactions only involve three steps :

1. Mass transport of electroactive species to the electrode surface
2. Electron transfer across the interface
3. Transport of the product to the bulk

Complex reaction rates can also be limited by additional chemical and surface processes. But here focus is given to simple reactions. In such cases, the electrode reaction can be

limited either by mass transport either by electron transfer. If mass transport limits the reaction rate, the reaction is called nernstian.

Non-faradaic processes also contribute to the current. The electrodes will be positively or negatively charged and attract opposite charged ions to neutralise the electrode-solution interface. Consequently a double layer will be formed around the electrode. The first layer, called the inner layer, is made of specifically adsorbed ions whereas the second layer, called the outer layer, is made of solvated ions non specifically adsorbed and attracted to the surface of the electrode by long-range Coulomb forces. This electrical double layer resembles a capacitor and can thus be charged. If so it is responsible for background current and limits the detectability of controlled potential techniques. This double layer charging process is non-faradaic because electrons are not transferred across the electrode–solution interface. It occurs when potential is applied across the double layer or when capacitances are changing.

Focus is given on faradaic current and non-faradaic currents are neglected.
In case of a bare gold surface, the reaction rate, linked to the faradaic current, will depend on mass transport. This mass transport can be split in three contributions :

1. Migration : driven by an electrical field affecting charged particles
2. Convection : driven by external mechanical energy (e.g. stirring, rotating, flowing)
3. Diffusion : driven by concentration gradients

During our analyses no external mechanical energy is applied; so convection can be neglected. Diffusion is taken into account in the outer layer of the electrode. Finally, migration is limited by the introduction of an inert electrolyte at a concentration much larger than the electroactive species.[1]
In case of modified gold surfaces by P(DMA-co-TlaAm)-30% copolymer and SAM (e.g. dodecanethiol) grafting, the reaction rate is limited by the electron transfer rate and no longer by mass transport. This is because the grafted layer acts as a blocking film.

Cyclic voltammetry (CV)

CV is a widely used technique to acquire qualitative electrochemical information. It consists of scanning linearly the potential of a working electrode in a solution without stirring. The potential thus varies between two chosen potentials at a fixed scanning rate (linear scanning). The potential has a triangular waveform and can be made of multiple cycles if desired (see figure 4.9). During this potential sweep, the equipment called a potentiostat measures the current resulting from the applied potential. Measurements are represented in a current-potential plot called cyclic voltammogram.[56]

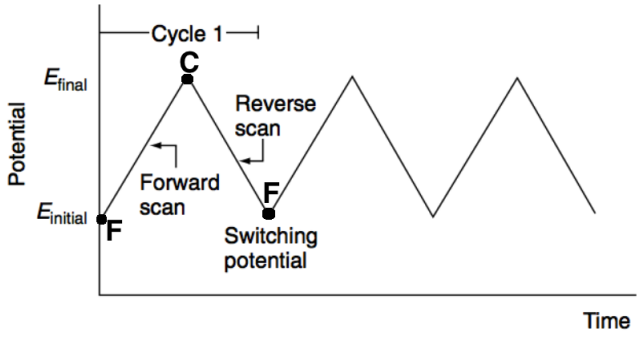

Figure 4.9 – Potential–time excitation signal in a CV experiment.[56]

An example of an experimental response of a bare gold surface during a single potential cycle is showed on figure 4.10. If only the oxidised form of the redox couple is initially present, a negative-going potential scan (forward scan) is chosen for the first half cycle. The second half cycle is consequently a positive-going potential scan (reverse scan). In the example shown on figure 4.10 the system is nernstian, thus controlled by mass transfer.

Starting from point F on figure 4.10, as the potential approaches the characteristic potential E° for the redox process a cathodic current begins to increase (between F and A) until a peak is reached (B).[56] During this first part of the voltammogram, analytes are oxidised at the electrode depleting their concentration near the surface. Moreover the solution is not stirred thus mass transport will mainly occur by diffusion. Since this mode of transport is slower than the reaction rate, it cannot maintain steady-state concentrations near the electrode. As the distance that reactants must travel to reach the electrode increases, the rate of mass transport decreases. This prevents the current from increasing exponentially with potential. When the mass transport becomes rate determining, the current reaches a maximum. Because the concentration gradient continues to decrease, mass transport also decreases and current decays and becomes time dependent. Then, at point C the scan direction is reversed. However the current is still anodic because the potential is positive enough to cause oxidation. Finally, when point D is reached, the current becomes negative, cathodic, resulting in the reduction of analytes. A diffusion controlled current peak is observed.[57]

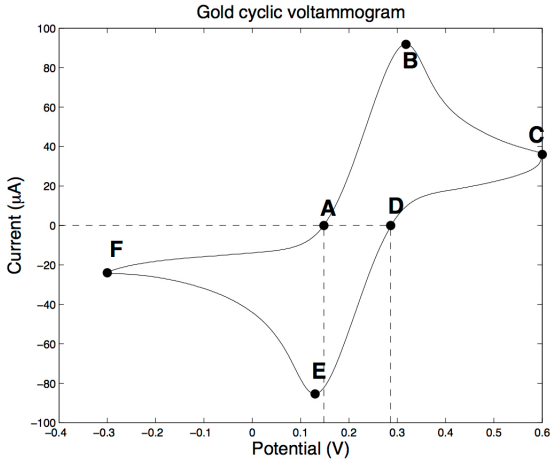

Figure 4.10 – Experimental cyclic voltammogram for a bare gold surface as working electrode, a platinum counter electrode and Ag/AgCl reference electrode with a solution of 1 mM $Fe(CN)_6^{-3}/Fe(CN)_6^{-4}$ and 0.1 M KCl.

Now that the cyclic voltammogram of a bare gold surface was detailed, focus is given to modified gold surfaces. Indeed, in our approach, nanostructured gold surfaces are coated by a copolymer layer acting as a blocking film. Thus the reaction rate will no longer be controlled by mass transport but by electron transfer rate. Consequently, the diffusion controlled peaks will no longer be observed. The obtained cyclic voltammogram will highly depend on the gold surface coverage. This is shown on figure 4.11.

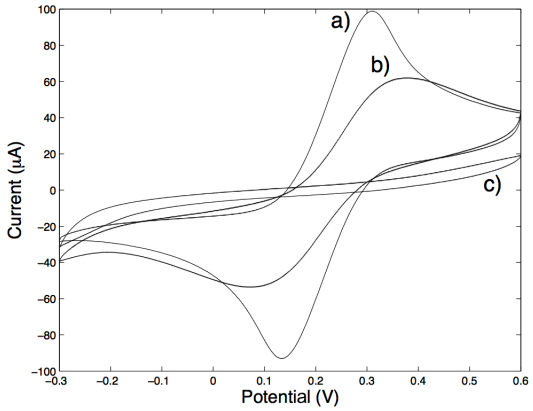

Figure 4.11 – Experimental cyclic voltammogram for a) a bare gold surface b) a partially covered gold surface c) an almost completely covered gold surface.

Indeed, the more the surface is covered by a blocking film acting as a resistance to electron transfer, the lower the surface area of the cyclic voltammogram becomes. This last area can thus give a quantitative information about the surface coverage by a blocking film. This brings us to the definition of the blocking factor (BF)[1] :

$$\mathrm{BF} = \frac{A_{bare} - A_{cov}}{A_{bare}} \cdot 100\ [\%]$$

Where A_{bare} is the surface area of the cyclic voltammogram of a bare gold surface and A_{cov} the surface area of a covered gold surface, in this case by copolymer grafting. The BF gives a quantitative value for gold surface coverage : the higher the BF the more the surface is covered.

Experimental parameters CV was performed with a potentiostat ChInstruments Chi660B. The experimental set-up is shown on figure 4.12 and comprises a Teflon cell vial, a rubber disc to ensure a good sealing without any leak of electrolytic solution, an Ag/AgCl reference electrode, a platinum counter electrode and the gold surface (to be characterised) acting as working electrode. All electrodes are linked to the potentiostat Chi660B.

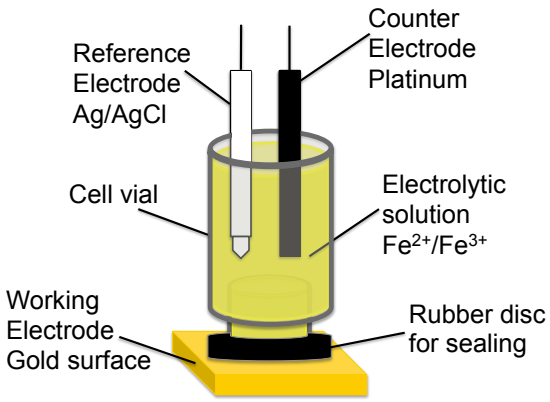

Figure 4.12 – Experimental set up of CV.

The electrolytic solution was composed of the redox couple Fe^{2+}/Fe^{3+}. More precisely, the solution has 1 mM of $C_6FeK_4N_6.3H_2O$, 1 mM of $C_6FeK_3N_6$ and 0.1 M KCl as buffer. MilliQ water is used as solvent and the solution is only used for maximum 5 days. Moreover the solution is purged with an inert gas (nitrogen) for 10 min before usage. This is done to remove the oxygen of the solution because oxygen can be reduced to hydrogen peroxide during electrochemical measurements. This hydrogen peroxide can then be reduced to water. Reactions are given below :

$$O_2 + 2H^+ + 2e^- \rightarrow H_2O_2$$
$$H_2O_2 + 2H^+ + 2e^- \rightarrow 2H_2O$$

The background current created by these reactions interfere with the measurement of many analytes. In addition, the products of the oxygen reduction may also affect the electrochemical process investigated.[58]Therefore it is important to remove oxygen in order to minimise background current.

To conclude the experimental operating conditions are listed below :

- Initial potential : 0.2 V
- High potential : 0.6 V
- Low potential : -0.3 V
- Initial scan polarity : positive
- Scan rate : 0.1 V/s
- Sweep segments : 20
- Sample interval : 0.001
- Quiet time : 0
- Sensitivity : 10^{-4}

Electrochemical Impedance Spectroscopy (EIS)

First of all, impedance is defined as the totally complex resistance when a current flows through an electrical circuit composed of resistors, capacitors or inductors.[56]
In EIS a sinusoidal signal of potential with a small amplitude is applied to the system in a wide range of frequencies and the current response is measured. Because of the low amplitude of the signal, the system remains in quasi-equilibrium state. Therefore properties can be measured without being disturbed. Moreover the frequency sweep affects the rate constant of the different reaction steps resulting in possible separation of mass transport, charge transfer and chemical reaction.[59] The excitation potential can be written as

$$E(t) = E_0 \cos(\omega t) \text{ or } E(t) = E_0 \exp(j\omega t)$$

with E(t) the applied potential at the time t, E_0 the potential amplitude and ω the angular frequency. If the system is linear, the current output signal I(t) has an amplitude I_0 and is phase shifted by ϕ.[59]

$$I(t) = I_0 \cos(\omega t - \phi) \text{ or } I(t) = I_0 \exp[j(\omega t - \phi)]$$

Then, using Ohm's law, the impedance can be expressed as a complex number,

$$Z(\omega) = Z_0 \exp(j\phi) = Z_0 (\cos\phi + j \sin\phi)$$

were $Z_0 = E_0/I_0$. If the imaginary part of the impedance is plotted versus the real part, one obtains the Nyquist plot. An example of an electrical circuit and the corresponding impedance representation by a Nyquist plot is shown on figure 4.13.

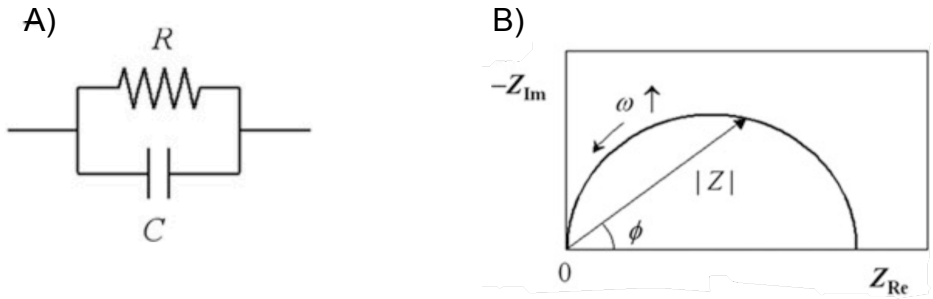

Figure 4.13 – A) Electrical circuit. B) Equivalent Nyquist plot.[59]

In an electrochemical cell, the different reaction steps affecting the impedance can be modelled by electronic circuit components. One of the simplest and most used model for interfacial phenomena in electrochemical cells is the Randles electronic equivalent-circuit (figure 4.14 A). It includes the double layer capacitance, C_d (already discussed in section 4.6.1 : Principle), the ohmic resistance of the electrolyte solution, R_s and the charge transfer resistance, R_{ct}. A variation of this circuit can be obtained by the addition of the Warburg element resulting from the diffusion of ions from the bulk solution to the electrode surface (figure 4.14 B).[56]

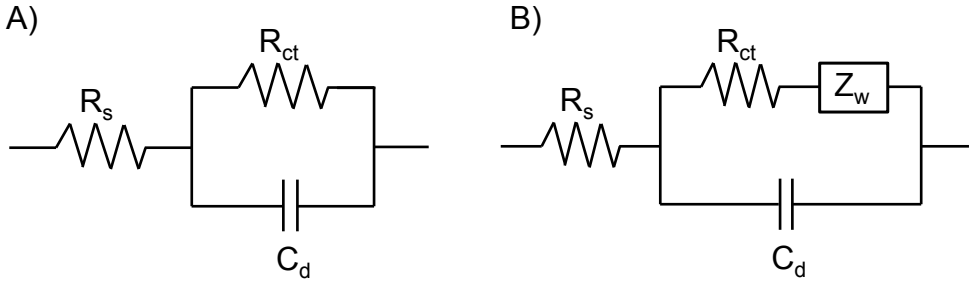

Figure 4.14 – A) Randles circuit. B) Randles circuit including the Warburg element.

Each of the electric components can be identified on a Nyquist plot (if the chosen model is correct). In that way the electrochemical cell properties that were modelled by an electric component can be determined. This is shown on figure 4.15. Indeed, when knowing the electrical circuit, the impedance can be deducted by using Ohm and Kirchhoff's law. For example, in case of the Randles circuit (figure 4.14 A), impedance is written as[59]

$$Z = R_s + (R_{ct}^{-1} + j\omega C_d)^{-1} \text{ or } Z = Z_{Re} + j\ Z_{Im}$$
$$\text{With } Z_{Re} = R_s + R_{ct}/(1 + \omega^2\ C_d^2\ R_{ct}^2)$$
$$\text{and } Z_{Im} = \omega\ C_d\ R_{ct}^2/(1 + \omega^2\ C_d^2\ R_{ct}^2)$$

Moreover

$$[Z_{Re} - (R_s + R_{ct}/2)]^2 + Z_{Im} = \frac{R_{ct}^2}{4}$$

which is the equation of a circle with a diameter of $\frac{R_{ct}}{2}$ corresponding to the Nyquist plot shown in figure 4.15 A. If the Warburg element is added the impedance equation

varies and the resulting plot is shown on figure 4.15 B. The equations are more complex and will not be discussed here as the principle and methodology of the calculations were already explained.

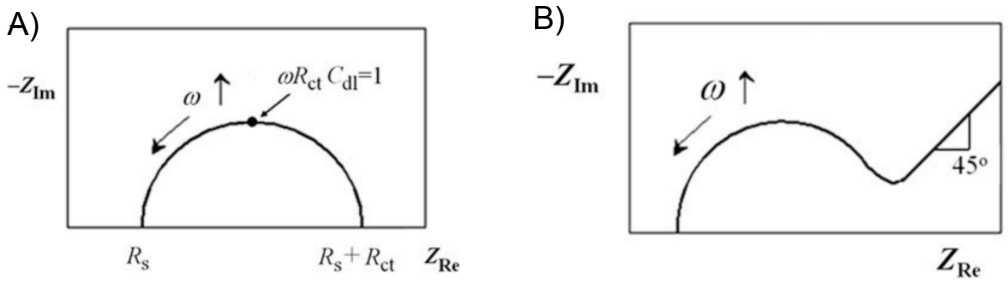

Figure 4.15 – A) Nyquist plot for Randles circuit. B) Nyquist plot for Randles circuit including the Warburg element.[59]

With respect to the electrochemical cell parameters, the solution resistance, R_s, mainly depends on ionic concentration and nature, as well as on the temperature and cell geometry. Moreover, the charge transfer resistance, R_{ct}, is associated to faradaic processes (discussed earlier in this section) : electrons in the electrode encounter reactants at a certain rate determined by the charge transfer resistance. And finally the Warburg impedance represents the mass transfer resistance due to diffusion.

In this study, both Nyquist plots shown on figure 4.15 were encountered. However experimental plots can slightly vary from the theoretical plots due to experimental interferences. The first plot (figure 4.15 A) is typically encountered when the P(DMA-co-TlaAm)-30% copolymer is grafted onto the surface. Indeed, the copolymer can be modelled as a charge transfer resistance and thus increases significantly the intrinsic charge resistance of the system. Consequently the Nyquist plot is dominated by the charge transfer resistance and has a shape close to a semi-circle with a large diameter. Whereas the second plot (figure 4.15 B) is typically obtained with bare gold surfaces. In that case, the resistance to charge transfer is low resulting in a small half circle but the mass transfer resistance is high. The principal mass transfer occurs by diffusion, so the Warburg element must be taken into account and the typical straight line with a slope of 45° will appear.

Experimental parameters The experimental parameters regarding electrolytic solution preparation and use are exactly the same as for CV and will thus not be detailed again. Furthermore, the experimental set up is also identical. A major difference with CV is that EIS has a high variability. Consequently measures are only made after a 30 min period during which the surface to be analysed stays in contact with the electrolytic solution. In this way the system can stabilise to equilibrium before EIS is performed.

To finish the experimental operating conditions are listed below :

- Initial potential : 0.2 V
- High frequency : 100 000 Hz
- Low frequency : 0.01 Hz
- Amplitude : 0.01

- Quiet time : 0
- Sensitivity : 10^{-4}

4.6.2 X-Ray Photoelectron Spectroscopy (XPS)

X-Ray Photoelectron Spectroscopy was used to characterise nanostructured gold surfaces after surface modifications. The purpose was to verify if P(DMA-co-TlaAm)-30% copolymer and dodecanethiol were indeed grafted. Moreover it allowed verifying if any PAA sacrificial layer was remaining on the surface after dissolution in water.

Principle

For XPS measurements, a sample is introduced in an ultra high vacuum chamber and irradiated with an X-ray beam. Electrons of the atoms present onto the surface interact with these X-rays generating photoelectrons. Photoelectrons will move inside the solid and undergo various scattering processes. A part can reach the surface and shall be emitted in the vacuum if they have enough energy to surmount the work function threshold. These photoelectrons are then collected and analysed by measuring their kinetic energy. This energy (in electron volt, eV) can be measured with a precision of about 0.2 eV for all elements (except H and He) that are present at the surface (probed depth 1-10 nm). Moreover knowing the wavelength of the X-ray and thus their energy allows calculating the binding energy of the ejected core electron[60] :

$$E_b = h\nu - E_{kin}$$

Consequently the chemical state will affect the shape and the position of the recorded peaks (binding energies). Peak areas normalised on the basis of acquisition parameters and corrected with elemental sensitivity factors allow to calculate mole fractions. The detection limit is less than 1 %. A detailed analysis of well-resolved peaks allows the quantification of chemical functions.

Operating parameters

The analyses were performed on a SSX 100/206 photoelectron spectrometer from Surface Science Instruments (USA) equipped with a monochromatised micro focused Al X-ray source (powered at 20 mA and 10 kV). Samples were fixed onto an aluminium conductive carousel with double sided adhesive tape. The pressure in the analysis chamber was around 10^{-6} Pa. The angle between the surface normal and the axis of the analyser lens was 55°. The analysed area was approximately 1.4 mm^2 and the pass energy was set at 150 eV. In these conditions, the full width at half maximum (FWHM) of the Au $4f_{7/2}$ peak of a clean gold standard sample was about 1.6 eV. A flood gun set à 6 eV and a Ni grid placed 3 mm above the sample surface were used for charge stabilisation. The following sequence of spectra was recorded: survey spectrum, C 1s, O 1s, N 1s, Au 4f, K 2p, S 2p and C 1s again to check the stability of charge compensation with time evolution and the absence of sample degradation. The C-(C,H) component of the C1s peak of carbon has been fixed to 284.8 eV to set the binding energy scale. Data treatment was performed with the CasaXPS program (Casa Software Ltd, UK) with a Gaussian/Lorentzian (85/15) product function and after subtraction of a linear baseline. Molar fractions were calculated using peak areas normalised on the basis of acquisition parameters and sensitivity factors provided by the manufacturer.

4.6.3 Ellipsometry

Ellipsometry was used to measure the film thickness on silicon wafers. This technique was notably used to measure the thickness of PAA films deposited by spin-coating and thereafter treated by plasma.

Principle

Ellipsometry is an optical characterisation technique that can be used to measure thin film thickness. The principle is to first elliptically polarise a light beam with the help of a polariser. This light beam is sent on the sample surface and specularly reflected. After that the beam is detected and analysed. The polarisation before the light beam reaches the sample is known thanks to the polariser. Moreover the change in polarisation state after the light beam has reflected from the sample, is registered by the analyser and detector.[61]
As the polarisation changes, two components of the electromagnetic wave change : E_{pi} (the component parallel to the plane of incidence) and E_{si} (the component perpendicular to the plane of incidence). After reflection they become E_{pr} and E_{sr} respectively. This modification can be quantified by the complex amplitude reflection coefficients given by Fresnel equations[61] :

- $r_p = \frac{E_{pr}}{E_{pi}} = \frac{N_s cos\theta_i - n_a cos\theta_t}{N_s cos\theta_i + n_a cos\theta_t}$

- $r_s = \frac{E_{sr}}{E_{si}} = \frac{n_a cos\theta_i - N_s cos\theta_t}{n_a cos\theta_i + N_s cos\theta_t}$

where n_a is the real index of refraction of the ambient, $N_s = n_s\text{-}ik_s$ where n_s is the real index of refraction of the sample and k_s its extinction coefficient, θ_i is the angle of incidence and θ_t is the complex angle of transmission. Snell's law can be used to eliminate θ_t. Ellipsometry measures the reflectance ρ equal to the ratio of those two coefficients.

$$\rho = \frac{r_p}{r_s} = \tan\,\psi\ e^{i\Delta}$$

where $\tan\,\psi$ is the ratio of the modules ($|r_p|/|r_s|$) and Δ is the phase shift introduced by the reflection. The two angles, characteristic of the studied surface, are called ellipsometric angles and characterise the polarisation state change during reflection. As ellipsometry is an indirect method, the measure of ψ and Δ cannot be converted directly into the optical constants and thickness of the sample. A model analysis must be developed that considers the optical constants and thicknesses of all layers of the sample. An iterative procedure is then used in which unknown optical constants and thicknesses are varied while ψ and Δ are calculated. The ψ and Δ values that are the closest to the experimental measures are eventually kept and the corresponding thickness is given by the model[61] .

Operating parameters

Ellipsometric measurements were performed in a clean room environment with a Sentech SE 850 equipment using the SpectraRay software. The apparatus is a spectroscopic ellipsometer that employs broad band light sources (190-900 nm). Ellipsometry is used to measure the thickness of spin-coated PAA layers on silicon substrates. The model to calculate optical constants and thicknesses is thus made out of 3 material layers and the ambient, namely silicon, SiO_2, PAA and air.
The first layer is the silicon substrate. Information regarding the values of n and k,

real and imaginary part of the refractive index respectively, for silicon was provided by the database of the SpectraRay software. These values vary significantly with the wavelength.
The second layer is made of SiO_2. Its thickness was set at 1.5 nm. The evolution of the refractive index with the wavelength is calculated by Cauchy's equation :

$$n(\lambda) = n_0 + \frac{n_1}{\lambda^2}$$

where n_0=1.452, n_1=36 and λ is the wavelength.
The third layer is made of PAA. The evolution of the refractive index with the wavelength is again calculated by Cauchy's equation with n_0=1.474 and n_1=47. The thickness of this layer needs to be set at a certain start value (initial condition), preferentially close to the real value, so that the model can start to iteratively calculate and optimise this thickness.
Lastly the ambient air is added to the model with a refractive index of 1.

4.6.4 Scanning electron microscopy (SEM)

SEM was used to characterise gold nanostructured surfaces before spin-coating in order to define the nanopillar's geometry (height and diameter) and density. It was also used to observe spin-coated surfaces although the image quality was bad.
The used equipment was a JEOL 7600F device. It included a semi-inlens secondary electron detector, a lateral secondary electron detector and backscatted electron detectors (classical and LABE).
In this master thesis only secondary electrons were used to produce images of the samples. The electron beam energy was set at 15 keV.

4.6.5 Atomic force microscopy (AFM)

AFM was used to characterise nanostructured gold surfaces before spin-coating, after spin-coating and after plasma treatment.
The used equipment is a Bruker Multimode Nanoscope V equiped with a tilt compensated high aspect ratio AFM tip provided by Nanosensors (type : AR5T-NCHR-10). This tip is appropriate for nanostructured surfaces like gold nanopillars.

CHAPTER 5

RESULTS AND DISCUSSION

In this chapter, the results obtained during this work are presented. The different functionalised surfaces that were elaborated and analysed are shown in figure 5.1.

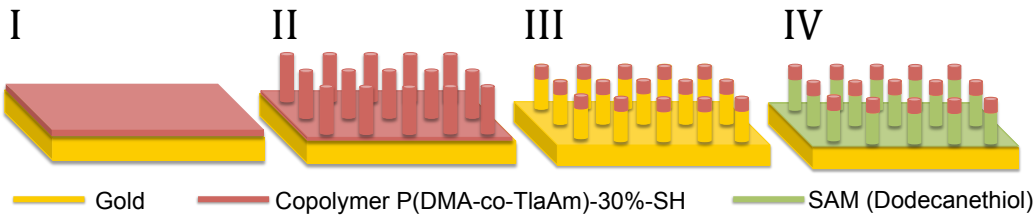

Figure 5.1 – Types of functionalised surfaces fabricated during this project. I) Flat surface (reference). II) Fully functionalised nanostructured surface. III) & IV) Chemically and topographically patterned surfaces; green colour = SAM (dodecanethiol) and red colour = P(DMA-co-TlaAm)-30%-SH.

The results obtained during this master thesis are split in three parts. The first part focuses on step I of the strategy (figure 3.4 in section 3.2), namely, the gold nanopillars fabrication and the preparation of the protected nanostructured surface for the selective functionalisation of the top of the nanopillars. These steps can be considered as the nanofabrication part of the work.

The second part of the results concerns electrochemical results obtained on bare gold surfaces. This part is intended to highlight the differences between flat and nanostructured surfaces during CV measurements.

The last part of the results is related to the chemical gold surface modification. This includes steps II and IV of the strategy (figure 3.4) that are the grafting of P(DMA-co-TlaAm)-30% copolymer and a SAM (dodecanethiol). Moreover the characterisation of the resulting surfaces will be discussed.

5.1 Gold nanopillars fabrication and exposure of their tops for selective functionalisation

5.1.1 Gold nanopillar fabrication

Gold nanopillars were fabricated according to the protocol given in section 4.2. After completion the gold nanopillars are characterised by SEM in order to know precisely their geometry (height and diameter) and their density. The results of this SEM characterisation are displayed in table 5.1 for the surfaces that will be analysed in this chapter. In addition, figures 5.2 and 5.3 are representative SEM images of surfaces A and B respectively.

	Diameter [nm]	Height [nm]	Density [10^9 pillars/cm^2]
Surface A	84 ± 9	515 ± 85	1.20 ± 0.17
Surface B	79 ± 3	454 ± 108	1.09 ± 0.08

Table 5.1 – Characteristics of used nanostructured surfaces.

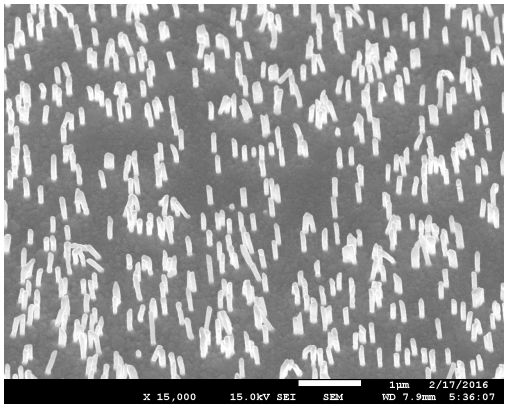

Figure 5.2 – SEM image of surface A (with a tilt of 30°).

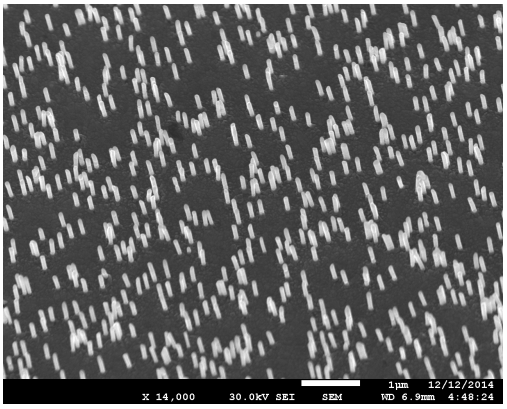

Figure 5.3 – SEM image of surface B (with a tilt of 30°).

5.1.2 PAA spin-coating

Spin-coating was performed to deposit a thin layer of PAA onto nanostructured gold surfaces. This technique was chosen because it is simple, fast and believed to be able to deposit a homogenous layer onto nanostructured surfaces as proven by literature.[62,63] Moreover PAA was selected because it is a water-soluble material so easy to spin-coat from an aqueous solution and easy to remove with water. Finally, PAA is not soluble in chloroform, which is the solvent used to graft P(DMA-co-TlaAm)-30% copolymer. It is thus suitable as a protecting layer during copolymer grafting on the top of the nanopillars.

The results obtained with spin-coating are given in the following sections. First outcomes were obtained by spin-coating on silicon substrates in order to calibrate the operating parameters. After calibration, spin-coating was performed on flat and nanostructured gold surfaces. The characterisation techniques used on gold surfaces are SEM and AFM whereas ellipsometry was used on silicon wafers.

Calibration of spin-coating parameters

First of all, spin-coating calibration was performed to estimate the obtained film thickness as a function of spin-coating parameters. Indeed, it is important to know precisely the obtained film thickness to expose the top of the nanopillars only. Ellipsometry is used to measure the film thickness but this technique is not compatible with gold surfaces. Therefore calibration was performed on silicon wafers. The spin-coating parameters to be defined are :

1. PAA solution concentration ($\frac{g}{ml}$)
2. Volume of PAA solution deposited (μl)
3. Speed (rpm)
4. Acceleration (rpm/s)
5. Time (s)

In this master thesis, some parameters were fixed by taking into account data extracted from the literature about PAA spin-coating.[43,64,65] Accordingly, the time was always set at 60 s in all spin-coating experiments and the acceleration equalled half of the speed. Furthermore the volume of PAA solution deposited was 40 μl. This value is low but was encountered in the literature.[63]

The remaining parameters, namely speed and PAA concentration, were varied and the resulting film thickness was measured by ellipsometry. The speeds investigated were : 1750, 2000, 2500, 3000 rpm whereas the investigated PAA concentrations were 0.025, 0.05, 0.065, 0.075 and 0.1 g/ml. It was however rapidly realised that the only speed compatible with our gold nanopillars was 1750 rpm because higher speeds induce damages on the nanopillars. Therefore focus was given to this speed although the obtained film thickness for other speeds was also investigated (see chapter B section B.1). Calibration results are represented in figure 5.4 and numerical values given in table 5.2.

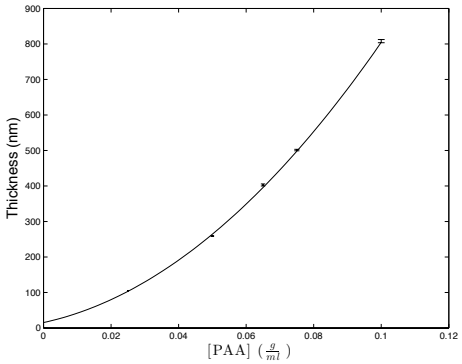

Figure 5.4 – Final calibration curve, experimental values are marked by error bars and the curve results from interpolation.

[PAA] (g/ml)	Thickness [nm]
0.025	105 ± 1
0.05	258 ± 2
0.065	400 ± 5
0.075	499 ± 5
0.1	803 ± 9

Table 5.2 – Film thickness obtained for various PAA concentrations.

To summarise, the only parameter truly varied in spin-coating was the solution concentration. The more the solution was concentrated, the thicker the resulting PAA film became. The other spin-coating parameters fixed at a specific value are given below.

1. Volume of PAA solution deposited : 40 μl

2. Speed : 1750 rpm
3. Acceleration : 875 rpm/s
4. Time : 60 s

Adhesion test on gold

Before starting to spin-coat on nanostructured gold surfaces, the proper adhesion of PAA on gold had to be verified. This was done by spin-coating a ca. 1 μm thick PAA film on a flat gold surface and controlling by naked eye if any film was present. Indeed, a spin-coated layer onto a gold surface is visible by naked eye and if the PAA film does not adhere to the gold surface no layer will be deposited nor visible. This adhesion test was successful. Moreover the spin-coated flat gold surface was immerged in chloroform for 1 h to ensure that no film detachment could occur during copolymer grafting. This test was also successful.

Spin-coating on nanostructured gold surfaces

After spin-coating calibration was performed and PAA adhesion on gold surfaces was verified, spin-coating of a PAA layer on gold nanostructured surfaces was tested.

First experiments at speeds higher than 1750 rpm failed. Indeed, the pillars had almost all fallen down. Those results are shown in appendix B section B.2. Other spin-coating experiments were performed on surfaces A and B at lower speed, namely 1750 rpm. Table 5.3 shows for each surface the most important parameters regarding spin-coating. It was chosen to spin-coat PAA films with a thickness close to the height of the nanopillars so that only the top of the nanopillars could be exposed.

	PAA concentration [g/ml]	PAA film thickness [nm]	Height nanopillars [nm]
Surface A	0.075	~ 500	515 ± 85
Surface B	0.065	~ 400	454 ± 108

Table 5.3 – Nanostructured surfaces main characteristics : nanopillar height and spin-coating parameters. The PAA film thickness is estimated according to the calibration curve (figure 5.4).

Results. To evaluate if the spin-coating experiments were concluding, SEM ad AFM images were taken. First of all, figure 5.5 shows a SEM image of surface A after spin-coating. It can be observed that a layer of material (most likely PAA) is present around the nanopillars (easy to identify because of their shape and the fact that they emit more electrons and are thus 'whiter'). No sharp image could be taken of the layer surrounding the nanopillars as it emits a low amount of electrons and is electrically charged. This material is thus not a conductor. A better image could have been obtained if the sample was coated by a conducting material. Nevertheless the sample could not have been reused any more and because the low number of available samples it was rather chosen to analyse samples after spin-coating by AFM.

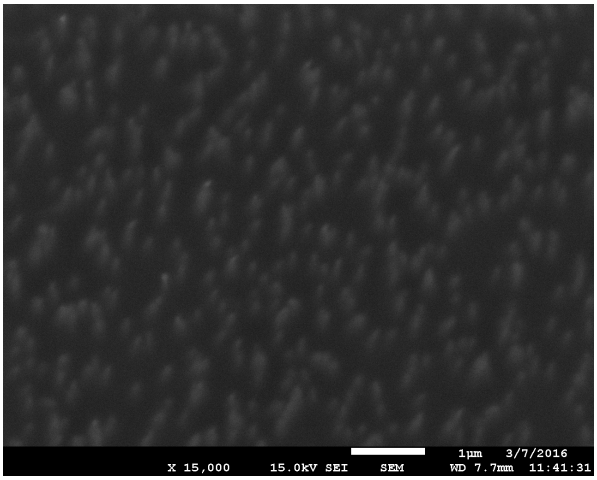

Figure 5.5 – SEM image of surface A after deposition of a PAA thick layer by spin-coating (with a tilt of 30°).

Further figures 5.6 and 5.7 show SEM images before spin-coating and after PAA film dissolution so as to compare the state of the pillars before and after spin-coating treatment. The pillars are not damaged in the sense of being broken or layered on the surface. However, these images show that some nanopillars are slightly inclined after spin-coating.

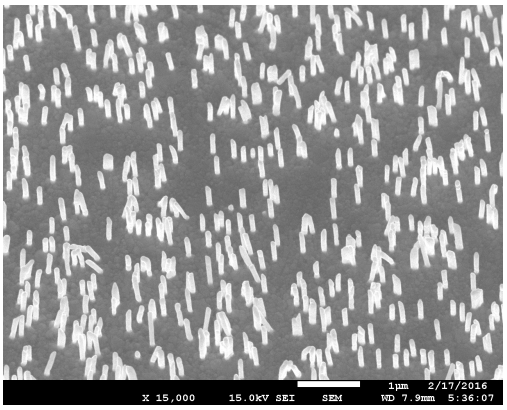

Figure 5.6 – SEM image of surface A before spin-coating (with a tilt of 30°).

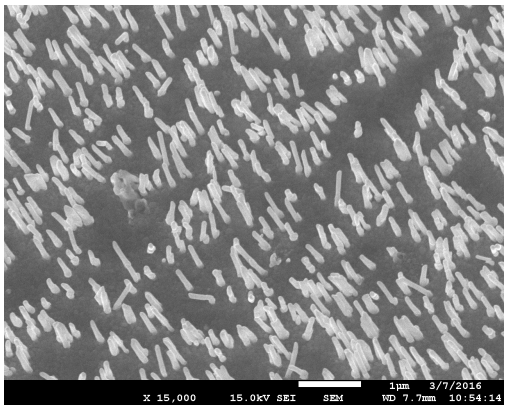

Figure 5.7 – SEM image of surface A after PAA film dissolution (with a tilt of 30°).

AFM images were also taken before and after spin-coating. These are shown in figures 5.8-5.10. By comparing figures 5.8 and 5.9, it can be seen that surface A is almost completely covered by PAA. Indeed, the pillars are 515 nm high and with a PAA layer of 500 nm they should only pop out by 15 nm. Consequently the pillars are almost impossible to distinguish. Surface B, meanwhile, is less covered and pillars are still easy to recognise in topographical contrast. This is because surface B has pillars of 454 nm high and a PAA layer of 400 nm. Hence pillars should theoretically pop out by 54 nm, which is relatively more than on surface A.

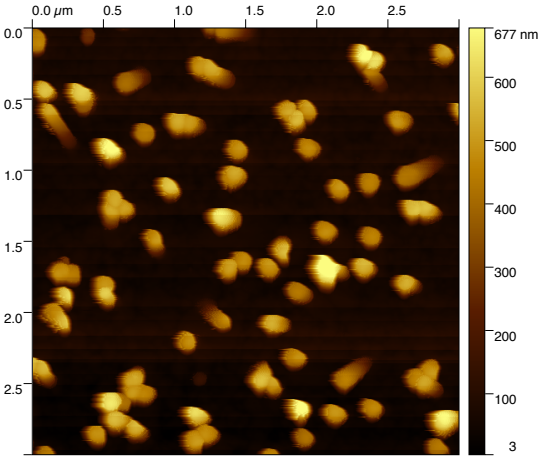

Figure 5.8 – AFM topographical image of surface A before spin-coating in topographical contrast.

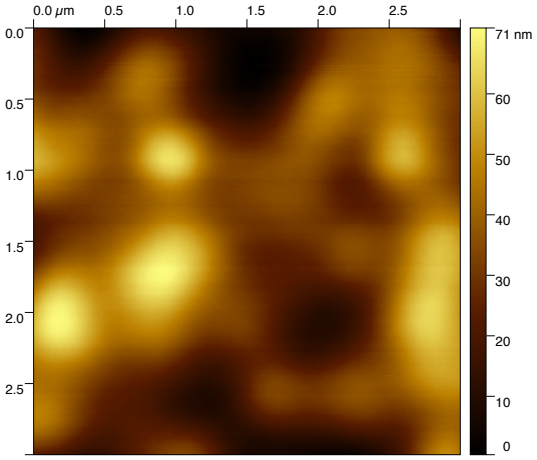

Figure 5.9 – AFM topographical image of surface A after spin-coating in topographical contrast.

Moreover AFM allowed to measure nanopillars height profiles as illustrated in figure 5.11 where the profiles of a nanopillar are shown before and after spin-coating. Attention should be paid to the fact that those profiles were not all taken on the same nanopillar, on the same surface. They are represented together for a rather qualitative comparison and allow to see how the film is deposited around the nanopillar. In addition, the height profile obtained after spin-coating for surface A (blue curve in figure 5.11) is rather uncertain as the nanopillars are difficult to distinguish for this surface after spin-coating (figure 5.9).

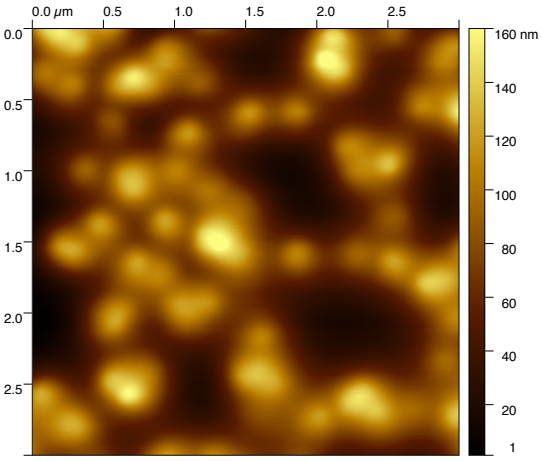

Figure 5.10 – AFM topographical image of surface B after spin-coating.

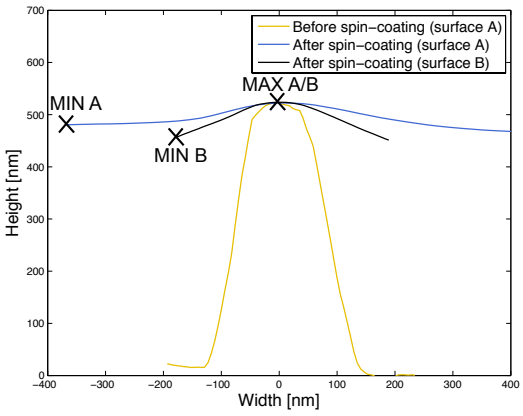

Figure 5.11 – Height profiles of a gold nanopillar. The maximum and minimum values of height profiles after spin-coating are cross-marked.

Quantitative results regarding the height difference between the top of the nanopillars and the PAA film were obtained by calculating the difference between the maximum and minimum values of 40 to 80 different nanopillar height profiles after spin-coating (see figure 5.11 where maximum and minimum values are cross-marked). The results are represented as histograms in figures 5.12 and 5.13. Moreover, mean values of this statistical analysis are presented in table 5.4 together with the surfaces main characteristics.

Those results show that the experimentally observed distance between the PAA film and the top of the nanopillars does not perfectly coincide with the expected theoretical value. Moreover, it appears that the histograms do not show a normal distribution.

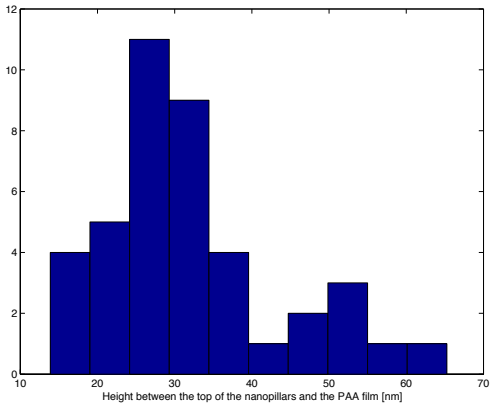

Figure 5.12 – Histogram of the experimentally measured (by AFM) height between the top of 41 gold nanopillars and the PAA film for surface A.

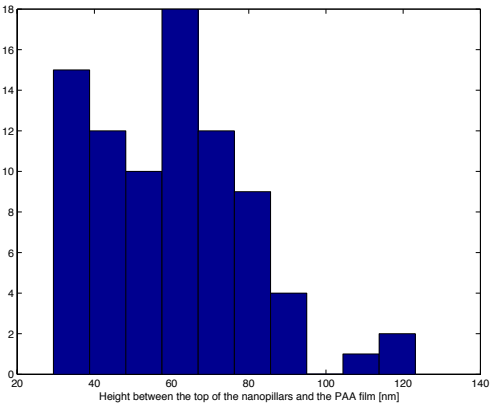

Figure 5.13 – Histogram of the experimentally measured (by AFM) height between the top of 83 gold nanopillars and the PAA film for surface B.

	PAA film thickness [nm]	Height nanopillars [nm]	Theoretical distance PAA film - top of nanopillars [nm]	Experimental distance PAA film - top of nanopillars [nm]
Surface A	∼500	515 ± 85	15	32
Surface B	∼400	454 ± 108	54	60

Table 5.4 – Nanostructured surfaces main characteristics with experimental and theoretical values of height differences between the PAA film and the nanopillars as measured on AFM height profiles. Number of height profiles measured for surface A and B are 41 and 83, respectively.

Discussion. Spin-coating experiments allowed to successfully spin-coat nanostructured surfaces without damaging them considerably.
During the first tests, experiments failed as the nanopillars were almost all broken. It was then decided to address this problem by

1. Decreasing the spin-coating speed from 2000 to 1750 rpm to reduce the force exerted on the nanopillars. When the spin-coater starts to spin, the nanostructured surface and the PAA on it, yet liquid at that moment, also start to spin quickly reaching the maximum speed. Simultaneously a centrifugal force is exerted on the nanopillars and on the PAA solution. This force pushes away from the center in a radial direction. The nanopillars are thus submitted to this force, which could bend or break them. In addition, during spin-coating, PAA solution is ejected (figure 2.8 in section 2.3.1 chapter 2) due to the radial centrifugal force. Thus PAA solution flows to the border of the surface to be ejected. Nevertheless, the nanopillars create a considerable obstacle to the PAA motion. As the PAA solution flows around the nanopillars to reach the border of the surface, it exerts a force on the nanopillars, which could also bend or break them. In summary the nanopillars are submitted to a centrifugal force due the rotation movement during spin-coating but also to a

force exerted by the PAA solution when it moves to the borders of the surface to be ejected. If the total force exerted on the nanopillars is too strong (exceeding the force associated with ultimate stress) the nanopillars will break or be deformed. It is thus important to limit the forces exerted on the nanopillars. Therefore the centrifugal force should be limited because this force is exerted directly on the nanopillars but it is also responsible for the radial motion of the PAA. Reducing the rotation speed reduces the centrifugal force. In this master thesis it was thus decided to set the speed at the minimum value of 1750 rpm (lower speed values do not allow to obtain a thin homogenous film).

2. Reducing the nanopillar height to maximum 550 nm to reduce the stress. Indeed, a nanopillar on a planar surface can be envisioned as a cantilever beam. The centrifugal force exerted by the spin-coat solution during spin-coating can be modelled as a uniform load. If assumed that only elastic bending occurs, that the loading is uniform across the beam (torsion and other loadings are neglected) and that nanopillars have a circular cross section, beam theory states that maximum stress equals[66] :

$$\sigma = \frac{F\,h^2}{1.56\,r^3}$$

where F is the centrifugal force, r the nanopillar radius and h the nanopillar height. It can be deducted from this formula that the nanopillar geometry greatly affects the maximum stress and thus nanopillars resistance to bending and rupture. Indeed, once the elastic maximum stress reaches a threshold, plastic bending (irreversible) starts and could eventually lead to rupture. If the height of the nanopillars decreases, maximum stress also decreases. Whereas if the diameter decreases, the opposite effect is observed. Nanopillars are therfore more resistant to bending if they are thicker and/or shorter. In this master thesis it was decided to work with shorter nanopillars not exceeding 550 nm in height.

The above two adjustments were effective as further spin-coating experiments did not break the nanopillars. However, as shown in figure 5.7, permanent bending of nanopillars was sometimes observed. Results could be further improved by increasing the diameter of the nanopillars or by decreasing the height of the nanopillars. Further decreasing the spin-coating speed is not an option, as it would not deliver a homogenous thin film. Potentially spin-coating acceleration could be decreased.

Next, figures 5.5, 5.9 and 5.10 indicate that spin-coating effectively deposited a homogenous layer of PAA. Moreover for surface A the spin-coated film almost completely covered the nanopillars. Indeed, figure 5.5 shows that the nanopillars are well surrounded by the polymeric film resulting in charging and bad SEM image quality. In case of surface B the nanopillars are still surrounded by PAA but less covered than on surface A (figure 5.10).
This was furthermore confirmed by AFM profile measurements as shown in figure 5.11. These measurements allowed to compare experimental and theoretical values for the distance between the PAA film and the top of the nanopillars (table 5.4). For surface A experimental results were not as close to theoretical results as for surface B. This can be explained by the fact that the error margin on the nanopillar height (85 nm) is high and nanopillars having a height of 500 nm or less cannot be made visible and are thus not taken into account. This feature may increase the experimental measured distance between the PAA film and the top of the nanopillars. Moreover tip effects could also

influence the obtained AFM results. Furthermore, histograms in figures 5.12 and 5.13 do not show a normal distribution. This could indicate a certain inhomogeneity across the surface. This inhomogeneity can be due to inhomogeneity in the nanopillar density or height across the surface or to inhomogenous PAA film deposition. Nevertheless experimental measurements for surface B are very close to the predicted ones (60 nm compared to 54 nm). Although it cannot be assumed with certainty that theoretical spin-coated thickness perfectly matches the experimentally observed values, it seems that experimental values are rather close to the theoretical ones.
To conclude, SEM and AFM images proved that :

1. Nanopillars can be spin-coated without significant damage
2. The theoretical film thickness is close to the experimental film thickness

5.1.3 Plasma treatment

Plasma treatment was performed after spin-coating for two reasons. First, etching of PAA film by oxygen plasma allows to reveal the tops of the nanopillars in order to functionalise them selectively (see figure 3.4 step I in chapter 3). Secondly, by applying the plasma treatment, not only the PAA film will be etched but also the exposed gold surface should be clean enough to graft the P(DMA-co-TlaAm)-30% copolymer during the next step of the process.

Plasma results are presented and discussed in this section. To begin, the calibration of the plasma treatment was performed. Then, the plasma treatment was applied to spin-coated gold nanostructured surfaces.

Calibration of plasma treatment

Plasma calibration was performed to estimate the thickness of etched PAA film in function of the power, P (in W) and the duration of the treatment (in s) of the plasma treatment. Therefore a 4-step process was used :

1. Spin-coating of silicon substrates with PAA solution (0.075 g/ml)
2. Thickness measurement of the spin-coated PAA film by ellipsometry
3. Plasma treatment at various times and powers
4. Thickness measurement after etching of the PAA layer by ellipsometry to estimate the etched thickness

It was chosen to investigate two powers (50 and 100 W) and 6 plasma durations (30, 60, 90, 120, 150 and 180 s). The results are shown in figure 5.14. From this graph, we can conclude that plasma treatment for less than 60 s is inefficient; indeed no PAA etching occurs. Furthermore plasma treatments lasting longer than 120 s cannot be considered since they will result in too much film damage. Indeed, optical microscope images showed that the film was severely damaged with the presence of holes when longer plasma treatments are performed. Furthermore as the maximal power is 100 W, the maximum PAA layer etching is 50 nm. Eventually it was decided to only use a plasma treatment of 100 W during 120 s.

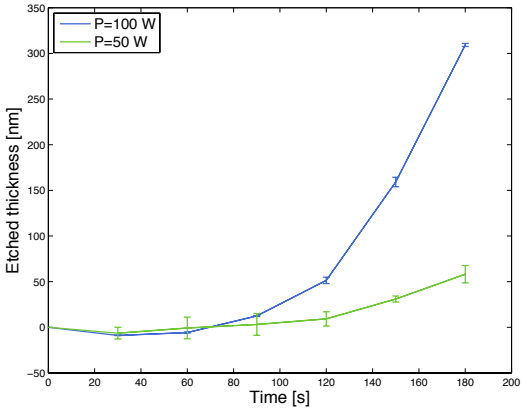

Figure 5.14 – Calibration curves of plasma treatment.

Plasma treatment on spin-coated nanostructured surfaces

After calibration, plasma treatment was performed on spin-coated gold nanostructured surfaces. To control if the plasma had been efficient, SEM and AFM images were taken. Moreover AFM height profiles were again extracted.

Results. First of all, SEM images were recorded to confirm that the tops of the nanopillars were exposed with a plasma treatment of 100 W for 120 s.

Results for surface B are shown in figures 5.15 and 5.16. These images suggest that the tops of the nanopillars are uncovered because they become visible on SEM images with a good precision which was not the case before plasma treatment (figure 5.5). However the images also show that the nanopillars are bended and their extremities tend to stick together as illustrated in figure 5.16. Moreover at higher magnification, it is possible to detect a partial tearing of the PAA film. Indeed, some holes (indicated by red arrows in figure 5.16) are clearly visible. These defects become more visible by increasing the brightness and contrast of the image as shown in appendix B section B.3.

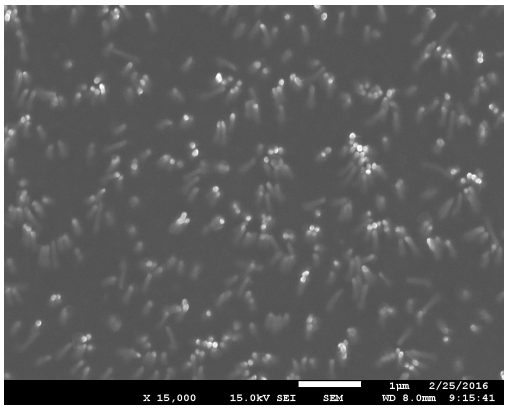

Figure 5.15 – SEM image of spin-coated surface B after plasma treatment.

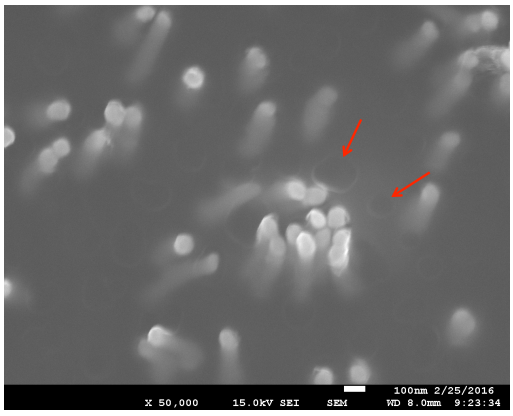

Figure 5.16 – SEM zoom-in image of spin-coated surface B after plasma treatment. Red arrows indicate visible holes in the PAA film.

Unfortunately no sharp SEM image could be taken from surface A. It seems that the nanopillars were not sufficiently uncovered to be analysed by SEM. Further characterisation was thus performed by AFM.

AFM images for surface A are presented in figures 5.17 and 5.18. It can easily be seen that the surfaces have drastically changed if one compares with figure 5.9. The nanopillars can easily be distinguished in phase contrast images proving again that etching was successfully performed. Moreover the topographical image also shows traces of the plasma treatment. Indeed, circular features can be seen all over the surface and those circles are not only nanopillars. Obviously some of them result from the plasma treatment damaging the film by making holes. This was already seen in SEM images (figure 5.16). Moreover, as already said, if the plasma treatment is applied for longer than 120 s, this damage also becomes visible with optical microscopy resulting in a very inhomogenous film.

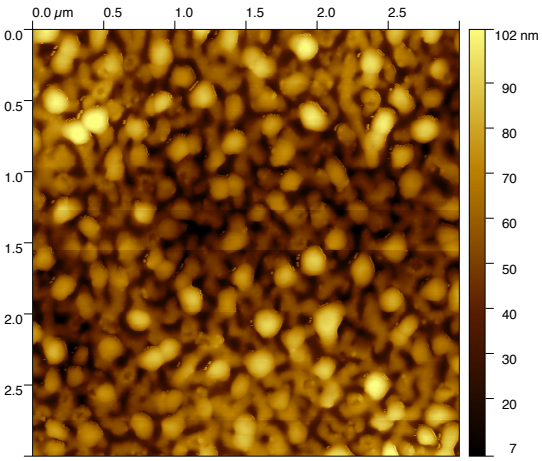

Figure 5.17 – AFM topographical image of spin-coated surface A after plasma treatment.

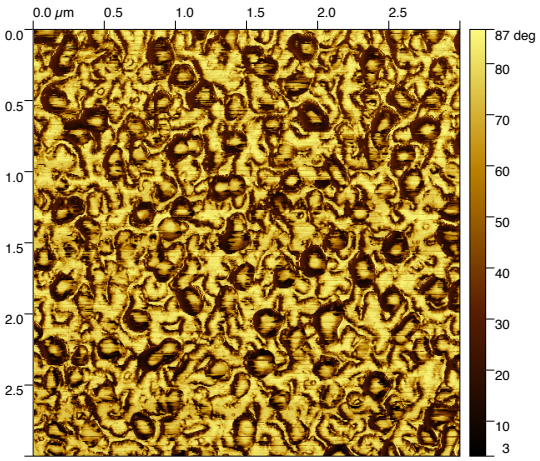

Figure 5.18 – AFM phase image of spin-coated surface A after plasma treatment.

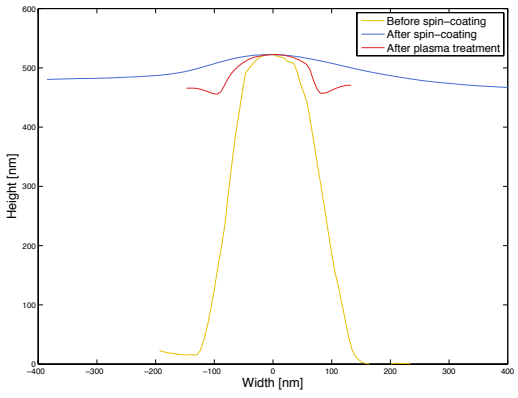

Figure 5.19 – Height profile of a nanopillar from surface A before and after PAA spin-coating and after plasma treatment (100 W).

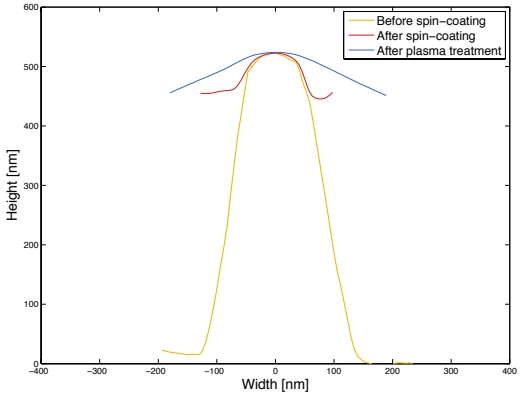

Figure 5.20 – Height profile of a nanopillar from surface B before and after PAA spin-coating and after plasma treatment (100 W). The height profile of the gold nanopillar stems from surface A as a reference.

AFM images allow to extract height profiles. This was done on AFM images before and after plasma treatment resulting in figures 5.19 and 5.20.
For surface A one can see that plasma treatment seems to have worked. The tops of the nanopillars become visible as evidenced by the analysis of AFM profiles. However it can also be seen that the height profile after plasma treatment (red curve in figure 5.19) does not perfectly coincide with the height profile of a bare gold nanopillar (yellow curve in figure 5.19).
For surface B results are clearer. For some nanopillars the height profile after plasma treatment (red curve in figure 5.20) perfectly coincides with a bare gold nanopillar (yellow curve in figure 5.20). Nevertheless not all height profiles of the surface after plasma treatment coincide that well.

Furthermore the theoretical and experimental distance (measured on AFM height profiles) between the PAA film and the tops of the nanopillars were compared. The results are represented as histograms in figures 5.21 and 5.22. Mean values are also given in table 5.5 together with the theoretically expected values. These show that plasma etching was perfectly predicted for surface A but not for surface B. In addition, the histograms do not show a normal distribution.

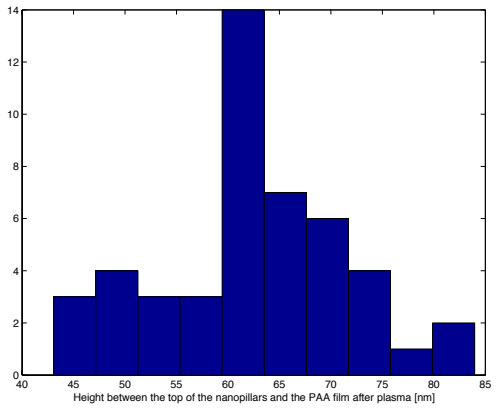

Figure 5.21 – Histogram of the experimentally measured (by AFM) height between the top of 80 gold nanopillars and the PAA film after plasma treatment for surface A.

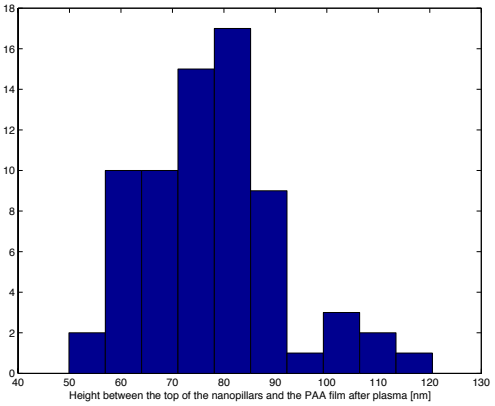

Figure 5.22 – Histogram of the experimentally measured (by AFM) height between the top of 78 gold nanopillars and the PAA film after plasma treatment for surface B.

	Theoretical distance PAA film - top of nanopillars after plasma treatment [nm]	Experimental distance PAA film - top of nanopillars after plasma treatment [nm]
Surface A	ca. 65	62
Surface B	ca. 104	78

Table 5.5 – Comparison of the theoretically predicted and experimentally measured distance between the PAA film and the tops of the nanopillars. Theoretical values are given by the calibration of the spin-coating and plasma treatment on silicon wafers. Experimental values are extracted from AFM height profiles. The number of profiles measured for surface A and B are 80 and 78 respectively.

Discussion. To begin, SEM images (figure 5.15 and 5.16) of surface B show that the tops of the gold nanopillars are revealed after plasma treatment. They also show the

bending of the nanopillars, which is consistent with SEM images after PAA film dissolution (figure 5.7). This bending is probably due to strong forces applied on nanopillars during spin-coating as already explained in the previous section. However this bending could compromise the exposure of the top of the nanopillars. Indeed, bending will affect the effective height of nanopillars as illustrated in figure 5.23. Consequently the nanopillars could be less uncovered as theoretically predicted.
Next, for surface A, no sharp SEM images could be made after plasma treatment suggesting that the tops of the nanopillars may not be properly uncovered. Another explanation is that for surface A the nanopillars should only pop out of about 65 nm whereas for surface B we should have 104 nm. Only a very small part of the gold nanopillars is thus visible on surface A compared to surface B where almost twice as much height of nanopillar is uncovered (104 nm compared to 65 nm). Consequently the high amount of remaining non-conductive PAA around the small uncovered nanopillar tops (65 nm) on surface A could hamper SEM imaging because the charging of non-conductive materials give rise to bad SEM image quality.

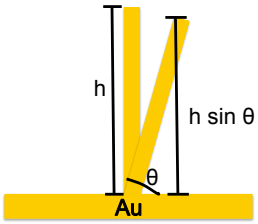

Figure 5.23 – Bending affecting the effective height of the nanopillars.

After that, AFM images show that the film topography has significantly changed. The results are consistent with the plasma treatment as nanopillars are exposed and appear clearly on AFM phase images. Furthermore it can be seen that surfaces are quite inhomogeneous after plasma treatment. Indeed, the topographical images show that the surface is not flat between the nanopillars whereas it was relatively flat after spin-coating (figure 5.9 and 5.10). This is consistent with the PAA film defects (i.e. holes) observed in a high magnification SEM image (figure 5.16) but could also be explained by tip effects distorting topographical images. Plasma treatment seems to result in an increase of roughness but this cannot be assumed with certainty as the presence of nanopillars affect surface imaging roughness. If desired this could be further investigated by applying plasma treatment on flat spin-coated surfaces and compare AFM images and surface roughness measurements before and after plasma treatment. However in case of nanostructured surfaces it can be concluded that the PAA film seems less homogenous between nanopillars after plasma treatment.

Furthermore the obtained height profiles before and after 100 W plasma treatment give evidence of etching (figures 5.19 and 5.20). In both cases the height profiles after plasma treatment become closer and even coincide with the topographical profiles of the tops of nanopillars measured for a bare gold nanopillar. This allows to conclude without doubt that plasma treatment was effective. However, whereas for surface B height profiles coincide well with a bare gold nanopillar it is not the case for surface A. Either the nanopillars of surface A are not well uncovered, this was already suggested by the fact that no sharp SEM images could be taken, or tip effects broadened the height profile. As we know that the surface is quite inhomogenous after plasma treatment with a most likely increase in surface roughness, tip artifacts could appear. Tip artifacts may occur if the surface features have the same or a smaller size than the AFM tip. If so, the tip cannot correctly draw the profile contours giving rise to convolution effects

especially feature broadening. Although tip effects may explain some broadening of the height profiles of surface A, it is not clear why such tip effects occurred only during measurements on surface A and not on surface B. We can however conclude that the tops of the nanopillars from surface B are well uncovered according to the measured AFM height profiles but we cannot draw the same conclusion for surface A as results are quite uncertain about this question.

Then, the histograms in figures 5.21 and 5.22 do not show a normal distribution. Moreover, the experimentally calculated distance between PAA film and tops of the nanopillars based on AFM height profiles is not completely consistent with the expected theoretical values. For example, for surface B it is expected to obtain 104 nm by applying a plasma treatment at 100 W for 120 s. But AFM images give a value of 77 nm. For surface A results are more consistent with expectations. It is not well understood why such a difference exists between both surfaces. Either the measurements are distorted due to the following reasons.

- It could be due to the fact that AFM is a very local characterisation technique and although images and measurements were performed on different areas of the surface, there might not be enough to have a correct statistical analysis.
- Some tip effects may also result in a broadening of height profiles as explained previously. Moreover tip effects can result in a vertical error if the tip is too large compared to the depth of a surface feature. As the surface is very inhomogenous and rather rough, it is difficult to estimate tip effects. AFM measurements on rough surfaces are less reliable and more difficult to interpret due to these tip effects.

Or the measurements are correct but the plasma treatment was less efficient than expected. This could be due to the fact that for surface B the pillars are more popping out of the PAA film compared to surface A after spin-coating resulting in a considerable surface roughness. This could affect the plasma treatment efficiency and homogeneity. Moreover if one compares the results after plasma treatment (table 5.5) with the results after spin-coating (table 5.4) it can easily be seen that plasma treatment is not as effective as it should be. This could be due to the fact that PAA could also deposit on the top of the nanopillars in which case the height difference between the PAA film and the top of the nanopillars does not increase immediately during plasma treatment (figure 5.24).

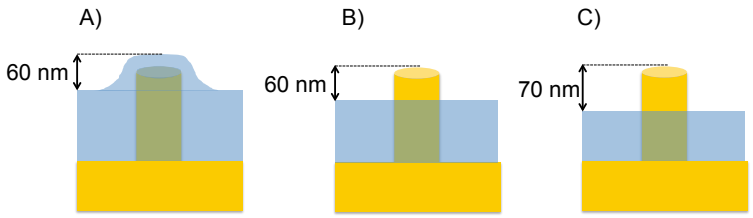

Figure 5.24 – The surface morphology of the PAA film deposited on nanopillars can affect the final height of the exposed nanopillars obtained after plasma treatment. A) Before plasma treatment. B) During plasma treatment, when the tops of the pillars become exposed. C) After plasma treatment. Values are randomly chosen and not representative.

Another possible explanation for these inconsistent results is the fact that the plasma treatment is isotropic[a]. This means that the incident plasma or more precisely ions are

[a]This information is provided in the technical specifications of the used plasma etcher i.e. K1050X

randomly oriented with respect to the sample to be treated. If the plasma is isotropic, its efficiency varies strongly with surface roughness or the presence of nanostructures. This is illustrated in figure 5.25.

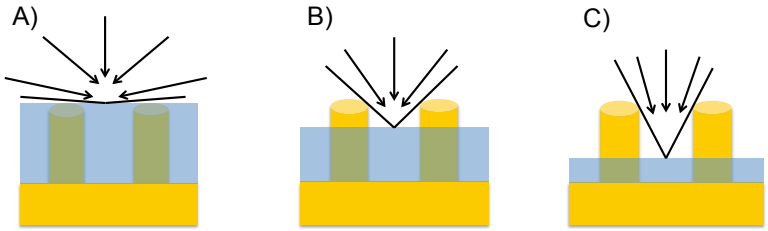

Figure 5.25 – Isotropic plasma treatment efficiency regarding incident angle. A) Flat surface or nanostructured surface fully covered by a PAA film. B) Nanostructured surface with slightly uncovered nanopillars. C) Nanostructured surface with largely uncovered nanopillars.

For flat surfaces or nanostructured surfaces completely covered by a PAA film the isotropic plasma is as efficient as an anisotropic plasma with a beam parallely oriented to the surface normal. This is because every region of the sample has the same probability to be targeted by an ion. As shown in figure 5.25 A, the incident angle can vary from ca. 0 to 90 °C with respect to the surface normal.
On the other hand if the tops of the nanopillars are exposed like in figure 5.25 B, the incident angle to etch the PAA film between two nanopillars is limited. Consequently the probability to etch the PAA film between nanopillars decreases. This effect is even more pronounced when the distance between the tops of the nanopillars and the PAA film increases (figure 5.25 C).

This isotropic character of the plasma treatment could thus explain why it is less efficient on nanostructured gold surfaces compared to flat surfaces. Moreover it could also explain why the plasma treatment is more efficient on surface A than surface B. Indeed, the nanopillars of surface A are less exposed than the ones of surface B (compare figure 5.25 B and C). Thus plasma treatment after spin-coating should be more efficient on surface A, which is experimentally observed. However this effect cannot be predicted with precision. Therefore it seems more appropriate to employ an anisotropic plasma treatment if one needs to know precisely how effective the plasma treatment actually was.

In conclusion plasma treatment on gold nanostructured surfaces should be further investigated if it is desired to know precisely the height of nanopillars revealed after treatment. It is also advisable to employ an anisotropic plasma treatment to get a higher accuracy. However according to results obtained for surface B, we know that by spin-coating a film that is at least 50 nm below the nanopillar's height and subsequently applying a plasma treatment of 100 W during 120 s, the tops of the nanopillars are exposed.

5.2 Bare gold surfaces

In this section, results obtained on bare gold surfaces are presented and discussed in order to understand clearly the initial situation before any surface modification (figure 5.26). Moreover, it allows a better understanding of the differences between flat and

RF Plasma Etcher/Asher/Cleaner.

nanostructured surfaces regarding electrochemical measurements.

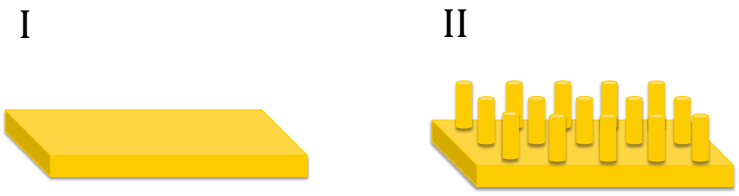

Figure 5.26 – Illustration of both types of bare gold surfaces before surface modification. Bare I) flat II) nanostructured gold surface.

Results. Flat and nanostructured surfaces were analysed by CV, a characterisation technique detailed in section 4.6.1 in order to assess the influence of the presence of nanopillars on these measurements. Results obtained on both surfaces are displayed in figure 5.27.

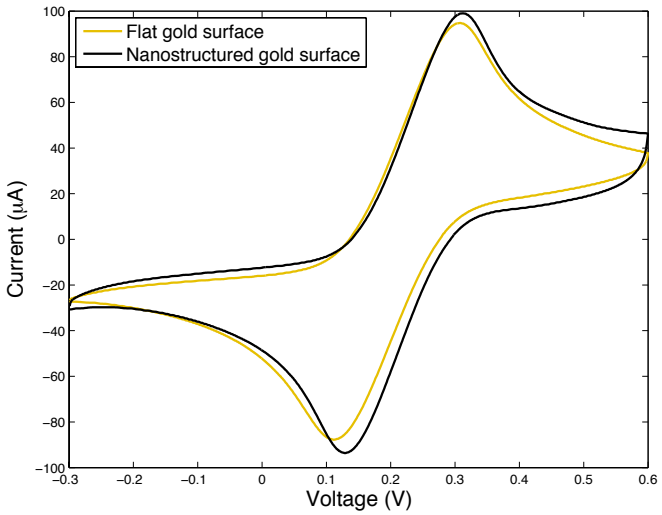

Figure 5.27 – CV measurement of a flat and a nanostructured bare gold surface. The nanostructured surface has a nanopillar height of 723 nm.

In both cases (nanostructured and flat surface), figure 5.27 shows the diffusion-limited process with very similar curve shapes. However the CV curve areas seem different. This was confirmed by matlab calculations of the CV area increase of nanostructured surfaces compared to flat surfaces. The surface increase factor is thus given by the formula :

$$\text{CV Surface increase factor} = \frac{CV\ area\ nanostructured\ surface}{CV\ area\ flat\ surface}$$

This value was calculated for three different nanostructured surfaces all having a nanopillar density of circa 10^9 nanopillars/cm^2. The results are given in table 5.6. It can be seen that the CV surface increase factor raises with the nanopillar height.

Moreover, the geometrical surface increase factor was calculated according to the following formula :

$$S_p = \pi.\Phi_p.h_p.d$$

where S_p is the surface increase created by nanopillar per plane electrode surface unit ($cm^2_{nanopillar}/cm^2_{electrode}$), Φ_p is the nanopillar diameter (90 nm), h_p is the nanopillar height and d is the nanopillar density (10^9 nanopillars/cm^2). The calculated S_p values for different nanopillar heights are displayed in table 5.6.

Nanopillar height [nm]	Measured CV area	CV surface increase factor	S_p [$cm^2_{nanopillar}/cm^2_{electrode}$]
0 (flat)	3.678 ± 0.098	-	-
450	4.098	1.114	1.27
510	4.302	1.170	1.44
723	4.314	1.173	2.04

Table 5.6 – CV surface increase factor and geometrical surface increase factor, S_p, for flat and nanostructured surfaces with different nanopillar height.

Discussion. Results show a CV area increase for nanostructured surfaces compared to flat surfaces. This increase is low but can be considered as rather significant because the difference in CV area between flat and nanostructured surfaces is higher than the error on the CV area measurements on flat surfaces. Nevertheless the errors on CV area measurements on nanostructured surfaces is unknown and could potentially be high enough to make the difference between flat and nanostructured surfaces non-significant. In case the difference in CV area between flat and nanostructured surfaces is considered as significant, this increase is due to a current increase. Indeed, on figure 5.27 the position of the peaks are the same and the area increase is rather vertical than horizontal. This increase in measured current is probably due to higher exposed surface in the case of nanopillars. Indeed, as more surface is available for redox reactions, more redox species can react and the generated current increases. Furthermore this effect could potentially increase with the nanopillars height because the higher the nanopillars the more available gold surface. However, the differences in CV area of nanostructured surfaces with different nanopillars heights are very low and not significant enough to draw conclusions.

Moreover, the CV surface increase factor is not a direct function of the geometrical surface increase factor as shown in table 5.6. The fact that the CV surface increase factor does not match with the geometrical surface increase can be due to diffusion. Indeed, CV curves for bare gold surfaces are diffusion-limited. Although more surface is available for redox reactions, the diffusion is still considerably limiting mass transport. Consequently the extra available surface cannot be used, as reactive species are not diffusing fast enough. This could also explain why the measured CV area (table 5.6) seems to reach a maximal value as the difference between nanopillars of 510 nm and 723 nm is very small. This would mean that there is a maximal value of effectively used surface area.

Nevertheless another explanation to the high difference between S_p and the measured CV surface increase factors (table 5.6) could lie in the nanopillar density. Indeed, the nanopillar density highly affects S_p and this density can significantly vary from one surface to another as further showed in table 5.7. In addition, the differences in CV surface increase factors for nanostructured surfaces with different nanopillar heights are very small. This suggests that the results could be non-significant. To further investigate this, more measurements should be performed on different nanostructured surfaces to calculate the error on the CV measurements.

5.3 Gold surface modification

In this section results regarding gold surface modification are presented. All the surfaces that were elaborated and characterised are presented in figure 5.28. First, results obtained for P(DMA-co-TlaAm)-30% copolymer grafting are discussed (figure 5.28 I). This includes grafting on a flat gold surface (reference displayed in figure 5.28 I.1), complete functionalisation of a nanostructured gold surface (figure 5.28 I.2) and selective functionalisation of the tops of the nanopillars (figure 5.28 I.3). After that, we give results obtained by grafting a SAM (dodecanethiol was chosen as SAM model molecule) on the remaining gold surface of a selectively functionalised nanostructured surface (figure 5.28 II). Finally, this section ends with the assessment of the redox-responsiveness of the copolymer. The redox-responsiveness of P(DMA-co-TlaAm)-30% copolymer after grafting on flat gold surfaces (figure 5.28 I.1) was already intensively studied. However, we have tested the redox-responsive property after grafting on a nanostructured gold surface (figure 5.28 I.2). A comparison between results obtained on a flat and on a nanostructured surface is provided.

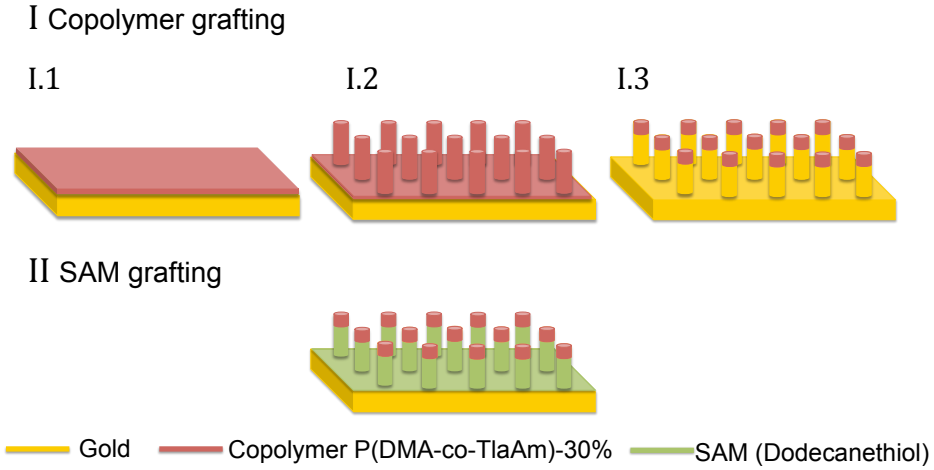

Figure 5.28 – Illustration of all type of surfaces elaborated and characterised. I) Different designs of P(DMA-co-TlaAm)-30% copolymer grafting. Grafting on I.1) flat surface (reference) I.2) nanostructured surface and I.3) selective grafting on the tops of the nanopillars. II) Chemically and nanotopographically patterned surface obtained after SAM grafting.

5.3.1 Copolymer grafting

P(DMA-co-TlaAm)-30% copolymer grafting is performed according to 3 different designs as shown in figure 5.28 I. Modified flat surfaces are used as reference and are thus detailed first (figure 5.28 I.1). The results regarding the nanostructured surfaces are presented and discussed for each case (full and selective grafting of copolymer P(DMA-co-TlaAm)-30% illustrated in figure 5.28 I.2 and I.3 respectively).

Flat gold surface modification

The first type of gold surface modification by copolymer is the functionalisation of a flat surface (figure 5.28 I.1).

Results. Typical CV curves of a flat gold surface before and after copolymer grafting are shown in figure 5.29. The blocking factor defined in section 4.6.1 equals 94 % for

these CV curves. But typical experimental values can range from 80 to 90 %.

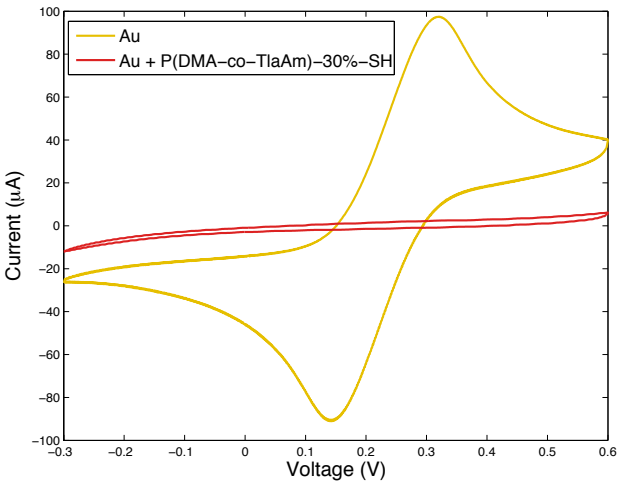

Figure 5.29 – CV measurements performed on a flat gold surface before and after P(DMA-co-TlaAm)-30% copolymer grafting.

Discussion. Before P(DMA-co-TlaAm)-30% copolymer grafting the redox process is limited by diffusion, therefore diffusion peaks can be seen on CV curves. After grafting of P(DMA-co-TlaAm)-30% copolymer, the CV curve completely changes. This is because the copolymer acts as a blocking film that significantly increases electron transfer resistance. Consequently the current decreases drastically. If the surface was perfectly covered by the copolymer almost no current should be measured at all and the blocking factor should almost be equal to 100 %. However the grafting is never perfect, thus a low amount of gold surface is still exposed and a low value of current is measured. The measurement of the BF provides an idea of the covered gold surface. In the shown example (figure 5.29), the BF value measured for the grafted surface is 94 %, which corresponds to a very good surface coverage. The obtained results are thus fully consistent with the theoretical expectations.

Full modification of the nanostructured gold surface

The second type of gold surface modification by copolymer is the complete functionalisation of the nanostructured surface (figure 5.28 I.2).

Results. Several nanostructured surfaces decorated with nanopillars of different heights and densities were modified by P(DMA-co-TlaAm)-30% copolymer in presence of ethanolamine. The characteristics of those surfaces and their respective BF are displayed in table 5.7. Moreover one of the obtained CV curves is shown in figure 5.30.

	Density [10^9 nanopillars/cm^2]	Nanopillar height [nm]	Grafting time [h]	BF [%]
Surface 1	0.38 ± 0.02	1148 ± 349	2	41
Surface 2	0.92 ± 0.02	723 ± 111	24	49
Surface 3	0.87 ± 0.01	510 ± 130	2	73

Table 5.7 – Characteristics of the nanostructured surfaces modified by P(DMA-co-TlaAm)-30%.

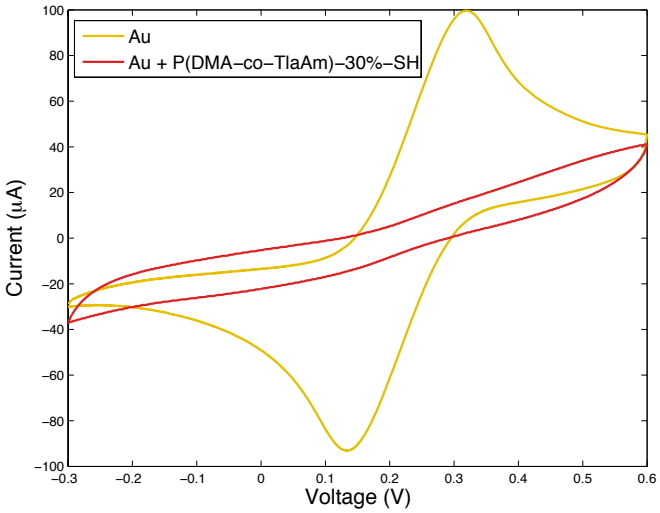

Figure 5.30 – CV measurements performed on surface 3 before and after copolymer P(DMA-co-TlaAm)-30% grafting.

Discussion. First of all, it was soon realised that nanostructured surfaces had a less efficient copolymer grafting than flat gold surfaces as measured BFs were relatively lower. Moreover surface 3 was grafted in the same pot as a flat gold surface with thus exact the same reaction conditions. The flat gold surface (CV showed in figure 5.29) had a BF of 94 % whereas surface 3 had a BF of 73 %. This confirms that nanostructured gold surfaces have lower surface coverage by copolymer than flat gold surfaces. The presence of the nanopillars blocks or limits the copolymer grafting. A hypothesis is that nanopillars limit copolymer diffusion. To check if this could be true, the effect of nanopillar density and height can be evaluated. Also the grafting time could be increased.

First, the effect of the nanopillar density was not investigated because the distance between two nanopillars should be approximately equal to 216 nm[b] if one assumes a density of 10^9 nanopillars/cm^2. This value is relatively high thus the copolymer grafting should not be blocked by a too high nanopillar density. Moreover surface 1 has the lowest density and the lowest BF thus high density does not seem to be a problem. In theory, if the copolymer grafting is diffusion-limited or at least limited by the presence of nanopillars then the less nanopillars there are (i.e. the lower the density) the better the copolymer grafting. This is not observed experimentally so we can conclude that our range of nanopillar densities is not a determining factor for copolymer grafting.
Next, the influence of the nanopillar height was evaluated. By comparing results from surface 1-3 regarding the BF, we can easily conclude that the shorter the nanopillars are the higher the BF and thus the surface coverage. High nanopillars are less favorable for a dense grafting of the copolymer.
Finally, the grafting time was increased from 2 to 24 h in the hope that the BF would increase. But if we compare results obtained for surfaces 1 and 2, we see that the increase of grafting time did not improve the BF.

In addition, we know that the nanopillars are obtained by gold electrodeposition whereas the flat gold surface is obtained by gold evaporation. To exclude the hypothesis

[b] $\langle r \rangle \sim 1/n^{1/2}$ with n = N/S the number of pillars per surface unit i.e. the density. With this formula r = 316. However the nanopillars have a certain diameter thus the distance between two nanopillars from surface to surface should be 316-100 if one assumes that each pillar has a diameter of 100 nm.

that thiol bonding is less efficient on electrodeposited gold compared to evaporated gold, we grafted P(DMA-co-TlaAm)-30% copolymer and dodecanethiol on electrodeposited and evaporated flat gold surfaces. The results (see appendix B section B.4) showed that grafting on electrodeposited gold resulted in a higher BF compared to evaporated gold. It seems that the bad grafting results with low BFs on nanostructured surfaces are due to the topographical effect of the nanopillars and not to the gold fabrication.

Besides the geometry of the nanopillar, the properties of the copolymer should also be looked at. First, the size of the copolymer could be determining. Indeed, a nanostructured surface was modified by dodecanethiol grafting, a much smaller molecule, with a measured BF of 99 % (result is displayed in appendix B section B.5). The main difference between dodecanethiol and the copolymer is the size of the molecule. As the copolymer is a large molecule its diffusion rate should be smaller than that of dodecanethiol.
Another important parameter is the copolymer conformation. When the copolymer is grafted onto a gold surface, its entropy diminishes because the possible conformations also decrease. Maybe the grafting on a nanostructured surface is entropically less favorable than on a flat surface. This could explain why the nanopillar height is such a determining factor in copolymer grafting.

In conclusion the higher the nanopillars, the lower the BF and consequently the density of the copolymer chains grafted on the surface. However it is not clearly understood why.

Selective modification of the tops of nanopillars

The last type of gold surface modification by copolymer was the selective modification of the tops of the gold nanopillars (figure 5.28 I.3).

Results. The surfaces were obtained by the strategy given in figure 3.4 section 3.2. A surface with nanopillars of 374 nm high was first spin-coated with a 0.05 g/ml PAA solution resulting in a film thickness of circa 260 nm. Subsequently a plasma treatment at a power of 100 W during 120 s was applied removing circa 50 nm of PAA film. Therefore the height of nanopillars available for copolymer grafting is approximately 160 nm. Then, the copolymer was grafted on these exposed gold nanopillar tops and the remaining PAA film was dissolved (see section B.6 in appendix B for detail). After PAA film dissolution the surface was characterised by CV and XPS.

The characteristics of the selectively modified surface and its BF are given in table 5.8. Furthermore the obtained CV curve before and after copolymer grafting is shown in figure 5.31. Finally, a schematic diagram is given in figure 5.32 with numerical values indicating the height of the nanopillar theoretically covered with copolymer and the height that was not modified.

This nanostructured surface was also characterised by XPS in order to know the surface composition. This allows to determine whether the copolymer was indeed grafted. As the process to graft the copolymer only on the top of the nanopillars is rather long and that each step is crucial (if one fails at a certain moment the process should be started again from the beginning), it is very important to control the final resulting sample. Up to know each step was already separately optimised : spin-coating, plasma treatment, copolymer grafting and PAA film dissolution. XPS should confirm if the combination of each step also works well. The XPS results include the general spectrum (figure 5.33) and the chemical composition of the surface, which is displayed in table 5.9.

Density [10^9 nanopillars/cm^2]	Nanopillar height [nm]	BF [%]
0.51 ± 0.02	374 ± 77	2.7

Table 5.8 – Characteristics of the nanostructured surface selectively modified by P(DMA-co-TlaAm)-30% copolymer grafting.

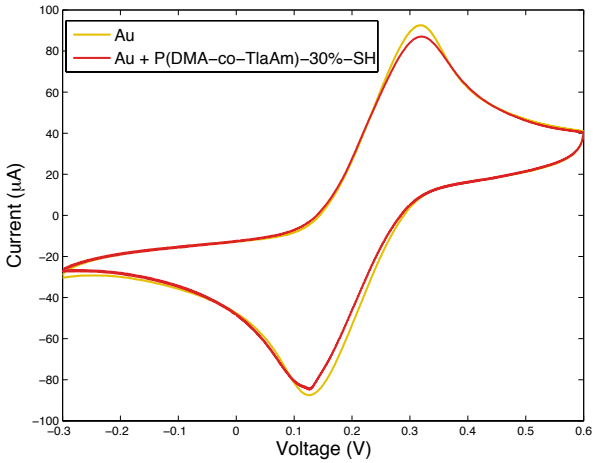

Figure 5.31 – CV measurement of a nanostructured surface before and after selective grafting of copolymer P(DMA-co-TlaAm)-30% on the top of nanopillars.

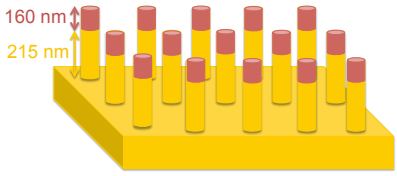

Figure 5.32 – Schematic representation of the selectively modified nanostructured gold surface.

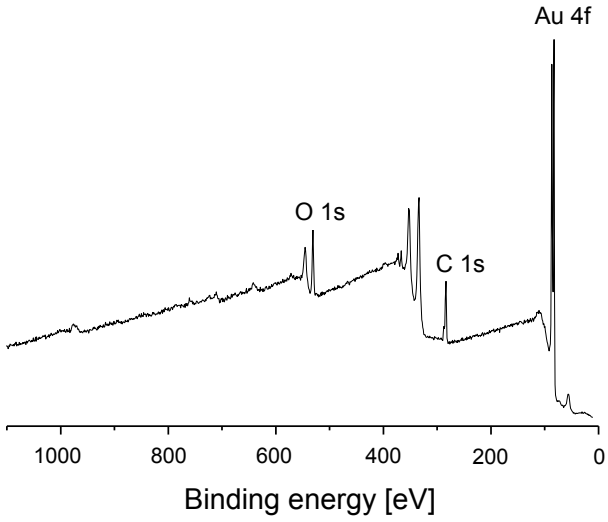

Figure 5.33 – General spectrum obtained by XPS analysis of a nanostructured surface with the tops of nanopillars selectively grafted by P(DMA-co-TlaAm)-30% copolymer.

O 1s [%]	C-(C,H) [%]	COOH [%]	Au 4f [%]	SOx [%]	N 1s [%]
11.4	22.82	5.6	11.26	0.195	0.82

Table 5.9 – Chemical composition of a nanostructured surface with the tops of nanopillars selectively grafted by P(DMA-co-TlaAm)-30% copolymer as determined by XPS.

Discussion. To begin, we discuss the obtained XPS results. First of all, the most crucial is the identification of the copolymer in the surface composition. Results displayed in table 5.9 show the presence of nitrogen although it was not identified in the general spectrum (figure 5.33). Nitrogen is an element that can only be attributed to the copolymer, consequently it attests to the presence of the copolymer grafting onto the gold surface. Moreover, the ratio of nitrogen to gold that was measured (0.82 %/11.26 % = 0.07) is very low compared to results obtained on flat surfaces functionalised by copolymer grafting (ca. 0.5). This could confirm that the copolymer was only grafted on a small surface area, which was most likely the surface of the tops of the nanopillars. However, quantitative XPS results on a nanostructured surface are not as reliable as on a flat surface. The measured ratio of nitrogen to gold may be distorted by the presence of nanopillars.
Furthermore oxidised sulfur was also detected (table 5.9). This means that the thiol functions of the copolymer were oxidised. This is likely due to the long storage of the surface before XPS analysis and the high sensitivity of thiol functions to oxidation.
Next, no potassium was detected in the general spectrum. Potassium is associated to PAA because the pH of the PAA solution was adjusted by KOH before spin-coating. As no potassium is detected all PAA seems to be removed from the surface through the dissolution treatment. However COOH functions were detected (table 5.9) and are certainly associated to the presence of PAA. Consequently it can be assumed that PAA is not completely removed from the surface. It is possible that the grafted copolymer hampers the removal of PAA chains from the surface due to intermolecular interactions.
Regarding the remaining elements, oxygen and carbon are present in the copolymer and in PAA. Their presence is not surprising and gives no further information. However the amounts are high and are thus most likely coming in major part from the presence of PAA. Also only C-(C,H) carbon links were found whereas the copolymer should also have C-(N,C=O) and C(=O) links. Eventually gold is detected, which is expected as not the entire surface is modified.
A first conclusion from XPS results is that the strategy that was elaborated works and only selectively modifies the top of the nanopillars. The second conclusion from XPS measurements is that the PAA film dissolution protocol should be further investigated, as it is not fully efficient.

Besides XPS results, CV measurements were also performed and illustrated in figure 5.31. These show that after grafting, the redox process of the CV experiment is still diffusion-limited. It can be seen that the CV curves are almost identical before and after grafting. This is numerically confirmed by the very low BF of 2.7 %. But the copolymer grafting was effective as proven by XPS measurement. Moreover a flat control surface was immerged in the same pot as the nanostructured surface and this flat control surface had a BF of 92 % confirming the grafting efficiency. The fact that diffusion peaks are still observed after selective grafting of the tops of the nanopillars is likely due to the high amount of available gold surface remaining after grafting. Indeed, even with nanopillars selectively covered by copolymer, the remaining accessible gold surface is still higher than a flat gold surface. It is thus normal that diffusion peaks are still observed. We can thus conclude that selectively modified nanostructured gold surfaces have the same electrochemical behaviour as flat gold surfaces.

Finally, the BF factor of 2.7 % cannot be related to the geometrical surface coverage. Indeed, if we calculate the surface theoretically covered by the copolymer and that we divide this number by the total available gold surface (before grafting) we obtain a theoretical BF of 23 %. Several explanations can be given to this inconsistency. First,

it is possible that the copolymer grafting was not as efficient as expected. This means that even if the top of the nanopillars were exposed the copolymer did not grafted efficiently. Secondly, it is possible that the tops of the nanopillars were not as exposed as theoretically predicted. It was already discussed previously that the plasma treatment may not be as efficient as expected. Thirdly it is possible that the geometrically calculated BF is not equal to the experimentally determined BF. Simply because the remaining surface is still so important that the redox process of the CV measurements remains diffusion-limited. Lastly, the theoretical density (10^9 nanopillars/cm^2) used to calculate the theoretical BF could be very different from the experimental (i.e. real) density. This could significantly influence the calculated BF of 23 %, which is thus only an approximation and not an exact value.

5.3.2 SAM grafting

SAM grafting is performed after selective grafting of the copolymer on the tops of the nanopillars and the dissolution of the sacrificial PAA layer. The purpose is to completely cover the remaining background gold surface as illustrated in figure 5.34. This background coverage is necessary to assess the redox-responsiveness of the copolymer by the grafting and subsequent release of PEG-SH. Indeed, PEG-SH can also be grafted on bare gold surface, which needs to be avoided by making the gold surface inert to PEG-SH grafting. It was thus chosen to graft a SAM (dodecanethiol) on the remaining exposed gold surface. Moreover, by this way a chemical contrast is created and the surface becomes topographically and chemically patterned.

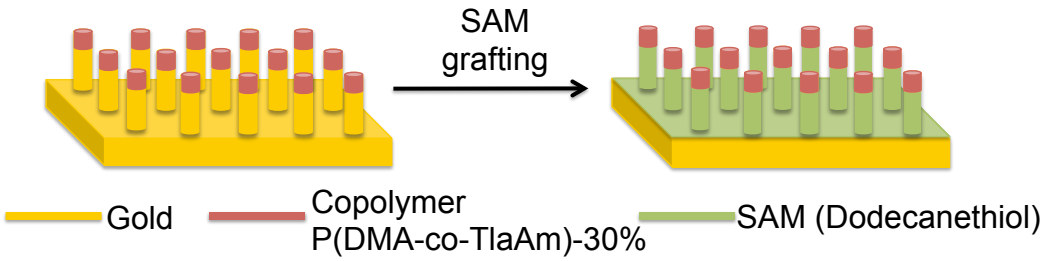

Figure 5.34 – Fabrication of chemically and nanotopographically patterned surfaces.

Results. A surface with nanopillars of 472 nm high was first spin-coated with a 0.065 g/ml PAA solution resulting in a film thickness of circa 400 nm. Subsequently a plasma treatment at a power of 100 W during 120 s was applied removing circa 50 nm of PAA film. Therefore the height of the nanopillars exposed for copolymer grafting was estimated to be of about 120 nm. Then, the copolymer was grafted on these exposed gold nanopillar tops. After which the PAA film was dissolved. Finally, dodecanethiol was grafted on the remaining gold surface. A scheme describing the structure of the bifunctionalised surface is shown in figure 5.36. The surface was characterised by CV and XPS analysis.

First of all, some surface characteristics are displayed in table 5.10. Also the BFs after copolymer and dodecanethiol graftings are given. These BF factors were calculated from the CV curves illustrated in figure 5.35. It must also be precised that in order to control the graftings, a flat gold surface was always added in the same container to get reference surfaces. The obtained BF for copolymer grafting on the flat control surface

equals 93.6 % whereas for dodecanethiol we obtain 99 %.

Beside CV analysis, XPS measurements where also performed. The general spectrum is given in figure 5.37 whereas the chemical composition of the surface is displayed in table 5.11. XPS analysis was performed to confirm the presence of both the copolymer and the dodecanethiol.

Density [10^9 nanopillars/cm^2]	Nanopillar height [nm]	BF after copolymer grafting [%]	BF after dodecanethiol grafting [%]
0.51 ± 0.02	374 ± 77	4.6	87

Table 5.10 – Characteristics of the nanostructured surface modified by P(DMA-co-TlaAm)-30% copolymer and dodecanethiol.

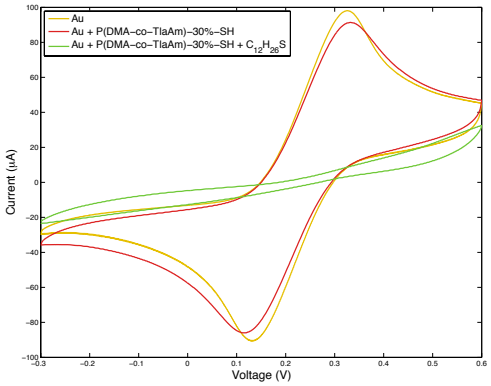

Figure 5.35 – CV measurements on nanostructured surface before grafting (yellow), after grafting of the copolymer on the tops of the nanopillars (red) and after grafting of both copolymer and dodecanethiol (green).

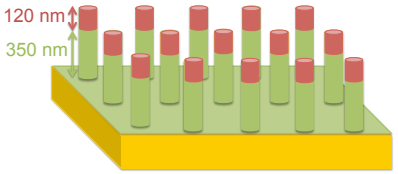

Figure 5.36 – Schematic diagram of a chemically and topographically patterned surface: green and red parts represent the dodecanethiol and the copolymer layer, respectively.

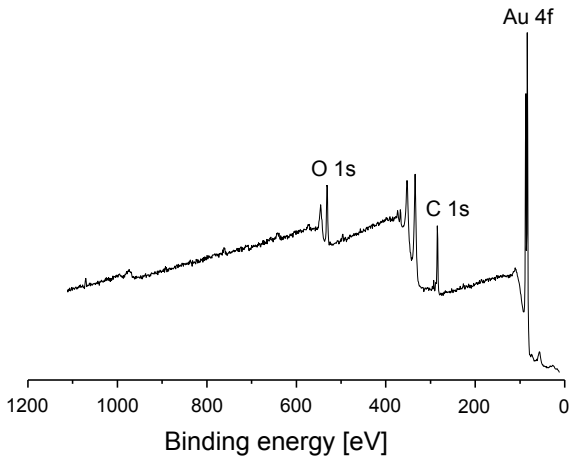

Figure 5.37 – General spectrum obtained by XPS analysis of a nanostructured surface after grafting of both copolymer and dodecanethiol.

O 1s [%]	C-(C,H) [%]	COOH [%]	Au 4f [%]	S-Au 3/2 [%]	N 1s [%]	K 2p [%]
11.33	24.59	4.49	9.51	0.45	0.34	1.12

Table 5.11 – Chemical composition of a nanostructured surface after grafting of both copolymer and dodecanethiol as determined by XPS.

Discussion First of all, XPS analysis are discussed. The first objective of XPS measurements is to identify the copolymer in order to confirm its grafting. In table 5.11 it is indicated that nitrogen was detected. As this element is discriminating for the presence of copolymer, it can be assumed that the grafting was successful.

Next, sulfur linked to gold was detected (table 5.11) with a value of 0.45 %. If we take the ratio of the percentage of nitrogen over the percentage of S-Au, we obtain 0.34/0.45=0.76. This means that the fraction of nitrogen represents approximately three quarters of the percentage of thiol-gold. Moreover, we know that a flat functionalised (i.e. by copolymer grafting) gold surface has a ratio of nitrogen over S-Au of about 3.5 to 4.5. This means that flat functionalised surfaces have a higher nitrogen than S-Au content. However, we observe the opposite with a ratio of 0.76. This means that the S-Au bondings cannot only be attributed to copolymer grafting and this testifies the presence of dodecanethiol contributing to the observed amount of S-Au bondings. Dodecanethiol was thus effectively grafted.

Then, a significant amount of potassium was measured compared to the amounts of nitrogen and S-Au bondings (table 5.11). Also COOH functions were present. Both results attest the presence of PAA. This means that again some PAA chains remained on the surface (through interactions with gold surface or copolymer).
Moreover, oxygen and carbon were present but this is normal and was already discussed previously. Finally, gold was still detected although the surface was completely covered by copolymer and dodecanethiol. This is due to the thickness probed by XPS (ca. 10 nm), which is higher than the thickness of the copolymer or dodecanethiol (1.7-2 nm[67]). Thus the gold surface beneath them is still detected through XPS analysis.
To conclude, XPS measurements allowed to confirm the presence of both copolymer and dodecanethiol.

A second part of the results is the CV analysis. Figure 5.35 shows the CV curves before any grafting, after copolymer grafting and after dodecanethiol grafting.
The first two curves are consistent with the results obtained for selective copolymer grafting. Indeed, at that stage of the process, the surface is in fact exactly the same as the one presented in figure 5.31. The BF value of 4.6 % is higher than the one presented in selective copolymer grafting (i.e. 2.7 %) but still in the same range.
The last CV curve, after dodecanethiol grafting, is very promising. Indeed, no diffusion peaks are observed thus the surface is highly covered and charge transfer now limits the CV redox process. This is numerically confirmed by the high BF of 87 %. This means that modification of the remaining gold surface after copolymer grafting is possible offering new possibilities to add functionalities on the surface.

5.3.3 Copolymer redox-responsiveness assessment

Copolymer redox-responsiveness was evaluated when grafted on the flat gold surface and on nanostructured surfaces. As already explained in section 4.5.4, the evaluation of the redox-responsiveness is made thanks to the grafting and subsequent release of a PEG-SH compound. EIS measurements were performed to evaluate the grafting of this molecule on the copolymer layer. Similarly the release of the PEG-SH compound in reducing conditions is characterised by EIS measurements. More information about EIS is provided in section 4.6.1.

The redox-responsiveness of copolymer grafted on flat surfaces was already intensively evaluated. This kind of surface is used as a reference. The samples that were used to evaluate the copolymer redox-responsiveness are schematically drawn in figure 5.38. We compared a flat and a nanostructured surface coated by the copolymer to assess the influence of the surface nanostructure on the redox-responsiveness of the copolymer layer. As illustrated in figure 5.38 II, the copolymer was grafted onto the whole available gold surface. The other type of grafting, namely only graft on the tops of the nanopillars (figure 5.28 I.3), could not be tested on redox-responsiveness. This is because in case of selective grafting, the gold surface, still exposed, could distort the grafting results by PEG-SH grafting onto the gold surface. Therefore dodecanethiol was grafted on the remaining exposed gold surface to make it inert to PEG-SH grafting. However, experiments showed that dodecanethiol was not inert to PEG-SH grafting. It is believed that thiol exchange can occur between grafted dodecanethiol and PEG-SH. This distorts the obtained results and therefore we will not present them.

Results. First of all, to control the copolymer grafting on both kinds of surfaces (figure 5.38) CV measurements were performed. Those are illustrated in figure 5.39.

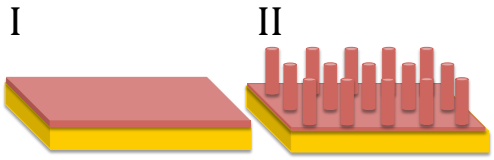

Figure 5.38 – Schematic diagram of the flat and nanostructured gold surfaces modified by the copolymer that were used to test the redox-responsiveness of the copolymer.

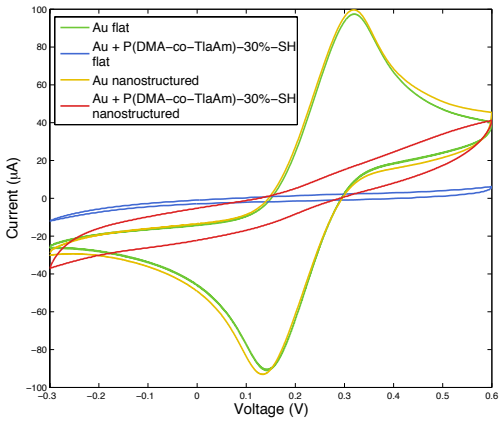

Figure 5.39 – CV measurements performed on flat and nanostructured surfaces grafted by the copolymer.

Furthermore the characteristics of the surfaces are given in table 5.12. It should be mentioned that both surfaces were immersed in the same pot during copolymer grafting so they did undergo exactly the same treatment. However the flat surface is more covered than the corresponding nanostructured surface. This was already discussed previously. The last presented results are the EIS measurements given in figures 5.40 and 5.41.

The evaluation of the grafting and release of PEG-SH was done simultaneously for both surfaces (with a time shift between them of approximately 15 min) and the same solutions were used on both surfaces for the oxidation and the reduction steps. Numerical impedance values can be extracted from these EIS measurements and are presented in table 5.13.

	Density [10^9 nanopillars/cm^2]	Nanopillar height [nm]	BF after copolymer grafting [%]
Flat	-	-	94
Nanostructured	0.87 ± 0.01	510 ± 130	73

Table 5.12 – Characteristics of the flat and nanostructured surfaces modified by P(DMA-co-TlaAm)-30% copolymer.

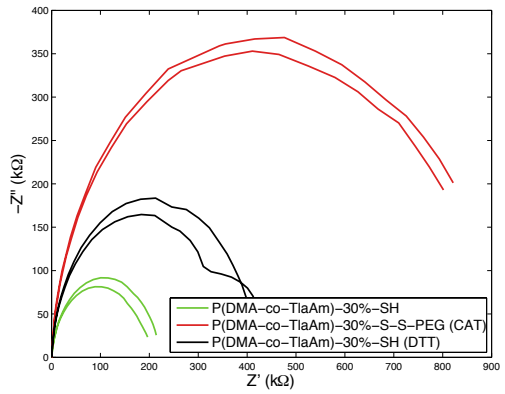

Figure 5.40 – Impedance measurements performed on a flat surface modified by the copolymer (green) then exposed to the PEG-SH (red) in oxidising conditions and finally exposed to DTT (reducing solution) (black) to release PEG-SH.

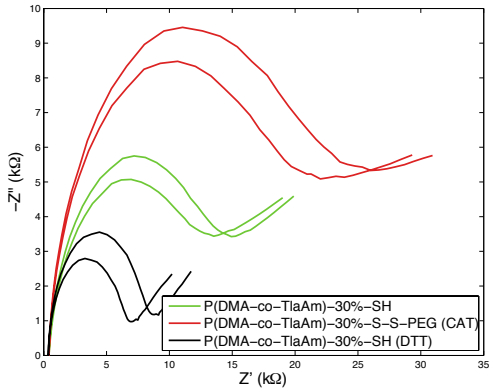

Figure 5.41 – Impedance measurements performed on a nanostructured surface modified by the copolymer (green) then exposed to the PEG-SH (red) in oxidising conditions and finally exposed to DTT (reducing solution) (black) to release PEG-SH.

	R_s [kΩ]	R_{ct} [kΩ]	Diffusion impedance
Flat	0.5-0.7	206 (initial) 812 (After PEG-SH grafting) 412 (After PEG-SH release)	No
Nanostructured	0.4-0.5	14.2 (initial) 24 (After PEG-SH grafting) 7.9 (After PEG-SH release)	Yes

Table 5.13 – Impedance of the solution R_s, the charge transfer R_{ct} and diffusion (mass transport) for the flat and nanostructured surfaces grafted by the copolymer and tested in redox conditions. The values were extracted from the graphs displayed in figures 5.40 and 5.41.

Discussion. First of all, CV analysis informs us on the surface coverage. It can be seen that the nanostructured surface is less covered than the flat surface. However a surface coverage of 73 % should be sufficient to evaluate the redox-responsiveness of the copolymer coating.

Then, EIS measurements give information about the grafting and releasing of the PEG-SH compound in redox conditions.
First, when the PEG-SH compound is grafted, it is experimentally observed for both surfaces that the red curves are always above the green ones (figures 5.40 and 5.41). This means that the impedance increases after grafting. This result is expected because when the PEG-SH compound is grafted, the resistance to charge transfer increases as well as the double layer capacitance due to the presence of an extra non-conductive molecule. This first result thus evidenced the successful grafting of the PEG-SH compound in oxidising medium.
Next, the release of the PEG-SH compound in the reducing conditions is analysed. We experimentally observe for both surfaces that the black curves are always under the red ones (figures 5.40 and 5.41). However the black curves do not coincide with the green ones neither for the flat surface (figure 5.40) neither for the nanostructured surface (figure 5.41). As the black curves in the impedance graphs are always under the red curves, we know that the impedance decreased after the exposure to the reducing medium. This proves that the PEG-SH compounds releasing was effective and that both surfaces are responsive to a reducing medium. However, the release of all the grafted PEG-SH compounds and only of them should bring both surfaces in the exact same state as before grafting (green curves). This is not experimentally observed. For the flat surface the black curve is above the green curve, this means that not all the PEG-SH compounds were released. Maybe the reducing solution was not strong enough; one must keep in mind that far more PEG-SH grafting occurred on the flat surface compared to the nanostructured surface. For the nanostructured surface the black curve is under the green curve. This means that not only the PEG-SH was released but also another compound and that must be the copolymer. In that case, the reducing solution may have been too strong. This can be explained by the fact that the quantity of PEG-SH to release is low on the nanostructured surface compared to the flat surface. Consequently the DTT solution (in excess) has not enough reagents to react with and could start to react with the copolymer by disrupting the S-Au bondings. This hypothesis is supported by the angle change of the diffusion impedance (straight line at low frequencies) : in figure 5.41 the angle of the diffusion impedance comes closer to 45 °C after PEG-SH release. This means that the electrochemical activity is enhanced, thus it could be possible that more gold surface was exposed.

Furthermore EIS curves allow to extract some impedance values given in table 5.13. The first impedance is the solution resistance, namely R_s. This solution resistance should be constant through EIS experiments and have the same value for both surfaces as it only depends on the electrolytical solution that was used (Fe^{2+}/Fe^{3+}). This is indeed experimentally observed : solution resistance is quite constant varying between 0.4 and 0.7 kΩ.
Then, the second impedance is charge transfer resistance, namely R_{ct}. This impedance varies with PEG-SH grafting because the PEG-SH grafting further hampers charge transfer, as it is not conductive. It can immediately be noticed that the flat surface has an overall larger charge transfer resistance then the nanostructured surface. This can be due to two reasons. First, the flat surface is more covered than the nanostructured one; more copolymer means more charge transfer resistance. Secondly, copolymer aggregates could have formed resulting in thicker copolymer layers, thus again more copolymer so more charge transfer resistance. Besides the scale difference between the charge resistance of the flat and the nanostructured surface, we can see that the numerical values confirm the grafting and release of the PEG-SH compounds.
Finally, we can look at the diffusion impedance. As explained in section 4.6.1 diffusion

impedance is represented by a straight line in Nyquist plots at low frequencies. If this impedance is measured it means that the diffusion process created a resistance to the redox process during EIS measurements. In other words, the redox process was limited by mass transport, more specifically diffusion. This can only happen if the gold surface is at least partly uncovered. If we look at the impedance graphs of figures 5.40 and 5.41, we see that the flat gold surface has no straight line in its impedance curves. This proves again that the flat gold surface is well covered by the copolymer. For the nanostructured surfaces straight lines appear in each case. Nevertheless the slope of these straight lines in the red and green curve is far too low (3-7° compared to the expected value of 45°). Moreover only 3 experimental values were recorded for the straight part of the red and green curve ! We can thus not conclude that the process is diffusion limited for the red and green curves. But the black curve has an increase in the slope value (25°), which comes closer to the expected value of 45°. This means that after the release of PEG-SH or exposure of the surface to a reducing solution, more gold is exposed, as the process becomes slightly diffusion limited.

To conclude a nanostructured gold surface coated with a copolymer shows a redox-responsive behaviour. However this behaviour is not as strong as the one obtained with a flat gold surface due to a lower surface coverage by the copolymer. Further experiments should be performed to improve the copolymer grafting on nanostructured surfaces and to adjust the reducing solution that is too strong for the surface tested up to now.

CHAPTER 6

CONCLUSION AND FUTURE PERSPECTIVES

Nanopillars, especially with a high aspect ratio, are promising for future drug delivery applications and biointerface applications to control cell behaviour including cell adhesion, proliferation and even differentiation. Their nanoscale geometry allows to interact directly with cell receptors. Moreover their high specific surface can be functionalised with a significant amount of drug or compound of interest. Finally, their needle shape could potentially provide a direct access to the cell cytoplasm, which is of high interest for drug delivery applications.

In this project a drug delivery strategy to release a chemical compound from the nanopillars was proposed. It relies on disulfide bonding through which a drug can be reversibly grafted and released in a reductive medium like the intracellular medium. Gold nanopillars were functionalised by a polythiolactone copolymer containing multiple protected thiol functions to avoid side reactions. The thiols are revealed by aminolysis and subsequently partially attached to the gold surface. The thiol groups not linked to the gold surface are subsequently used to immobilise a substance of interest through a cleavable disulfide link. The grafting of a thiolated compound onto the available thiols has been achieved in a mild oxidising solution (CAT). Then, the grafted thiolated compounds can be released in a reducing medium like the cell, simulated in this work by a DTT solution.

The ultimate goal of this master thesis was to functionalise nanostructured surfaces by P(DMA-co-TlaAm)-30% copolymer. This functionalisation was performed on the whole surface of the nanostructured sample or selectively on the tops of the nanopillars in order to produce redox-responsive surfaces showing a topographical pattern or both topographical and chemical pattern. To achieve the selective functionalisation of the tops of the nanopillars a proposed strategy was investigated and optimised. First, the deposition of a sacrificial PAA layer by spin-coating was optimised. Then, a plasma treatment was applied to the spin-coated film in order to expose the tops of the nanopillars. After that copolymer grafting was performed followed by an immediate dissolution of the remaining sacrificial PAA layer. The resulting surface was then characterised to evaluate the performance of the whole process. Besides the development of the strategy to selectively functionalise the tops of the nanopillars, the redox-responsiveness of completely functionalised nanostructured surfaces was evaluated.

First, the strategy for selective functionalisation was optimised. It was shown that spin-coating on nanostructures without excessive damage is possible if the spin-coating

speed is very low (i.e. 1750 rpm). Then, the plasma treatment was optimised. Although the plasma treatment allowed to expose the tops of the nanopillars, it seems not as efficient on nanostructured surfaces as on flat surfaces. This is possibly due to the isotropic character of the used plasma treatment. Results could maybe be improved with an anisotropic plasma treatment. Next, the exposed gold surface was grafted with P(DMA-co-TlaAm)-30% copolymer by aminolysis. This step was already optimised in previous research performed in the lab. Thereafter the spin-coated PAA film was dissolved. The protocol to dissolve the PAA film was optimised and no PAA traces were revealed on CV measurements. However, XPS analysis showed the presence of PAA on the gold surface after dissolution. Further experiments should be performed to improve PAA dissolution and remove any remaining traces which can result from interactions between the PAA and copolymer chains. An additional step was also tested : grafting of a SAM (dodecanethiol) on the remaining gold surface to create both topographically and chemically patterned surfaces. The obtained surfaces, with and without dodecanethiol, were characterised by XPS. Those results confirmed the presence of copolymer in both cases and of dodecanethiol if it was grafted. XPS results thus prove the efficiency and achievability of the strategy.

Then, nanostructured surfaces were fully functionalised by the copolymer. These surfaces were characterised by electrochemical analysis. The CV results regarding surface coverage showed a lower surface coverage for nanostructured surfaces compared to flat surfaces. Moreover the surface coverage becomes worse with increasing nanopillar height. The reason behind this is not well understood for the moment. Moreover the redox-responsiveness of the grafted copolymer was evaluated by grafting then releasing a thiolated oligomer in redox conditions. EIS results confirmed that less copolymer was grafted on nanostructured surfaces by showing a lower charge transfer resistance compared to flat surfaces. Nevertheless the copolymer grafted on the nanostructured surface is still redox-responsive as proven by EIS results. To conclude, further research should be performed to improve the copolymer grafting on nanostructured surfaces.

To summarise, selective functionalisation of the tops of nanopillars was successfully achieved and optimisation of each step of the process was performed. Research should now focus on further improvement especially for plasma treatment efficiency and functionalisation of the remaining gold surface. Finally, nanostructured surfaces are less grafted by the copolymer than flat surfaces. The reason behind this is not clear and further experiments should focus on understanding the underlying phenomena.

BIBLIOGRAPHY

[1] C. Chattaway. Towards redox-responsive nanostructured surfaces for drug delivery application. Master's thesis, Université catholique de Louvain, 2015.

[2] X. Liu and F. Chen. Advancing biomaterials of human origin for tissue engineering. *Progress in Polymer Science*, 53:86–168, 2016.

[3] X. Liuab and S. Wang. Three-dimensional nano-biointerface as a new platform for guiding cell fate. *Chem. Soc. Rev.*, 43:2385, 2014.

[4] M. A. Bucaro, Y. Vasquez, B. D. Hatton, and J. Aizenberg. Fine-tuning the degree of stem cell polarization and alignment on ordered arrays of high-aspect-ratio nanopillars. *asc nano*, 6(7):6222–6230, 2012.

[5] X. Xie, A. M. Xu, M. R. Angle, N. Tayebi, P. Verma, and N. A. Melosh. Mechanical model of vertical nanowire cell penetration. *Nano Lett*, 13:6002–6008, 2013.

[6] M. A. Xu, A. Aalipour, S. Leal-Ortiz, A. H. Mekhdjian, X. Xie, A. R. Dunn, C. C. Garner, and N. A. Melosh. Quantification of nanowire penetration into living cells. *Nat. Commun.*, 5:3613–3621, 2014.

[7] S. Bonde, N. Buch-Manson, K. R. Rostgaard, K. T. Andersen, T. Berthing, and K. L. Martinez. Exploring arrays of vertical one-dimensional nanostructures for cellular investigations. *Nanotechnology*, 25:362001–362020, 2014.

[8] C. N. Prinz. Interactions between semiconductor nanowires and living cells. *J. Phys. : Condens. Matter*, 27:233103, 2015.

[9] A.S.G. Curtis. The mechanism of adhesion of cells to glass. a study by interference reflection microscopy. *The Journal of Cell Biology*, 20(2):199–215, 1964.

[10] S. Demousiter and C. Dupont. Course lgbio2030 : Biomaterials.

[11] P. Espeel and F.E. Du Prez. One-pot multi-step reactions based on thiolactone chemistry: A powerful synthetic tool in polymer science. *European Polymer Journal*, 62:247–272, 2015.

[12] P. Espeel, F. Goethals, M.M. Stamenović, L. Petton, and F.E. Du Prez. Double modular modification of thiolactone-containing polymers: towards polythiols and derived structures. *Polymer chemistry*, 3(4):1007, 2012.

[13] A. S. Curtis and M. Varde. Control of cell behaviour : topological factors. *J Nat Cancer Res Inst*, 33:15–26, 1964.

[14] M.J. Dalby, M.O. Riehle, H. Johnstone, S. Affrossman, and A.S.G. Curtis. In vitro reaction of endothelial cells to polymer demixed nanotopography. *Biomaterials*, 23(14):2945–2954, 2002.

[15] C. Choi, S.H. Hagvall, B.M. Wu, J.C.Y. Dunn, R.E. Beygui, and C.J. Kim. Cell interaction with three-dimensional sharp-tip nanotopography. *Biomaterials*, 28(9):1672–1679, 2007.

[16] C.J. Bettinger, R. Langer, and T. Borenstein. Engineering substrate topography at the micro and nanoscale to control cell function. *Angew. Chem. Int. Ed.*, 48(30):5406–5415, 2009.

[17] K.J. Cha, J.M. Hong, D.W. Cho, and D.S. Kim. Enhanced osteogenic fate and function of mc3t3-e1 cells on nanoengineered polystyrene surfaces with nanopillar and nanopore arrays. *Biofabrication*, 5(2):025007, 2013.

[18] S.W. Kuo, H.I. Lin, J.H. Ho, Y.R. Shih, H.F. Chen, T.J. Yen, and O.K. Lee. Regulation of the fate of human mesenchymal stem cells by mechanical and stereotopographical cues provided by silicon nanowires. *Biomaterials*, 33(20):5013–5022, 2012.

[19] S Bonde, T. Berthing, M.H. Madsen, T.K. Andersen, N. Buch-Månson, L. Guo, F. Li, X. Badique, K. Anselme, J. Nygard, and K.L. Martinez. Tuning inas nanowire density for hek293 cell viability, adhesion, and morphology: Perspectives for nanowire-based biosensors. *ACS Applied Materials & Interfaces*, 5(21):10510–10519, 2013.

[20] G.A. Abrams, S.L. Goodman, P.F. Nealey, M. Franco, and C.J. Murphy. Nanoscale topography of the basement membrane underlying the corneal epithelium of the rhesus macaque. *Cell and tissue research*, 299(1):39–46, 2000.

[21] S.Y. Kim and E.G. Yang. Collective behaviors of mammalian cells on amine-coated silicon nanowires. *ACS Applied Materials & Interfaces*, 24(45):455704, 2013.

[22] P.M. Mendes. Cellular nanotechnology: making biological interfaces smarter. *Chem. Soc. Rev.*, 42(24):9207–9218, 2013.

[23] D. Liu, C. Yi, K. Wang, C. Fong, Z. Wang, P.K. Lo, D. Sun, and M. Yang. Reorganization of cytoskeleton and transient activation of ca^{2+} channels in mesenchymal stem cells cultured on silicon nanowire arrays. *ACS Applied Materials & Interfaces*, 5(24):13295–13304, 2013.

[24] E. Migliorini, G. Grenci, J. Ban, A. Pozzato, M. Tormen, M. Lazzarino, V. Torre, and M.E. Ruaro. Acceleration of neuronal precursors differentiation induced by substrate nanotopography. *Biotechnology and Bioengineering*, 108(11):2736–2746, 2011.

[25] W. Kim, J.K. Ng, M.E. Kunitake, B.R. Conklin, and P. Yang. Interfacing silicon nanowires with mammalian cells. *J. Am. Chem. Soc.*, 129(23):7228–7229, 2007.

[26] S. Park, Y. Kim, W.B. Kim, and S. Jon. Carbon nanosyringe array as a platform for intracellular delivery. *Nano Lett.*, 9(4):1325–1329, 2009.

[27] S. J. Hurst, E. K. Payne, L. Qin, and C. A Mirkin. Multisegmented one-dimensional nanorods prepared by hard-template synthetic methods. *Angew. Chem. Int. Ed.*, 45:2672–2692, 2006.

[28] E. Ferain and R. Legras. Track-etch templates designed for micro- and nanofabrication. *Nucl. Instr. and Meth. in Phys. Res.*, 208:115–122, 2003.

[29] H. Masuda and K. Fukuda. Ordered metal nanohole arrays made by a two-step replication of honeycomb structures of anodic alumina. *Science*, 268(5216):1466–1468, 1995.

[30] J. Grainger and J. Blunt. Engineering coatings: Design and application. chapter 5 : Electrodeposited coatings. *Abington Publishing*, pages 167–173, 1998.

[31] S. K. Chakarvarti and J. Vetter. Template synthesis - a membrane based technology for generation of nano-/micro materials : a review. *Radiation Measurements*, 29(2):149–159, 1998.

[32] J. C. Hulteen and C. R. Martin. A general template-based method for the preparation of nanomaterials. *J. Mater. Chem.*, 7(7):1075–1087, 1997.

[33] H. Li. Microfabrication techniques for producing freestanding multi-dimensional microstructures. *Microsyst Technol*, 22:223–237, 2016.

[34] D.P. Birnie. Chemical solution deposition of functional oxide thin films chapter 11 spin-coating : art and science. *Springer-Verlag Wien*, pages 263–274, 2013.

[35] M.S. Vijaya. Piezoelectric materials and devices : Applications in engineering and medical sciences. *CRC Press*, 2012.

[36] L.E. Scriven. Physics and applications of dip coating and spin-coating. *Mat. Res. Soc.*, 121:717, 1988.

[37] K.H.J. Buschow. Handbook of magnetic materials, volume 17, chapter 6 magnetic microelectromechanical systems, section 2 mems fabrication subsection 2.11 deposition. *Elsevier North-Holland*, pages 474–475, 2008.

[38] D.M. Mattox. Handbook of physical vapor deposition (pvd) processing, chapter 1 introduction. *Elsevier*, pages 2–5, 2010.

[39] S. Irving. A dry photoresist removal method. *Journal of the Electrochemical Society*, 1967.

[40] S. Irving. Plasma oxidation process for removing photoresist films. *Solid State Technology*, 14(6):47–51, 1971.

[41] C. Cardinaud, M. Peignon, and P. Tessier. Plasma etching: principles, mechanisms, application to micro- and nano-technologies. *Applied Surface Science*, 164(1-4):72–83, 2000.

[42] A. Fridman. Plasma chemistry chapter 9.7 : Interaction of non-thermal plasma with polymer surfaces. *Cambridge university press*, pages 632–641, 2008.

[43] V. Linder, B. D. Gates, D. Ryan, B. A. Parviz, and G. M. Whitesides. Water-soluble sacrificial layers for surface micromachining. *small*, 1(7):730–736, 2005.

[44] C. Vericat, M.E. Vela, G. Corthey, E. Pensa, E. Cortés, M.H. Fonticelli, F. Ibañez, G.E. Benitez, P. Carro, and R.C. Salvarezza. Self-assembled monolayers of thiolates on metals: a review article on sulfur-metal chemistry and surface structures. *RSC Advances*, 4(53):27730, 2014.

[45] S. Belbekhouche, S. Reinicke, P. Espeel, F. E. Du Prez, P. Eloy, C. Dupont-Gillain, A. M. Jonas, S. Demoustier-Champagne, and K. Glinel. Polythiolactone-based redox-responsive layers for the reversible release of functional molecules. *ACS Appl. Mater. Interfaces*, 6:22457–22466, 2014.

[46] A. Ulman. Formation and structure of self-assembled monolayers. *Chemical Reviews*, 96(4):1533–1554, 1996.

[47] L.L. Rouhana, M.D. Moussallem, and J.B. Schlenoff. Adsorption of short-chain thiols and disulfides onto gold under defined mass transport conditions: Coverage, kinetics, and mechanism. *J. Am. Chem. Soc.*, 133(40):16080–16091, 2011.

[48] J.C. Love, L.A. Estroff, J.K. Kriebel, R.G. Nuzzo, and G.M. Whitesides. Self-assembled monolayers of thiolates on metals as a form of nanotechnology. *Chemical Reviews*, 105(4):1103–1170, 2005.

[49] M. Le Neindre and R. Nicolaÿ. Polythiol copolymers with precise architectures: a platform for functional materials. *Polymer chemistry*, 5(16):4601, 2014.

[50] C.G. Overberger and H. Aschkenasy. Preparation of polymeric condensation products containing functional thiol side chains. polyamides. *Journal of Organic Chemistry*, 25(9):1648–1651, 1960.

[51] C.G. Overberger and H. Aschkenasy. Preparation of polymeric condensation products containing functional thiol side chains. polyurethans. *Journal of the American Chemical Society*, 82(16):4357–4360, 1960.

[52] S. Chakravarthi, C.E. Jessop, and N.J. Bulleid. The role of glutathione in disulphide bond formation and endoplasmic-reticulum-generated oxidative stress. *EMBO Reports*, 7(3):271–275, 2006.

[53] K. Yum, S. Na, Y. Xiang, N. Wang, and M. Yu. Mechanochemical delivery and dynamic tracking of fluorescent quantum dots in the cytoplasm and nucleus of living cells. *Nano Letters*, 9(5):2193–2198, 2009.

[54] J.W. Finley, E.L. Wheeler, and S.C. Witt. Oxidation of glutathione by hydrogen peroxide and other oxidizing agents. *American Chemical Society*, 29(2):404–407, 1981.

[55] J. Wang. Analytical electrochemistry (wang/analytical electrochemistry, third edition) : Fundamental concepts. *Wiley Blackwell*, pages 1–28, 2006.

[56] J. Wang. Analytical electrochemistry (wang/analytical electrochemistry, third edition) : Study of electrode reactions and interfacial properties. *Wiley Blackwell*, pages 29–66, 2006.

[57] G.A. Mabbott. An introduction to cyclic voltammetry. *Journal of Chemical Education*, 60(9):697, 1983.

[58] J. Wang. Analytical electrochemistry (wang/analytical electrochemistry, third edition) : Practical considerations. *Wiley Blackwell*, pages 115–163, 2006.

[59] S.-I. Pyun, H.-C. Shin, Lee J.-W., and J.-Y. Go. Electrochemistry of insertion materials for hydrogen and lithium. *Springer*, pages 115–163, 2012.

[60] S. Hofmann. Auger and x-ray photoelectron spectroscopy in materials science. chapter 3 : Qualitative analysis (principle and spectral interpretation). *Springer*, pages 43–76, 2013.

[61] D. Abou-Ras, T. Kirchartz, and U. Rau. Advanced characterization techniques for thin film solar cells. chapter 6 : Spectroscopic ellipsometry. *Wiley Blackwell*, pages 125–149, 2011.

[62] E. Miele, G.C. Messina, M. Dipalo, V. Shalabaeva, A. Jacassi, S. Panaro, M. Malerba, P. Zilio, and F. De Angelis. Fabrication of zno nanoflowers on gold coated pillars. *Microelectronic engineering*, 141:51–55, 2015.

[63] N. Sanetra, V. Feig, B. Wolfrum, A. Offenhausser, and D. Mayer. Low impedance surface coatings via nanopillars and conductive polymers. *Phys. Status Solidi A*, 208(6):1284–1289, 2011.

[64] A. Winkleman, R. Perez-Castillejos, M. Lahav, Narovlyansky M., L. N. J. Rodriguez, and G. M. Whitesides. Patterning micron-sized features in a cross-linked poly(acrylic acid) film by a wet etching process. *Soft Matter*, 3:108–116, 2007.

[65] M Lahav, M. Narovlyansky, A. Winkleman, R. Perez-Castillejos, E. A. Weiss, and G. M. White-sides. Patterning of poly(acrylic acid) by ionic exchange reactions in microfluidic channels. *Adv. Mater.*, 18:3174–3178, 2006.

[66] I. Doghri. Course lmeca1100 : Mécanique des solides déformables.

[67] T. Kondo, M. Yanagida, K. Shimazu, and K. Uosaki. Determination of thickness of a self-assembled monolayer of dodecanethiol on au(111) by angle-resolved x-ray photoelectron spectroscopy. *Langmuir*, 14(19):5656–5658, 1998.

[68] A. Greer and W. Nix. Nanoscale gold pillars strengthened through dislocation starvation. *American Physical Society*, 73(24):245410, 2006.

[69] V. Anandan, Y.L. Rao, and G. Zhang. Nanopillar array structures for enhancing biosensing performance. *Int J Nanomedicine*, 1(1):73–79, 2006.

[70] D. Bruggemann, B. Wolfrum, and J.P. Silva. Handbook of nanomaterials properties. chapter 11 : Fabrication, properties and applications of gold nanopillars. *Springer*, pages 317–354, 2014.

[71] P. Forrer, F. Schlottig, H. Siegenthaler, and M. Textor. Electrochemical preparation and surface properties of gold nanowire arrays formed by the template technique. *Journal of Applied Electrochemistry*, 30(5):533–541, 2000.

Appendices

APPENDIX A

LITERATURE REVIEW

A.1 Spin-coating on gold nanopillars

Spin-coating is typically used on flat surface but it can also be applied to nanostructured surfaces. Only a few examples are available in the literature but are worth mentioning. A first example is related to the fabrication of ZnO nanoflowers on gold coated pillars.[62] The whole fabrication process is illustrated in figure A.1.

The interesting step is showed in figure A.1 D where a 600 nm thick poly(methylmethacrylate) (PMMA) layer is spin-coated onto the hollow nanopillars circa 1 μm high. Unfortunately no information is provided concerning the spin-coating parameters (e.g. spin-coat solution concentration, speed or acceleration).

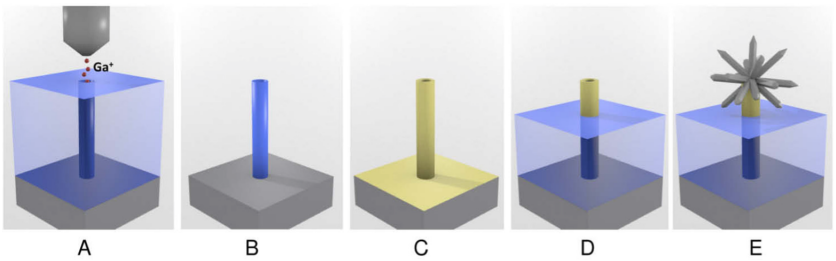

Figure A.1 – Fabrication process of ZnO coated hollow nanopillars. (A) Gallium ion beam defining the structure by local positive tone resist inversion. (B) Acetone removed unexposed resist. (C) Coating of the pillars by thermal evaporation of a gold and ZnO seed layer. (D) A 600 nm PMMA layer (blue) is spin-coated. (E) Selective crystal growth.[62]

Nevertheless, the final structure is observed by scanning electron microscopy (SEM) and is showed on figure A.2. This proves that ZnO crystals only grow on the upper part of the nanopillars. Thus the spin-coated layer indeed only covered the lower part of the nanopillars and played its role like expected. It also proves that spin-coating can be used on nanostructured surfaces to deposit thin and homogenous film.

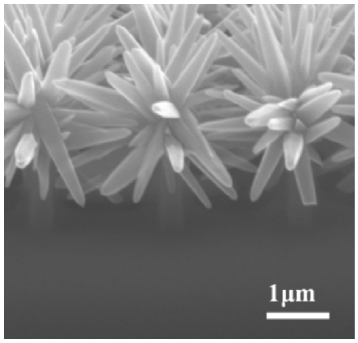

Figure A.2 – SEM image showing the selective growth of the ZnO crystals at the top of the pillars.[62]

A second example of spin-coating onto nanopillars is provided by Sanetra et al.[63] Their study concerns conductive polymers (PEDOT/PSS)[a] for ultra thin electrode coatings. More precisely, they applied PEDOT/PSS coatings on gold nanopillar electrode surfaces by spin-coating. In order to do that, they made an aqueous solution of PEDOT/PSS and spin-coated with speeds ranging from 2000 to 8000 rotations per minute (rpm) varying by this way the obtained film thickness. The volume of solution deposited was fixed at 40 μl. Furthermore the films were baked at 150°C for 2 min on a hotplate to evapore the solvent, water in this case. The resulting films were observed by SEM by taking cross-sectional views at 60° after cleaving the surfaces (e.g. figure A.3 shows a 120 nm thick film). The average diameter, height and spacing of the gold nanopillars are 50, 200 and 30 nm. In this case, it can be seen that the spin-coated film follows the structure of the pillars but does not go to the bottom of the electrode. This is explained by the fact that the distance between two pillars is in the same range as the thinnest polymer thickness realised in the study.[63] However the surface roughness is about 0.8 nm (root mean square for measurement on 0.5×0.5 μm^2) for a film thickness of 120 nm. This indicates that a more or less homogenous film can be obtained by spin-coating on nanopillars.

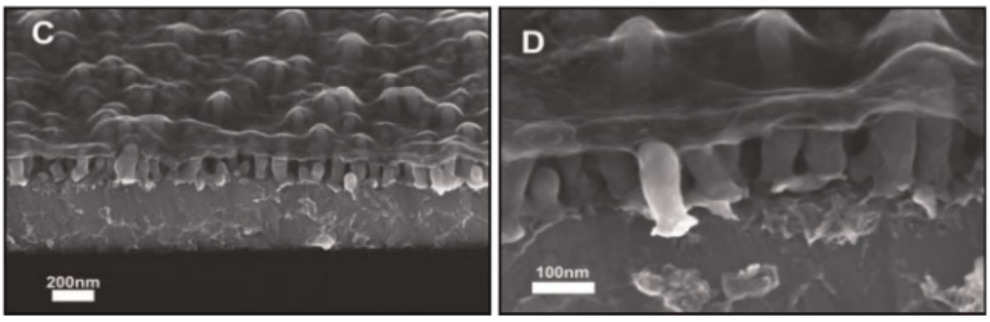

Figure A.3 – Cross-sectional SEM images of gold nanopillar samples spin-coated with PEDOT/PSS. (C) and (D) show a 120 nm film in overview and close up.[63]

[a] poly(3,4-ethylenedioxythiophene) stabilised with polystyrene sulfonic acid

A.2 Gold nanopillar properties

Mechanical stability

Mechanical properties of nanoscale objects deviate from those of the bulk because of side effects. Gold nanopillars are no exception and often exhibit an increase in magnitude of mechanical properties. For example, it was demonstrated that the ultimate compression yield stress increases from 30 MPa, bulk value, to 800 MPa for gold nanopillars with a diameter of 250 nm.[68] It is believed that this effect is due to dislocation starvation.
Mechanical stability is an important parameter if the gold nanopillars are exposed to external forces during processing (e.g. spin-coating) or simply by being put in contact with liquids. Anandan et al. studied the behaviour of nanopillars in a liquid environment.[69] They concluded that pillars with an aspect ratio below 30 did not deform, thus, gold nanopillars with low aspect ratio have a higher resistance to bending. This is in interesting result for cell culture studies or electrochemical studies that require the pillars to be exposed to liquids.[70]
In conclusion, gold nanopillars have stronger mechanical properties than in the bulk state and are mechanically stable.

Electrochemical properties

Metal nanopillars including the gold ones are nanoelectrode ensembles. If the mean distance between two pillars falls in the submicrometer range, the diffusive field of individual pillar electrodes will likely overlap as shown in figure A.4 where various diffusion mecanisms are shown. The resulting macroscopic diffusion layer is dominated by the geometric aspects of the electrode itself and not by the individual structure of the nanopillars. Macroscopic nanopillar electrodes thus exhibit 'classical' peak-shaped voltammograms, instead of the diffusion-limited sigmoidal shapes observed with individual ultramicro- or nanoelectrodes that exhibit radial diffusion profiles.[70,71]

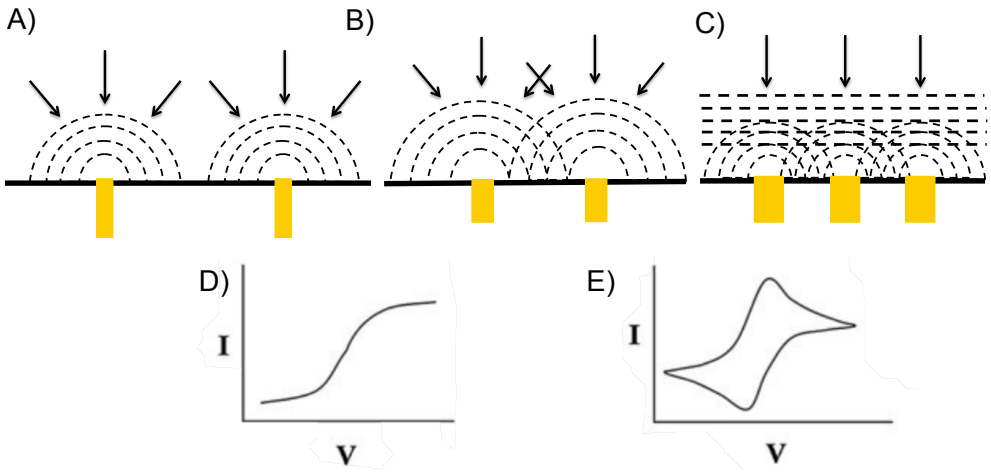

Figure A.4 – Schematic representation of electrode ensembles of different size and density showing A) radial diffusion B) overlapping radial diffusion C) planar diffusion. D) and E) Cyclic voltammograms for the diffusion scenario in A) and C) respectively.[70]

APPENDIX B

RESULTS

B.1 Spin-coating calibration

Film thickness calibration was performed for various speeds ranging between 1750 and 3000 rpm as shown in figure B.1. However only the 1750 rpm speed was further used because higher speeds damaged the nanopillars (see next section).

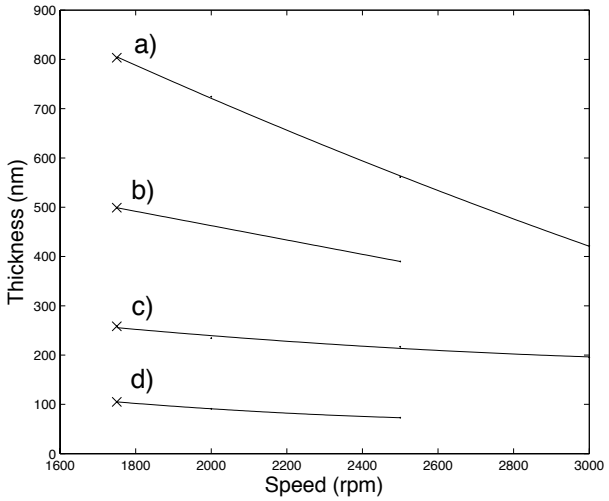

Figure B.1 – Calibration curves for PAA concentrations of a) 0.01 b) 0.075 c) 0.05 d) 0.025 g/ml. Cross-marked points are experimental values, the curves result from extrapolation of previously obtained results.

B.2 Spin-coating at a speed higher than 1750 rpm on nanostructured gold surfaces

A first spin-coating test was performed by spin-coating at 2000 and 2500 rpm using a PAA solution concentration of 0.1 g/ml. More precisely, a surface having nanopillars of about 700 nm high was spin-coated at 2000 rpm whereas a surface having nanopillars of 800 nm high was spin-coated at 2500 rpm. After PAA film dissolution, both surfaces were analysed by SEM showing the severely damaged nanopillars (figure B.2). As most of the nanopillars had broken, the surfaces could no longer be used. However, it proved

that spin-coating is a heavy treatment for nanostructured surfaces and that it can result in severe damage of the nanostructure.

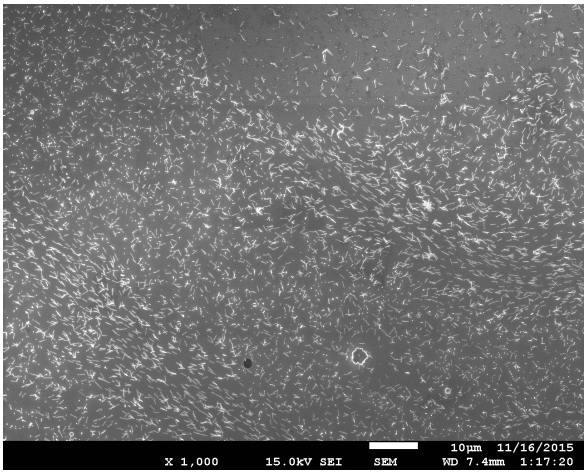

Figure B.2 – SEM image of a surface having nanopillars of a height of ca/ 700 nm after PAA film dissolution (× 1000).

B.3 PAA film defects created by plasma treatment

The plasma treatment applied on the spin-coated nanostructured surfaces is quite heavy as serious PAA film defects appear on SEM images (figure B.3. However, these defects are not visible on the original image shown in chapter 5 section 5.1.3 figure 5.16. To make the defects more visible, the contrast and the brightness of the original image were increased resulting in the image shown in figure B.3. This image is consistent with AFM images also showing holes all over the surface (figure 5.17 in section 5.1.3, chapter 5).

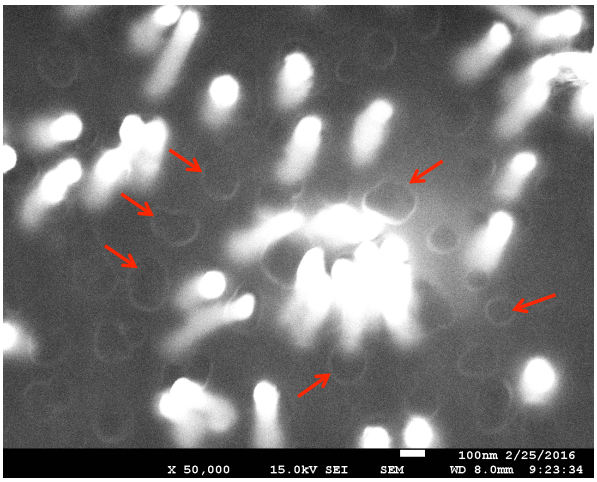

Figure B.3 – SEM zoom-in image of spin-coated surface B after plasma treatment. Red arrows indicate visible holes in the PAA film. The contrast and brightness of the image were increased to have the defects appearing more clearly.

B.4 Thiol grafting on electrodeposited and evaporated flat gold surfaces

Gold nanopillars were fabricated by electrodepositing gold whereas flat gold surfaces are made by evaporating gold. As the techniques employed to fabricate solid gold are different, the resulting microstructure of the gold is also different. This could hypothetically influence the thiol-gold link. To evaluate this effect P(DMA-co-TlaAm)-30% copolymer and dodecanethiol were grafted on both evaporated and electrodeposited flat gold surfaces. Moreover, CV measurements were performed before and after grafting to evaluate the BF. CV results are given in figures B.4 and B.5 for P(DMA-co-TlaAm)-30% copolymer and dodecanethiol grafting respectively. The calculated BFs are displayed in table B.1.

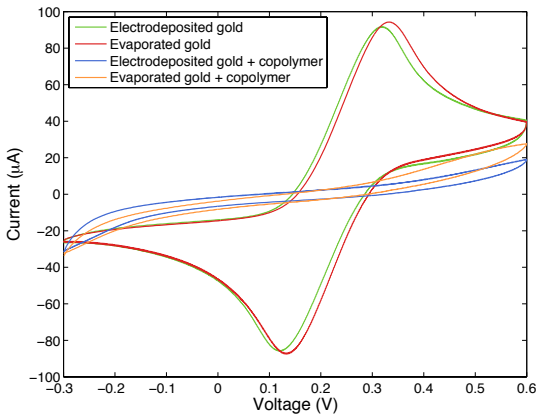

Figure B.4 – CV measurements of flat evaporated and electrodeposited gold surfaces before and after copolymer grafting.

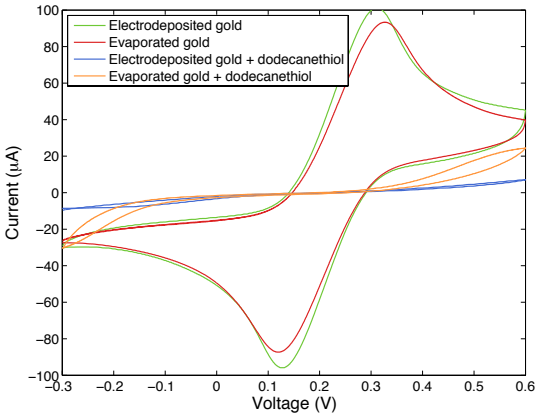

Figure B.5 – CV measurements of flat evaporated and electrodeposited gold surfaces before and after dodecanethiol grafting.

	BF after copolymer grafting [%]	BF after dodecanethiol grafting [%]
Electrodeposited gold	89	99
Evaporated gold	85	92

Table B.1 – BF obtained by grafting copolymer and dodecanethiol on electrodeposited and evaporated flat gold surfaces.

The calculated BFs testify that grafting through thiol-gold links is more efficient on electrodeposited gold surfaces than on evaporated gold surfaces, although the difference in terms of BF is low between both types of surfaces. This means that nanopillars (electrodeposited gold) should be more efficiently covered than a flat gold surface (evaporated gold).

B.5 Dodecanethiol grafting on a nanostructured gold surface

Dodecanethiol was grafted on a nanostructured surface having nanopillars of about 700 nm high. This experiment was performed to determine if dodecanethiol could be

efficiently grafted onto nanostructured surfaces. Therefore CV measurements were performed before and after grafting. Results are presented in figure B.6. One can see that the grafting was extremely efficient resulting in a BF of 99 %.

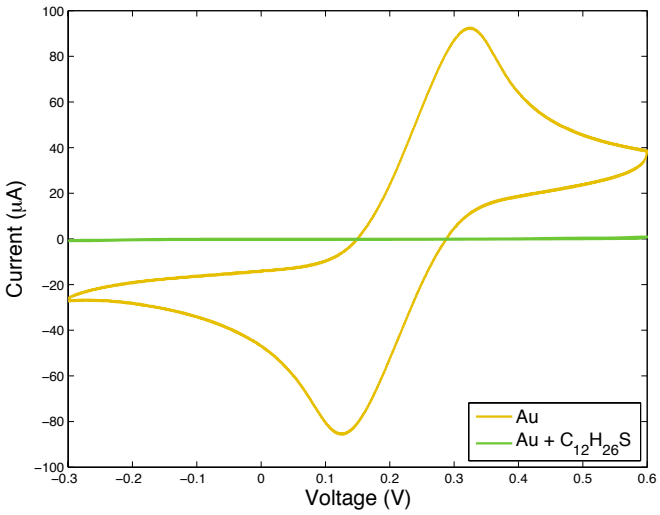

Figure B.6 – CV measurements of a nanostructured gold surface before and after dodecanethiol grafting.

B.6 Optimisation of PAA film dissolution

PAA film dissolution was first performed in milliQ water during 15 min with ultrasounds. However, as ultrasounds are damaging for nanostructures like nanopillars, this protocol was abandoned. The new protocol was to immerge the spin-coated surfaces in circa 15 ml of milliQ water during 1 h. Nonetheless traces of PAA appeared on SEM images (figure B.7).

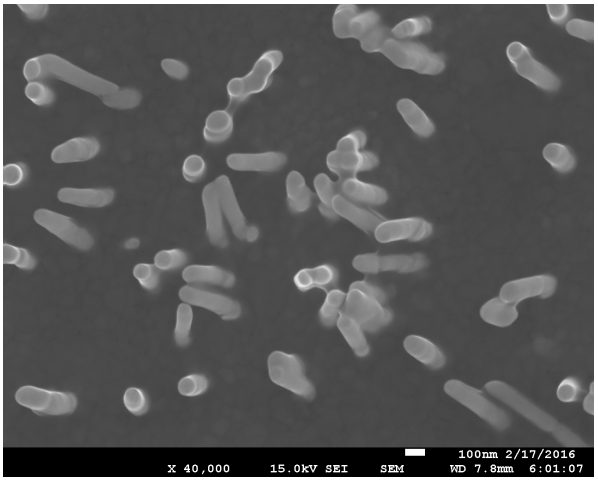

Figure B.7 – SEM image of a nanostructured surface after PAA film dissolution for 1 h.

Consequently, the protocol was adapted by increasing the dissolution time from 1 to 3 h. Moreover, the pH of the milliQ water was adjusted. MilliQ water has a pH of approximately 5 and is thus acid. To improve the PAA dissolution, the pH of the water was increased to 7. To control the effectiveness of this protocol, a nanostructured surface

was analysed by CV, then spin-coated and subsequently its PAA film was removed according to the new protocol. After that the surface was analysed again by CV. Results are given in figure B.8. As the CV curves almost perfectly overlap it seems that PAA dissolution was effective. However the technique is not sensitive enough to exclude any trace of PAA.

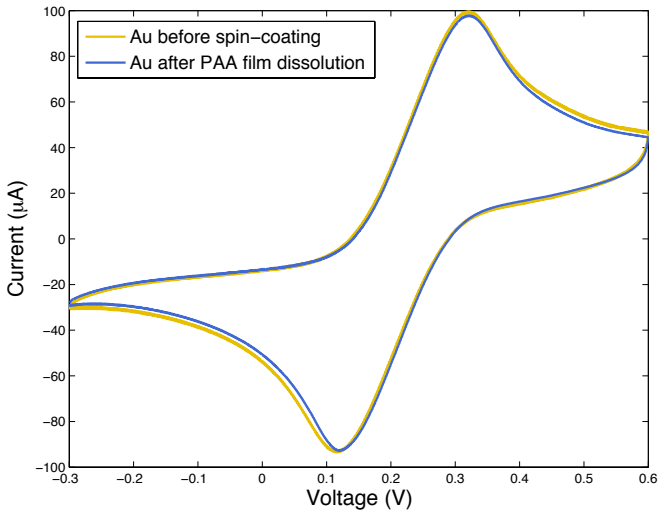

Figure B.8 – CV measurements of a nanostructured gold surface before spin-coating and after PAA film dissolution.

Rue Archimède, 1 bte L6.11.01, 1348 Louvain-la-Neuve **www.uclouvain.be/epl**